

Ferumoxytol iron oxide nanoparticles as a magnetic resonance contrast agent in central  
nervous system lesions

By

Heather Loraine McConnell

A DISSERTATION

Presented to the Neuroscience Graduate Program,

Oregon Health and Science University,

And School of Medicine

In partial fulfillment of

The requirements for the degree of

Doctor of Philosophy

January 2018

School of Medicine  
Oregon Health & Science University  
CERTIFICATE OF APPROVAL

This is to certify that the Ph.D. dissertation of  
Heather L. McConnell  
has been approved on

Advisor, Edward A. Neuwelt, M.D.

Co-Advisor, Leslie L. Muldoon, Ph.D.

Member and Chair, Philip Stork, Ph.D.

Member, Mary Logan, Ph.D.

Member, Damien Fair, Ph.D.

## Contents

<b>List of Figures</b> .....	<b>vi</b>
<b>Acknowledgments</b> .....	<b>ix</b>
<b>Abstract</b> .....	<b>xi</b>
<b>Chapter 1: The Translational Significance of the Neurovascular Unit</b> .....	<b>1</b>
<b>1.1. Abstract</b> .....	<b>2</b>
<b>1.2. NVU Components and Functions</b> .....	<b>2</b>
<i>Vascular Endothelial Cells</i> .....	<b>3</b>
<i>Pericytes</i> .....	<b>4</b>
<i>Astrocytes</i> .....	<b>4</b>
<i>Neurons</i> .....	<b>5</b>
<i>Basement membranes</i> .....	<b>6</b>
<i>Microglia and Perivascular Macrophages</i> .....	<b>7</b>
<b>1.3. NVU: Intercellular Interactions</b> .....	<b>8</b>
<i>Functional Hyperemia</i> .....	<b>8</b>
<b>1.4. NVU: Pathology</b> .....	<b>10</b>
<i>Alzheimer's Disease</i> .....	<b>10</b>
<i>NVU pathology in neoplastic disease</i> .....	<b>13</b>
<b>Figures</b> .....	<b>15</b>

<b>Chapter 2. Introduction to ferumoxytol .....</b>	<b>21</b>
<b>2.1 Introduction.....</b>	<b>21</b>
<b>2.2 Fundamental principles of magnetic resonance imaging .....</b>	<b>23</b>
<i>Tissue Magnetization .....</i>	<i>24</i>
<i>Relaxation Times.....</i>	<i>25</i>
<i>Weighted images .....</i>	<i>26</i>
<i>Clinical magnetic resonance imaging contrast agents .....</i>	<i>27</i>
<b>2.3 Use of gadolinium-based contrast agents in the brain.....</b>	<b>31</b>
<i>Mechanisms of gadolinium-based enhancement .....</i>	<i>32</i>
<i>Impaired Gadolinium elimination.....</i>	<i>33</i>
<b>2.4 Ferumoxytol as an alternative MRI contrast agent.....</b>	<b>36</b>
<i>Properties of Ferumoxytol .....</i>	<i>36</i>
<i>Cerebrovascular Imaging with Ferumoxytol.....</i>	<i>37</i>
<i>CNS Inflammatory Imaging with Ferumoxytol.....</i>	<i>40</i>
<b>Figures.....</b>	<b>43</b>
 <b>Chapter 3. Ferumoxytol nanoparticle uptake in brain during acute neuroinflammation is cell-specific .....</b>	 <b>50</b>
<b>3.1 Abstract.....</b>	<b>51</b>
<b>3.2 Introduction.....</b>	<b>52</b>
<b>3.3 Methods.....</b>	<b>54</b>

<b>3.4 Results .....</b>	<b>59</b>
<b>3.5 Discussion.....</b>	<b>62</b>
<b>Acknowledgements .....</b>	<b>67</b>
<b>Figures.....</b>	<b>69</b>
<b>Chapter 4. Future directions for ferumoxytol research .....</b>	<b>77</b>
<b>4.1 Pseudoprogession is an immune-related response occurring after glioma therapy .....</b>	<b>78</b>
<b>4.2 Ferumoxytol uptake is cell-specific .....</b>	<b>82</b>
<b>4.3. Ferumoxytol highlights cerebrospinal fluid movement through cortical glymphatic space .....</b>	<b>84</b>
<b>4.4. Intracellular localization may alter the T<sub>1</sub> signal of ferumoxytol .....</b>	<b>86</b>
<b>4.5 Ferumoxytol immunoconjugation may enable tumor cell labeling.....</b>	<b>89</b>
<b>Summary.....</b>	<b>94</b>
<b>Figures.....</b>	<b>95</b>
<b>References .....</b>	<b>103</b>

## List of Figures

<b>Figure 1.1.</b> Anatomical structure of the neurovascular unit (NVU). .....	15
<b>Figure 1.2.</b> Perivascular clearance in brain: The Glymphatic System .....	17
<b>Figure 1.3.</b> Neurovascular unit components act in concert to regulate cerebral blood flow. ....	18
<b>Figure 1.4.</b> Antiangiogenic therapy normalizes tumor vasculature. ....	19
<b>Figure 2.1.</b> Vector representation of net magnetization produced in the presence of an external magnetic field.....	43
<b>Figure 2.2.</b> Time course of tissue magnetization is governed by the $T_1$ and $T_2$ relaxation constants.....	44
<b>Figure 2.3.</b> Magnetic resonance imaging contrast agents shorten $T_1$ and $T_2$ relaxation times .....	45
<b>Figure 2.4.</b> Gadolinium-based contrast reagent extravasation in a three-compartment tissue model. ....	46
<b>Figure 2.5.</b> Vascular localization of gadolinium-based contrast agents and ferumoxytol after injection .....	47
<b>Figure 2.6.</b> Imaging phases of ferumoxytol after intravenous administration in a single tumor-bearing patient.....	48

<b>Figure 2.7.</b> Spatial resolution comparison of cerebral blood volume maps calculated from gadolinium-enhanced dynamic susceptibility contrast imaging versus ferumoxytol-enhanced steady-state imaging .....	49
<b>Graphical Abstract.</b> An ultrasmall superparamagnetic iron oxide nanoparticle (ferumoxytol) is used off-label as a contrast agent for magnetic resonance imaging of neuroinflammation in an immune-competent rat model.....	68
<b>Figure 3.1.</b> Maximum ferumoxytol MRI susceptibility/enhancement occurs 48 h post inflammatory insult.....	69
<b>Figure 3.2.</b> Experimental protocol schematic .....	71
<b>Figure 3.3.</b> Immunostaining demonstrates that ferumoxytol traffics from the systemic circulation to reactive CNS lesions.....	72
<b>Figure 3.4.</b> Immunofluorescence analysis reveals ferumoxytol localization within lesional macrophages and perivascular spaces .....	73
<b>Figure 3.5.</b> Ultrastructural analyses of CNS tissue show ferumoxytol localization within astrocyte endfeet, astrocyte processes, and phagocytic CNS macrophages .....	75
<b>Figure 4.1.</b> Imaging characteristics of pseudoprogression.....	95
<b>Figure 4.2.</b> Ferumoxytol trafficking to cervical lymph nodes .....	97
<b>Figure 4.3.</b> Intracellular localization may alter the $T_1$ signal of ferumoxytol.....	98
<b>Figure 4.4.</b> WST-1 assay of cell survival.....	99

<b>Figure 4.5.</b> Electron micrographs of SKBR3 human breast cancer cells treated with ferumoxytol immunoconjugate in vitro .....	100
<b>Figure 4.6.</b> Trastuzumab-ferumoxytol immunoconjugate in vivo magnetic resonance imaging pilot study .....	102

## **Acknowledgments**

*For my daughter, Casey.* Every tear, every class, every late night, every paper, every disappointment, and every success: it's all been for you. You're my greatest accomplishment, my most treasured friend, and my reason for everything.

My incredible advisors, Dr. Neuwelt and Dr. Muldoon. You have spent 5 years encouraging me, inspiring me, and guiding me through two graduate degrees. Dr. Neuwelt, your unfaltering enthusiasm for science and medicine inspires me daily. Your dedication to your patients is rivaled only by your dedication to your laboratory and clinical staff. Thank you for your unwavering support and kindness over the years. Leslie, you have been so much more than simply a mentor to me. You have been a confidant, an advocate, a supporter, and of course - a friend. You are always available to discuss science, potential experiments, writing, professional development, or whatever I need. You are the most caring and supportive boss I have ever had, and I will forever treasure the time I have spent working for and learning from you.

My collaborator and mentor, Randy Woltjer. Thank you for all of your academic and life advice over the years. I have thoroughly enjoyed all of our collaborations and all of the time we have spent together in lab.

Dan Schwartz, collaborator, and friend. Thank you for the (almost daily) assistance, scientific discussion, and laughter. You have directly contributed to much of the work in this dissertation and I'm incredibly grateful for your hard work and your friendship.

My dissertation advisory committee, Drs. Stork, Logan and Fair. Thank you for your advice and guidance these past 5 years, for your flexibility in scheduling, and for our many wonderful discussions. I have greatly appreciated your enthusiasm for my non-traditional project and your kind approval of my brief foray into clinical research endeavors. Thank you also to Dr. Schnell for agreeing to sit on my defense committee.

Finally, all those who have contributed indirectly to my dissertation. My love, Arek.

Thank you for your unwavering support these past 7 years. Thank you for endless acts of kindness and love; you have my whole heart. My parents, Julie and Carl, who financed my return to school and have supported me in all ways possible through the many ups and downs of life, health, motherhood, and school. You mean the world to me and I love you more than words can define. Thanks for letting me reach for the stars and for always having my back. My brother and sister-in-law, Kyle and Kathryn. My decision to return to school was prodigiously influenced by you and your steadfast belief that I was capable of something greater. Thank you for helping me enroll in school, for taking care of Casey when I had to work night shifts, for my early math and chemistry tutoring, and for all the times you convinced me to push through in those first two years when I felt so close to quitting. Mike and my de facto grandparents, Otto and Norma. Thank you for many weekends of laughter, cookies, farm dogs, and fun.

I am deeply appreciative of you all – thank you.

## Abstract

Magnetic resonance imaging (MRI) is an essential tool in the assessment of central nervous system (CNS) lesions, allowing us to visualize abnormal vasculature and structures associated with neurological diseases and brain tumors. Gadolinium-based contrast agents are commonly used to further enhance brain tissue discrimination. However, this approach is limited by rising concerns about tissue retention of traditional, gadolinium-based contrast agents. As such, the need to characterize potential alternative contrast agents is increasing rapidly. In this dissertation, I discuss the application of ferumoxytol, an iron oxide nanoparticle, for image contrast in MRI of CNS lesions. These data include immunohistochemical stains with a novel marker of the nanoparticle, electron micrographs demonstrating the intracellular localization of these nanoparticles within CNS lesions and ferumoxytol contrast-enhanced high-resolution MR images. In broad terms, the goal of this dissertation is to determine how ferumoxytol behaves in acute inflammatory CNS lesions and around tumor sites and to determine whether this behavior informs clinical MRI interpretation.

The first chapter of this dissertation is a brief literature review of the neurovascular unit (NVU) in health and in select pathologies. I describe the individual components of the NVU as well as their intercellular interactions in the brain. Further, I describe how NVU components act in concert to modify cerebrovascular function and permeability in health and representative CNS diseases, including CNS neoplasms and Alzheimer's disease. The second chapter is an introduction to ferumoxytol, its chemical and structural properties, and its numerous applications in the clinical setting. In the third chapter, I describe my use of immune-competent rats to study ferumoxytol behavior at an

acute neuroinflammatory lesion and in the surrounding cerebrovasculature. Prior ferumoxytol studies have been hindered by the inability to differentiate the nanoparticle from endogenous iron or blood products in tissues. One of the important themes of this work is the unequivocal localization of ferumoxytol in tissues using a Dx1 antibody to visualize the nanoparticle coating, in lieu of the general Perls Prussian blue iron stain, which cannot distinguish the ferumoxytol core from endogenous iron. I developed a novel model of neuroinflammation that provides a localized lesion at which to study ferumoxytol contrast-enhancement on MRI and cell-specific uptake. Comparing MR images acquired *in vivo* with *ex vivo* thin-sectioned brain tissue slices at the same time point allowed me to compare patterns of differential ferumoxytol signal enhancement to cell uptake patterns. These data suggested that high concentration of ferumoxytol within macrophages results in marked signal loss at a lesion site, while lower concentration of ferumoxytol results in signal enhancement on T<sub>1</sub>-weighted images. These data also confirmed that ferumoxytol uptake did not occur in tumor cells, but rather in macrophages and astroglia. Finally, chapter 4 is a discussion of future research directions for ferumoxytol.

The central theme, present throughout this work, is the development and application of ferumoxytol nanoparticles to MRI endeavors. The work has translational applicability and aims to improve diagnostic discrimination of CNS lesions in clinical MRI applications

## **Chapter 1: The Translational Significance of the Neurovascular Unit**

Heather L. McConnell, Cymon N. Kersch, Randall L. Woltjer, Edward A. Neuwelt

From the Departments of Neurology, Pathology, Neurosurgery, and Veterans Affairs,  
Oregon Health & Science University, Portland, OR, USA

*Published in the Journal of Biological Chemistry, January 2017*

*(DOI: 10.1074/jbc.R116.760215)*

**Keywords:** neurovascular unit, blood-brain barrier, cerebrovasculature, vascular endothelial growth factor (VEGF), brain, brain tumor, vasculogenesis, glioblastoma

## **1.1. Abstract**

The mammalian brain is supplied with blood by specialized vasculature that is structurally and functionally distinct from that of the periphery. A defining feature of this vasculature is a physical blood-brain barrier (BBB). The BBB separates blood components from the brain microenvironment, regulating the entry and exit of ions, nutrients, macromolecules, and energy metabolites. Over the last two decades, physiological studies of cerebral blood flow dynamics have demonstrated that substantial intercellular communication occurs between cells of the vasculature and the neurons and glia that abut the vasculature. These findings suggest that the BBB does not function independently, but as a module within the greater context of a multicellular neurovascular unit (NVU) that includes neurons, astrocytes, pericytes, and microglia as well as the blood vessels themselves. Here, we describe the roles of these NVU components as well as how they act in concert to modify cerebrovascular function and permeability in health and select diseases.

## **1.2. NVU Components and Functions**

The neurovascular unit (NVU) enables tight regulation of blood flow through the vasculature, which has unique structure in the brain. The arteries that dive into the brain from the subarachnoid space consist of endothelial cells (ECs), a basement membrane, smooth muscle cells, the perivascular (Virchow-Robin) space, pia mater, and astrocyte endfeet (Figures 1.1 and 1.2). As vessels continue deeper into the brain, they lose their smooth muscle cell and pia mater coverage, gaining pericytes between the EC and astrocyte endfeet. Along the length of the cerebral vasculature, neuronal and astrocyte processes contact other components of the NVU, where they can influence the function of

the entire unit. Here we describe individual NVU components and their roles within the NVU.

### *Vascular Endothelial Cells*

The ECs lining cerebral blood vessels are the core anatomical unit of the vascular blood-brain barrier (BBB), protecting the brain from systemic influences by limiting transcellular and paracellular transport mechanisms. Brain vascular ECs contain no fenestrae and undergo very low rates of transcytosis (1). Tight junctions (TJs) and adherens junctions formed between adjacent ECs underlie the physical barrier that impedes paracellular diffusion of ions, macromolecules and other polar solutes (Figure 1.1A-B). Structurally, TJs are composed of combinations of integral membrane proteins including occludins and claudins (which form dimers with their counterparts on adjacent ECs) and cytoplasmic proteins that couple these transmembrane proteins to the actin cytoskeleton (2). The result is a tight interendothelial seal with *in vivo* transendothelial electrical resistances of up to  $1800 \Omega\text{-cm}^2$  (3). In addition to a physical barrier, brain vascular ECs form a selective transport interface between the blood and the brain, similar to that of many epithelial surfaces throughout the body. The luminal and abluminal membranes of brain vascular ECs have polarized expression of transporters, metabolite-degrading enzymes, receptors, ion channels, and ion transporters (4), ensuring that nutrients such as glucose, amino acids, nucleosides, and electrolytes are delivered to the brain from the blood and that solutes and metabolite waste products are effluxed from the brain to the blood (2). The specialization of brain vascular ECs reflects the unique requirements of an organ that demands a homeostatic ionic environment and protection from neuroactive blood-borne solutes.

### *Pericytes*

Pericytes are mural cells embedded within the basement membrane that envelops blood vessels. Pericytes extend thin processes around and along pre-capillary arterioles, capillaries, and post-capillary venules (Figure 1.1A-B) (5). Their morphology varies with their position along the vascular bed, reflecting the existence of subpopulations with diverse functions in blood vessel formation, vessel maintenance and permeability, angiogenesis, clearance of cellular debris, immune cell entry, and cerebral blood flow (CBF) regulation (5-7). As a member of the NVU, pericytes are able to communicate directly with cerebral ECs through gap junctions and with other pericytes via peg-and socket contacts (8,9). The importance of pericytes in the NVU is further illustrated in development, during which pericytes induce polarization of astroglial endfeet around vessels, and in disease, in which pericyte degeneration leads to increased vessel permeability (10). Pericytes have even been shown to have stem cell-like properties making them capable of potentially differentiating into other cell types found in the NVU (11,12).

### *Astrocytes*

Classically, astrocytes have been considered the physical, biochemical, and metabolic support cells of the central nervous system (CNS). Astrocytes are distributed throughout the brain and exhibit heterogeneous, star-shaped, highly branched morphology that varies with their location and, more specifically, on the cell populations with which they interact. Individual astrocytes can extend processes to several neurons and up to 140,000 synapses to modulate neuronal function (Figure 1.1) (13). While individual astrocytes occupy their own non-overlapping spatial domain, they are interconnected with neighboring astrocytes by gap junctions to facilitate long-range signaling (14). In the

context of the NVU, astrocytes are centrally positioned between neurons and ECs, which allows them to respond dynamically to synaptic activity and neuronal metabolism to help regulate CBF. Astrocytes extend endfoot processes to the surface of cerebral blood vessels providing ~99% abluminal vessel coverage (15,16). Endfeet express high levels of aquaporin-4 water channel proteins, which are thought to be critical for perivascular clearance mechanisms via the newly characterized glymphatic system (Figure 1.2) (17). Developmentally, secretion of growth factors from astrocyte endfeet induces TJ formation and upregulates transport system proteins in vascular ECs (18). During adulthood, bidirectional signaling between astrocyte endfeet and brain ECs helps maintain vascular integrity (19-21).

### *Neurons*

In the brain, neuronal processes are in physical contact with the vasculature and these associations mediate a local increase in CBF in response to increased neuronal metabolic demand at that location, a mechanism known as functional hyperemia (see '*Functional Hyperemia*'). In brief, vasoconstriction and dilation are thought to be driven by the contractility of arteriolar smooth muscle cells and capillary pericytes responding to release of neuron- and astrocyte-derived vasoactive substances including COX-2-derived prostanoids (22), nitric oxide (23), vasoactive intestinal polypeptide (24), acetylcholine (25), corticotropin-releasing factor (26), neuropeptide Y (27), and somatostatin (28). Regional regulation of CBF by neurons appears a complex function of the **1)** developmental stage of the brain, **2)** brain region and the populations of neurons served by the vasculature, **3)** presence and nature of glial cells that may serve as local mediators of neuronal stimuli, **4)** duration and magnitude of neuronal activity, and **5)** the effects of

brain injury or disease that may alter any of these other factors. The association of neuronal processes with cerebral vasculature is also important for the development and maintenance of the BBB. During development, vascular endothelial growth factor (VEGF) signaling appears to drive vascular patterning (29); however, neural progenitor cells contribute to the stabilization of the nascent network (30). Post-developmentally, it is likely that neuronal activity continues to participate in the maintenance of the vascular network (31), with astrocytes, rather than neurons, as the chief mediators of cerebrovascular permeability.

#### *Basement membranes*

Secreted proteins make up a specialized extracellular matrix (ECM) that forms the basement membrane between ECs and pericytes and between astrocytes and pericytes (Figure 1.1A). Pericyte coverage of vasculature is discontinuous; in areas of discontinuity, a single basement membrane is shared between astrocytes and ECs. Proteomic studies from rodent vasculature demonstrate that the brain vasculature ECM protein composition differs from that present in the periphery. Even within the brain, basement membrane protein composition varies greatly between large and small vessels (32), providing evidence that the NVU is functionally heterogeneous throughout the brain. Key proteins of the basement membranes include numerous isoforms of ECM proteins such as collagens, fibrillins, laminins, vitronectin, and fibronectin as well as soluble factors (e.g. growth factors and cytokines), enzymes responsible for matrix degradation and processing (including matrix metalloproteases), and proteins known to bind to ECM (e.g. lectins and semaphorins). Both ECM and support protein components of the basement membrane are essential to proper NVU functioning as they directly

mediate the activation state of many receptors on the cellular components of this unit.

Dysfunction and degradation of the basement membrane is associated with several CNS disease states.

### *Microglia and Perivascular Macrophages*

Microglia are the primary immune cells of the brain. Early in development, these yolk sac-derived myeloid precursors seed the brain (33,34) where they develop into highly plastic cells with motile capabilities. During their native resting state, microglia have small cell bodies with numerous long and highly branching processes (Figure 1.1A). Under pathologic conditions, microglia become activated and take on an amoeboid morphology (larger nuclei and cell bodies with shorter processes), produce and secrete numerous cytokines and soluble factors, and become highly phagocytic (35). The activation state of microglia is often considered polarized as an M1 or M2 phenotype, with the cells diverging to either pro- or anti-inflammatory functions, respectively, based on altered expression of cell membrane receptors and secretable factors. However, *in vivo*, there is a wide range of microglial activation phenotypes that reflect the specific insult administered and the state of the surrounding NVU cells. Current research is investigating novel strategies to modulate microglial polarization as a potential therapeutic target (16,36).

Perivascular microglia/macrophages that originate from both CNS resident microglia and bone marrow-derived circulating monocytes also exist in the NVU (33,37). During development, vasculature-associated microglia interact with tip cells on sprouting vessels to facilitate angiogenesis. In the adult brain, perivascular macrophages are likely derived from and replenished by circulating monocytes, and act as a first line of defense

against invading pathogens (38). Perivascular macrophages maintain contact with the other cell types of the NVU, and crosstalk between these cells likely contributes to NVU function and dysfunction. Recent studies employing intravital two-photon microscopy reveal that in several pathological states, parenchymal microglia can migrate to form perivascular cuffs, leading to vascular degradation and disease progression (39-41). In contrast, perivascular microglial phagocytosis is hypothesized to clear neurotoxic substances in Alzheimer's disease (AD; *see Alzheimer's Disease*).

### **1.3. NVU: Intercellular Interactions**

Interactions occur between neural, glial, and vascular components of the NVU in response to physiological stimuli, facilitating activity-dependent regulation of vascular permeability, CBF regulation, and neuroimmune responses. On the whole, these interactions maintain CNS homeostasis. To illustrate this, we highlight their influence on CBF, focusing on mechanisms of functional hyperemia.

#### *Functional Hyperemia*

Cerebral circulation can be regionally modified based on the energy demands of local neural tissue. Temporal and spatial orchestration of increased blood flow to CNS tissue in response to neural activity is termed functional hyperemia (1). To effect delivery of blood substrates such as oxygen and glucose to metabolically active regions of the brain, local groups of neurons and their associated astrocytes signal to smooth muscle cells (SMC) or pericytes and vascular ECs to modify vascular tone. Though neurons are able to contact and signal to the vasculature directly, astrocytes can act as relays between neurons and ECs (42).

In glutamate neurotransmitter-regulated neurovascular signaling, synaptic glutamate released during increased neuronal activity binds to NMDA receptors on nearby neurons and to metabotropic glutamate receptors on astrocytes. Glutamate binding results in intracellular calcium ( $[Ca^{2+}]_i$ ) increases in both neurons and astrocytes, stimulating the release of vasoactive compounds (Figure 1.3) (42,43).

In astrocytes, the increased  $[Ca^{2+}]_i$  activates phospholipase  $A_2$  (PLA<sub>2</sub>) which then produces arachidonic acid (AA). AA can be released at astrocyte endfeet to the contractile elements of vascular walls where it is converted to its metabolite, 20-HETE, which elicits vasoconstriction. As astrocytic AA accumulates, it is also converted to the vasoactive metabolites prostaglandin (PG) and epoxyeicosatrienoic acid (EET), which are released to elicit vasodilation (44,45). Increases in  $[Ca^{2+}]_i$  in astrocyte endfeet can also activate large-conductance calcium-gated potassium channels and stimulate  $K^+$  efflux onto vessels, resulting in vasodilation (46,47). The role of astrocyte  $[Ca^{2+}]_i$  oscillations in neuronal-vascular coupling was demonstrated in experiments showing that blockade of neuronal activity-dependent  $[Ca^{2+}]_i$  elevations within astrocytes impaired the ability of astrocytes to control arteriole tone (48). The specific vasomotor response elicited by increased astrocyte  $[Ca^{2+}]_i$  depends on factors such as local oxygen concentrations and the pre-existing vascular tone (42,49).

In neurons, increased  $[Ca^{2+}]_i$  activates neuronal nitric oxide synthase creating nitric oxide (NO), which induces vasodilation through its action on cGMP in arteriolar smooth muscle cells and has been proposed to modulate astrocyte-vascular signaling pathways via inhibition of EET and 20-HETE (50). As in astrocytes, increased neuronal  $[Ca^{2+}]_i$  activates PLA<sub>2</sub> producing AA. AA's vasoactive metabolites are released to act on

the contractile cells of vascular walls (1,51). Neurons can also modulate neurovascular coupling by signaling directly to vascular smooth muscle cells and ECs. Additionally, numerous vasoactive mediators (acetylcholine, GABA, neuropeptide Y, somatostatin) released from neurons during neural activity have been shown to elicit vasomotor responses (Figure 1.3) (28,42,52).

While the relative contributions of astrocytes and neurons to vasomotor responses vary as a function of brain region and local neural anatomy, the vasoactive mediators released from both cell populations act together either synergistically or antagonistically to precisely regulate CBF within their microdomains (42). Taken together, these observations highlight the extensive communication that must occur between NVU components to match blood flow with regional activity levels.

#### **1.4. NVU: Pathology**

Disease can lead to aberrations in cellular communication between NVU constituents and result in impaired brain function. Here we discuss Alzheimer's disease (AD) and CNS neoplasms, two pathologies with cerebrovascular dysfunction that demonstrate principles of NVU function.

##### *Alzheimer's Disease*

The marked cognitive decline seen in patients with Alzheimer's disease (AD) is associated with neurovascular dysfunction (49) as manifested in impaired clearance of proteins that are widely believed to be toxic, most notably the amyloid  $\beta$  ( $A\beta$ ) peptide.  $A\beta$  is aberrantly formed when the transmembrane receptor amyloid precursor protein (APP) is cleaved by  $\beta$ -secretase and  $\gamma$ -secretases to release soluble  $A\beta$ . Mutations in

genes that either encode the APP substrate or encode proteins involved in its processing to A $\beta$  uniformly produce dominantly inherited forms of AD, indicating the key role of this peptide in the pathogenesis of AD (51). Several isoforms of soluble A $\beta$  monomers can be produced and exist in equilibrium with one another, with hypothesized neurotoxic effects;  $\beta$ -sheet-mediated interactions between these lead to progressive aggregation to form insoluble deposits. These are constituted in the cerebral cortex as amyloid plaques, one of the hallmark lesions of AD, but are also found in and around cerebral blood vessels.

A $\beta$  can be cleared from the brain via enzymatic degradation, EC transport system-mediated clearance, or interstitial bulk flow and perivascular glymphatic clearance into cerebrospinal fluid (CSF) (52). In sporadic late-onset AD in particular, A $\beta$  accumulation is thought to be due to faulty clearance, rather than overproduction (52). Impaired clearance of A $\beta$  across the cerebrovascular endothelium is believed to result in A $\beta$  deposition in and around cerebral blood vessels, a condition known as cerebral amyloid angiopathy. This condition produces a structural weakening of the vasculature that predisposes affected patients to brain hemorrhage.

According to one hypothesis of AD, inflammatory signaling that increases with aging results in increased expression of APP, impairments in its secretion, and deficiencies in axonal transport that depend on microtubules (53); APP and its A $\beta$  cleavage products accumulate in swollen axonal compartments that become leaky due to microtubular failure and resulting transport deficiencies. A $\beta$  cleavage products are eventually extruded through the leaky axonal membranes into the brain interstitial fluid

where they can be taken up and degraded by nearby neurons (54). Alternatively, A $\beta$  will persist in the brain interstitial space and form amyloid plaques (53).

Extruded A $\beta$  can also be taken up by glial cells. Although microglia are spatially associated with neuritic amyloid plaques containing dystrophic axons and dendrites, microglial ablation in two different mouse models of AD did not affect A $\beta$  deposition (55). While microglia do phagocytose aggregated and misfolded A $\beta$  (56), they later extrude it (57) and proponents of the inflammation hypothesis of AD contend that this uptake may be a byproduct of the increased microglial clearance stimulated by nearby degenerating neurites (55). As disease became chronic, senescent microglia that are thought to become hyperreactive initially may demonstrate decreased responsiveness to damage signals over time, allowing peptides and debris to accumulate locally, perhaps creating a “hot spot” that is permissive for plaque formation (53).

The role of astrocytes in AD pathophysiology is poorly characterized. While some studies have demonstrated that astrocytes take up and degrade A $\beta$ , others have shown that astrocytes actually produce and secrete high levels of it. As in the case of microglia, these seemingly contradictory findings may reflect different astroglial activation states. Astrocytes may take up and degrade A $\beta$  in relatively newly formed senile plaques (58), but this may decline as AD progresses, perhaps as local cytokines and A $\beta$  itself activate astrocytes to produce and secrete A $\beta$  in a feed-forward mechanism (59,60). Importantly, changes in astrocytes in AD have been linked with the development of perivascular A $\beta$  deposits (61) and are likely to have more widespread consequences as astrocytes fail to survey and occupy their territorial domains.

### *NVU pathology in neoplastic disease*

Another example of cerebrovascular dysfunction may be found in CNS neoplasms, including both primary (tumors originating within the CNS) and secondary (metastatic) tumors. In both conditions, neoplastic cells early in disease can survive within the perivascular space of the NVU, and later remodel, destroy and produce new vasculature with aberrant NVU components and function (62). Understanding the NVU in neoplastic disease will open up novel treatment strategies, as this specific niche is critical for tumor development and drug delivery.

Gliomas, tumors arising from glial cells, provide an optimal example of NVU pathology in CNS malignancies. Glioma cells in the perivascular space can migrate within perivascular spaces and are in direct contact with the NVU basement membrane(s) and its associated soluble factors. These components promote glioma development by: **1)** providing traction support for migration utilizing proteins such as collagens, fibronectin and vitronectin, **2)** promoting survival, proliferation, and maintaining multi-potency via activation of pathways including TGF-beta, cytokine, notch, sonic hedgehog and ECM signaling, and **3)** facilitating radio- and chemotherapy resistance (63-68). Furthermore, glioma cells can produce and secrete additional ECM and growth factor proteins as well as matrix metalloproteinases to loosen the ECM for invasion (69). A delicate balance of cell adhesion for traction force coupled with ECM degradation for motility is necessary for successful infiltration. Glioma cells overexpress potentially targetable receptors, such as integrins, to mediate these processes.

In addition, complex molecular signaling and crosstalk between glioma cells and the cells of the NVU also dictate tumor survival and progression (70-73). These cell-cell interactions promote tumorigenic processes and disrupt normal NVU functions.

Displacement of normal astrocyte endfeet promotes vascular “leakiness” through downregulation of TJ expression (53) and disrupted regulation of vascular tone. Using acute slices and  $\text{Ca}^{2+}$ , Watkins *et al.* showed that perivascular glioma cells could even take over the regulation of vascular tone in a  $\text{K}^+$ -dependent manner (69).

Beyond disrupting the NVU by individual or small clusters of neoplastic cells, larger tumors promote neovascularization to ensure adequate oxygen and metabolic support; these newly induced vessels have abnormal NVU structure and function (Figure 4) (74). GBM cells release pro-angiogenic growth factors such as VEGF, which activates VEGF receptors on ECs, inducing them to sprout and extend into the tumor (75,76). Newly formed vessels can lack structural components of the NVU such as adequate pericyte coverage, normal EC walls and TJs, and normal basement membrane composition and have variable permeability (77,78). Understanding the increased, yet heterogeneous, permeability of tumor vasculature is essential for optimizing drug delivery to tumors. In clinical practice, CNS tumor vascularity is assessed by a magnetic resonance imaging (MRI)-derived parameter,  $\text{K}^{\text{trans}}$ , which reflects both vascular surface area and permeability. The role of VEGF in tumor-associated permeability can be seen in the decrease in  $\text{K}^{\text{trans}}$  that occurs after treatment with the VEGF inhibitor, bevacizumab (Figure 1.4D) (79).

In summary, the NVU serves as the gateway to the brain. Understanding its components, development, maintenance, functions, and pathologic conditions will provide essential insights and tools needed to treat essentially all diseases that affect the brain.

## Figures

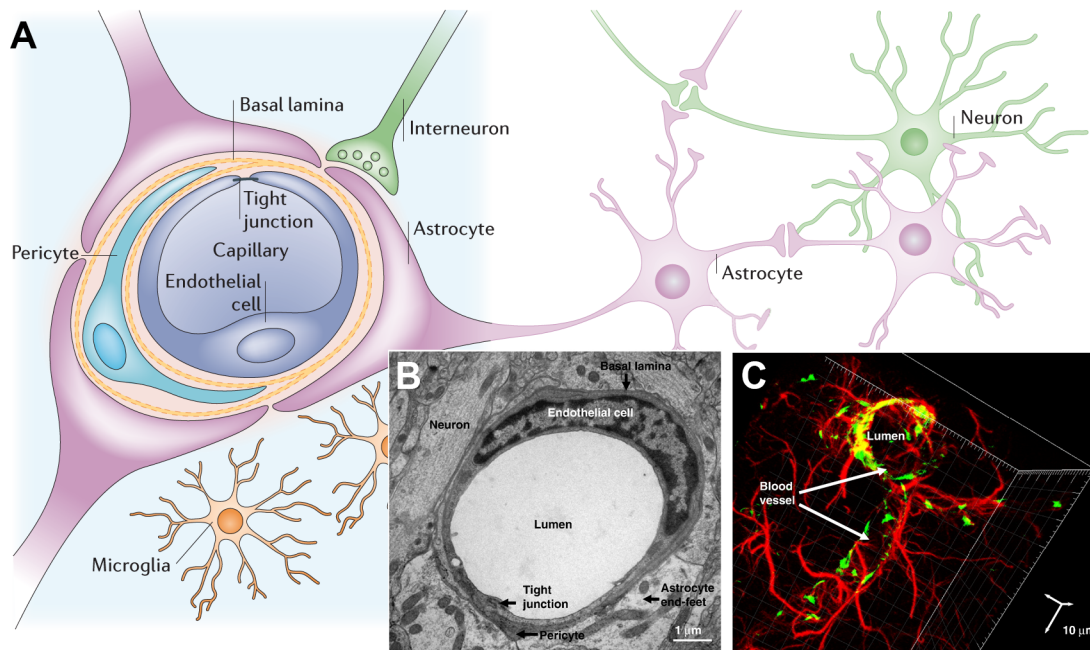


**Figure 1.1. Anatomical structure of the neurovascular unit (NVU).** A) A schematic representation of a capillary cross-section within a single neurovascular unit demonstrates the following important features: **1)** Specialized brain endothelial cells line cerebral vessels **2)** Tight junctions between endothelial cells restrict paracellular diffusion and effectively “seal” the vessels **3)** A continuous basal lamina/basement membrane encases endothelial cells. Pericytes are embedded within this matrix, situated between endothelial cells and astroglial endfeet **4)** Astrocytes are centrally positioned within the brain parenchyma. These cells extend processes that communicate with local neurons and synapses and also extend foot-like processes that encase cerebral vessels. Astrocytes are therefore ideally localized to sense and respond to both neuronal and vascular activity **5)** Resident microglia use long cellular processes to survey their microenvironment and can quickly respond to insults at or near the NVU **6)** Local interneurons innervate cerebral vasculature and can induce vessels to change their tone based on incoming neuronal

afferent signals (28) [adapted with permission from Macmillan Publishers Ltd: (Nature Reviews Neuroscience), Abbott *et al.* 2006 (80)]. **B)** Electron micrograph of a capillary cross-section in rat brain. **C)** 3D reconstruction of immunofluorescent NVU images taken on a confocal microscope demonstrating von Willebrand Factor reactivity (endothelial cells) and glial fibrillary acidic protein reactivity (astrocytes) outside the vascular wall [B and C reprinted from *Biochimica et Biophysica Acta (BBA) – Biomembranes*, **1788**:4, Weiss *et al.* The blood-brain barrier in brain homeostasis and neurological diseases, 842-857, Copyright (2009), with permission from Elsevier (81)].

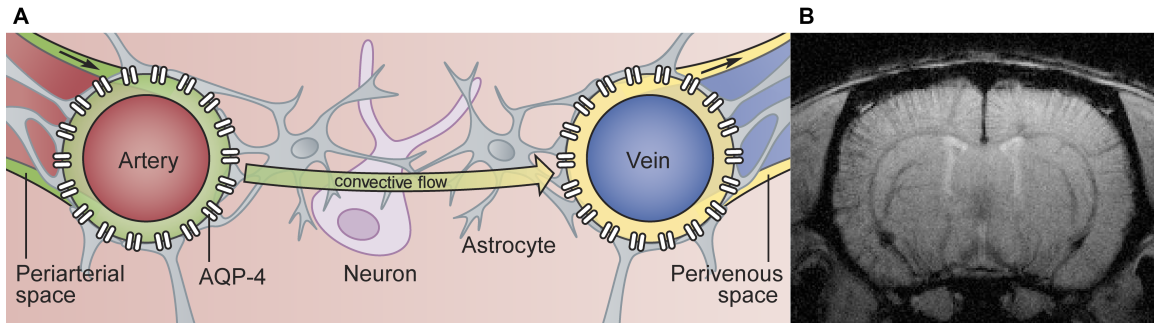


**Figure 1.2. Perivascular clearance in brain: The Glymphatic System.** **A)** The glymphatic system consists of directional fluid flux along the abluminal surface of brain endothelium (black arrows) beneath astrocyte endfeet, which express high levels of the water channel aquaporin 4 (AQP-4). Convective movement of extracellular fluids and solutes help drive clearance in the brain parenchyma, with drainage (at least in part) into the perivascular space [adapted from *The Lancet Neurology*, **14**:10, Iliff *et al.* Implications of the discovery of brain lymphatic pathways, 977-979, Copyright 2015, with permission from Elsevier (82)]. **B)** Perivascular Virchow Robin spaces may be demonstrable using MRI.  $T_2^*$ -weighted MRI image shows decreased signal along penetrating arterioles in the cortex 2h after an intrathecal cisternal injection of an iron oxide contrast agent (unpublished pilot data).

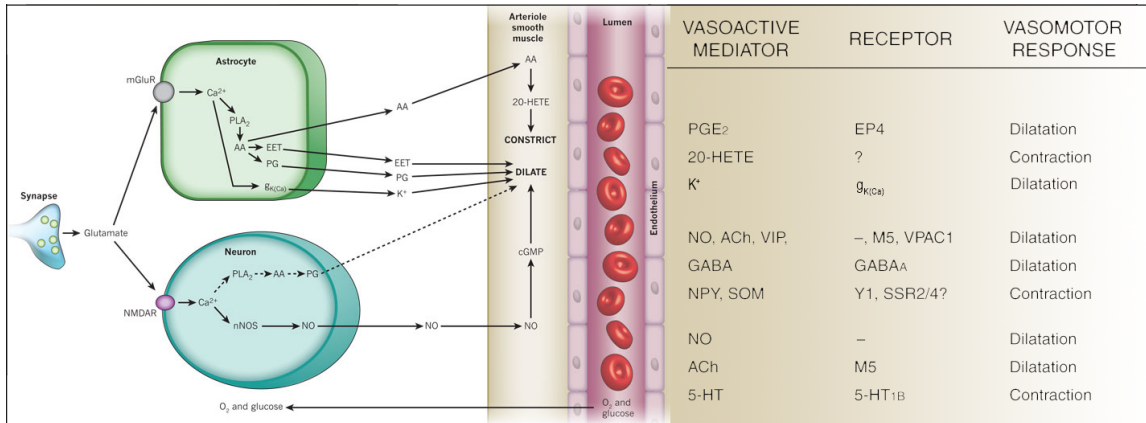


**Figure 1.3. Neurovascular unit components act in concert to regulate cerebral blood flow.** Glutamate is released during increased neuronal activity and binds receptors on astrocytes and neurons, inducing rises in intracellular calcium ( $\text{Ca}^{2+}$ ) levels.  $\text{Ca}^{2+}$  activates precursors that stimulate release of vasoactive mediators that induce cerebral vessels to constrict or dilate after binding their vascular receptors. This concerted activity between neurovascular unit components allows precise regulation of vasomotor responses to affect delivery of oxygen and glucose to brain regions with increased neuronal activity

[Adapted with permission from Macmillan Publishers Ltd: (Nature), Attwell *et al.* 2010 (42) and The American Physiological Society: (Journal of Applied Physiology), Hamel, E. 2006 (83)].

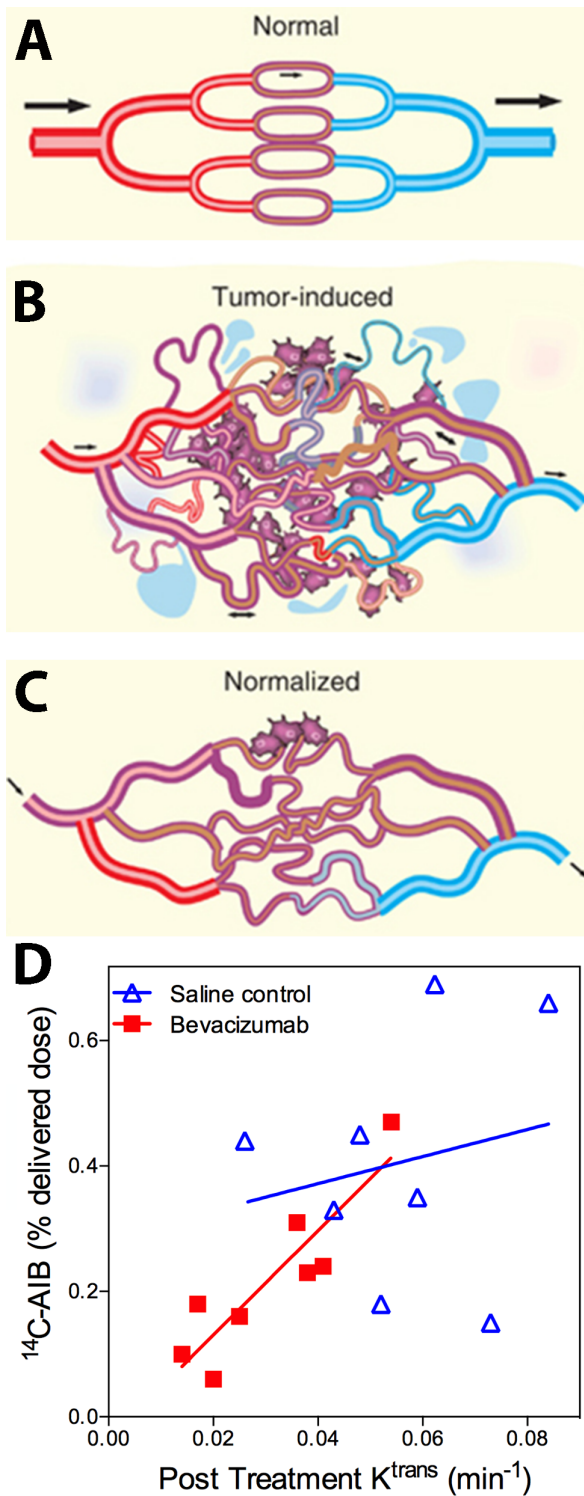


**Figure 1.4. Antiangiogenic therapy normalizes tumor vasculature.** **A)** Normal capillary bed demonstrating typical physical interactions between arterial and venous circulation. **B)** Tumor-secreted angiogenic factors induce neovascularization, resulting in

abnormally tortuous and leaky vascular beds. Blood flow through these capillaries is decreased and inconsistent, possibly resulting in tissue hypoxia. **C)** Treatment with anti-angiogenic therapy, such as the vascular endothelial growth factor (VEGF) inhibitor bevacizumab, normalizes vascular beds and reduces their permeability [Adapted with permission from Macmillan Publishers Ltd: (Oncogene), Farnsworth et. al. 2014 (74)]. **D)** Once vascular beds are normalized with bevacizumab treatment, MRI-derived  $K^{\text{trans}}$  measurements of vascular permeability correlate linearly with the concentration of  $^{14}\text{C}$ -AIB, a tracer with unidirectional permeability across the blood-brain barrier [Adapted with permission from Biomed Central: (Fluids and Barriers of the CNS), Pishko *et al.* 2015 (79)].

## **Chapter 2. Introduction to ferumoxytol**

### **2.1 Introduction**

The BBB properties described in Chapter 1 serve to protect the brain from toxins, modulate the entry of metabolic substrates, and provide an ultra-stable extracellular fluid for CNS neurons that is compositionally different from that in the circulation blood plasma. As a result of these properties, drug delivery to the brain is highly restrictive and does not occur as readily as drug delivery to peripheral organs, which are supplied by sinusoidal and fenestrated vasculature. In particular, any drug or compound that is not extremely small and very lipophilic is unlikely to reach the brain in therapeutically relevant concentrations when delivered intravenously. Delivery to the brain becomes less restricted during BBB dysfunction, which can occur during inflammatory CNS pathology. Contrast-enhanced MRI allows researchers to identify where the BBB becomes dysfunctional in the brain; in this sense, a pathologically leaky BBB can serve as a diagnostic tool by allowing us to visualize where contrast agent extravasation occurs.

MRI is an essential component of clinical management and has preclinical utility for imaging numerous CNS pathologies. Generally, MRI is useful for non-invasive visualization of numerous tissues of the body, but it is especially superior in brain imaging to other imaging modalities for evaluating pathology. MRI has advantages over these other imaging modalities (e.g. positron emission and computed tomography; PET, CT) as it allows for higher resolution imaging and soft tissue contrast, and does not make use of ionizing radiation. The neuroimaging field has been steadily progressing as more advanced MRI pulse sequences, analysis paradigms and more powerful magnets have come to the fore. This progress is marked by improved imaging techniques that have

substantially increased the spatial and temporal resolution of images, allowing for more accurate detection and localization of brain lesions such as tumors (84). These improvements, in turn, yield improved diagnostic, response assessment, and surgical planning capabilities in the field of neuro-oncology.

To enhance the visibility of anatomical structures and pathologies in tissues on MRI, exogenous contrast agents are used. Small advancements in MRI contrast media have been made, though gadolinium-based contrast agents (GBCA) remain the most widely used MRI contrast media for clinical use in the United States (84). These GBCA agents provide excellent contrast that, while sensitive, is non-specific. After intravenous injection, GBCAs extravasate from cerebrovasculature with disrupted blood-brain barrier (BBB) (see Chapter 1; *Vascular Endothelial Cells*) and from those small areas of normal brain lacking a BBB. In these extracellular spaces, the paramagnetic GBCAs will accelerate tissue proton relaxation times, resulting in increased contrast on MR images. Thus, the contrast produced by GBCA is in large part due to intravascular localization and/or passive leak across dysfunctional cerebrovasculature (85). Of note, concerns regarding impaired gadolinium elimination from the brain have recently been raised (86-89). Further, patients with renal dysfunction that receive GBCA are now known to be at increased risk of developing nephrogenic systemic fibrosis (NSF) (90-92), underscoring the need for alternative contrast agents (93,94).

Ferumoxytol ultrasmall superparamagnetic iron oxide nanoparticles are poised to act as an alternative and supplementary contrast agent to traditional GBCAs (95-98). These nanoparticles are FDA-approved for iron replacement therapy in patients with iron deficiency anemia and can be administered to patients with impaired kidney function

(99). Ferumoxytol nanoparticles are structurally distinct from GBCA and behave differently in the cerebrovasculature and in the brain parenchyma. Early after administration, these nanoparticles act as a blood pool agent in the vasculature. At later time points, to varying degrees, they can act as markers of inflammation at CNS lesions where they are taken up by macrophages and activated astroglial cells (100,101). As GBCAs offer no information regarding the inflammatory state of a lesion, ferumoxytol nanoparticles can act as informative supplements to GBCA imaging. Moreover, ferumoxytol can also act as an alternative contrast agent in patients with impaired kidney function. Therefore, the study of how ferumoxytol behaves in the brain and interacts with pathological lesions is of significant clinical interest. This chapter is devoted to familiarizing the reader with basic concepts of MRI, with a particular focus on the clinical applications of GBCA and ferumoxytol contrast agents in patients with neurological lesions.

## **2.2 Fundamental principles of magnetic resonance imaging**

Here I describe some of the fundamental principles underlying MRI for the lay reader. The purpose of this section is not to provide a complete theory of MRI, but rather to provide the reader with enough knowledge of the vocabulary and underlying physics to give context and understanding of ideas discussed in later chapters.

Typically, MRI is used to visualize positively charged hydrogen nuclei,  $^1\text{H}$ , which are abundantly present throughout the body in water and fat (though some MRI applications make use of nuclei other than  $^1\text{H}$ ). These protons have non-zero angular momentum and “spin” about their rotational axis, in random directions, generating many

dipole moments with a net electromagnetic field of zero. The frequency of this spin, the Larmor frequency, is determined by the gyromagnetic ratio of the nucleus and the strength of the external magnetic field ( $B_0$ ) to which the nuclei are exposed (102). The strength of  $B_0$  in MRI is the field strength of the operating system; most commercially available and clinically relevant scanners range operate at field strengths of 1.5 Tesla (T) or 3T. The experiments in this dissertation were conducted using an ultrahigh field strength 12T scanner, the use of which is restricted to animal research (mainly due to bore size).

### *Tissue Magnetization*

After the application of an external magnetic field, the randomly oriented and spinning  $^1\text{H}$  nuclei will begin to align parallel and antiparallel to  $B_0$ . Following the Boltzmann distribution, more  $^1\text{H}$  nuclei will line up parallel to  $B_0$  than antiparallel. This creates a net magnetization,  $M_0$ , in the direction of  $B_0$  (which is defined as the longitudinal or z-axis in a 3-dimensional space; Figure 2.1) (103).

The aligned  $^1\text{H}$  nuclei will now not only rotate about their own axis, but will also precess about the axis of  $B_0$  in a frequency defined by the Larmor equation (the so-called “Larmor frequency”). For the precessing nuclei to produce a signal that can be measured, the net magnetization must be tipped away from its longitudinal axis. This is accomplished using oscillating radiofrequency (RF) magnetic field pulses. For the oscillating RF pulse to affect the protons, the frequency of the transmitted pulse must match the frequency at which the nuclei precess (this matching of frequencies is termed *resonance* and is the basis of the name “magnetic *resonance* imaging”). The pulses are applied at durations and intensities that produce a specified tilting of  $M_0$  away from the

longitudinal axis to a new prescribed angle. A  $90^\circ$  pulse, for example, would flip  $M_0$  into the transverse plane (xy-axes). Thus, RF pulses are transmitted into the sample to flip the longitudinal magnetization of the nuclei into the transverse plane, generating a detectable signal in a nearby coil of wire according to Faraday's Law (104).

To derive spatial information from the scan, we use an applied magnetic field that is spatially varied. This magnetic field *gradient* is used to make particular groups of nuclei precess at different Larmor frequencies. These Larmor frequencies are proportionally related to the strength of a locally experienced magnetic field (105). The maximum available signal strength, in turn, is related to the local spin density. Interestingly, this relationship helps explain the drive to use and develop ultrahigh field strength scanners; signal strength depends on  $M_0$ , which depends on the size of  $B_0$ . With high field scanners, more protons can be aligned along the  $B_0$  axis, which increases signal in MR images.

### *Relaxation Times*

After the RF excitation pulse is turned off, nuclei will return to their thermal equilibrium state (a process termed "relaxation") where more spins will again align with  $B_0$  along the longitudinal z-axis. Two independent relaxation processes occur here simultaneously: 1) recovery of longitudinal magnetization along the z-axis (Figure 2.2A) and 2) decay of coherent transverse magnetization along the xy-axes (Figure 2.2B). Each process follows an exponential time course characterized by the relaxation time constants  $T_1$  and  $T_2$ , respectively.

Importantly,  $T_1$  and  $T_2$  are both *inherent* properties of tissues. Both constants are used to characterize tissues in MRI.  $T_1$ - and  $T_2$ -weighted images are produced from MRI

sequences that make use of different RF pulse parameters (see *Weighted Images*, below). Varying the length of RF pulse parameters allows either the inherent  $T_1$  or inherent  $T_2$  properties of the tissue to (predominantly) dictate the contrast and brightness within the image. Generally,  $T_1$  and  $T_2$  weighted images can be visually differentiated by which tissue structures they highlight. To simplify greatly,  $T_1$ -weighting highlights protons within fatty tissues,  $T_2$  weighting highlights protons of free water, (102). As such, CSF will appear dark on  $T_1$ -weighted images but bright on  $T_2$ -weighted images (102,104).

Another time constant,  $T_2^*$ , also describes the decay of transverse magnetization along the xy-axes but takes into account not only the inherent  $T_2$  properties of the tissue, but also any inhomogeneities present in the local magnetic field. Such inhomogeneities arise from non-uniformity within the main magnet itself and also from the susceptibility effects arising from nearby materials such as blood, metal or air (102) with different susceptibilities. In general,  $T_2^*$ -weighting is able to highlight the presence of blood products, calcification and also iron deposits (106). The relationship between  $T_2^*$  and  $T_2$  relaxivity is complicated, but both are strongly related to the concentration of susceptibility-inducing contrast agents (100,107).

### *Weighted images*

Image weighting in MRI refers to the application of particular RF pulse sequences that are designed to “weight” the signal intensity towards a longitudinal or transverse relaxation time (e.g.  $T_1$ ,  $T_2$ ). Importantly, because of imaging speed considerations and instrumentation limitations, *both*  $T_1$  and  $T_2$  relaxation will affect the final acquired MR image. In general, weighting involves manipulation of three pulse sequence parameters: repetition time (TR), echo time (TE), and the flip angle of the RF excitation pulse (102).

TR refers to the time between RF excitation pulse administrations. If TR between pulses is short, then excitatory RF pulses are being delivered rapidly, which in turn limits the recovery of longitudinal magnetization along the z-axis (Figure 2.2A). Areas of the tissue being sampled that have short  $T_1$  will recover more rapidly at a given TR relative to other areas, producing signal hyperintensity (brightness) that allows discrimination of these structures relative to those of long  $T_1$ . This short TR, along with a short TE, will effectively weight the signal in relation to the tissue's  $T_1$  values, allowing the reader to discriminate between  $T_1$  properties of the tissue.

For T2-weighting, a long TR effectively removes this  $T_1$  effect and a long TE effectively weights the signal in relation to the tissue's  $T_2$  values as follows: after an RF pulse is delivered, protons precess at frequencies related to the local fields and both transverse and longitudinal magnetization will begin immediately. For a spin-echo sequence, a  $180^\circ$  RF pulse can then be applied to refocus signal lost due to local field inhomogeneity in the transverse plane (Figure 2.2B). The time it takes from the initial RF pulse until the protons are in phase with one another again is referred to as TE. Areas of the tissue being sampled that have short  $T_2$  will result in more rapid signal loss in the transverse plane at a given TE relative to other areas, producing signal hypointensity, allowing the reader to discriminate between  $T_2$  properties of the tissue.

### *Clinical magnetic resonance imaging contrast agents*

Enhancement on non contrast-enhanced MRI depends on endogenous signal differences between pathological and normal brain tissue that vary depending on the type, location, and size of a given lesion and the amount of inflammation the lesion has caused in the

surrounding tissue. In the clinic and in research, exogenous MRI contrast agents are often used to enhance the visibility of anatomical structures and pathologies in tissues. Here I describe the use of linear and cyclic GBCA versus iron-based contrast agents in the CNS. Contrast agent identity can inform clinical MRI interpretation; due to marked differences in size and chemistry, GBCAs and ferumoxytol nanoparticles demonstrate different but biologically significant patterns of enhancements in the brain and around the cerebrovasculature. The fidelity of enhancement depends strongly on BBB permeability as well as contrast dosage, route of administration, and imaging timing.

Contrast agents enhance the visibility of anatomical structures and pathologies in tissues by affecting the  $T_1$  and  $T_2$  nuclear relaxation rates of  $^1\text{H}$  protons in adjacent and compositionally varying tissues (Figure 2.3) (108). In the sense that these agents are acting indirectly by catalyzing  $^1\text{H}$  relaxation processes rather than themselves becoming visible, MRI contrast agents are fundamentally different from CT or PET imaging agents (105). In general, contrast agents shorten the  $T_1$  and  $T_2$  times of water protons that are near the contrast agent. The magnitude of signal enhancement depends on the concentration of the contrast agent present, the relaxivity properties of that contrast agent (where relaxivity is defined as the amount of [1mmol/L] contrast agent needed to increase the longitudinal ( $R_1$ ) and transverse ( $R_2$ ) relaxation rate constants of  $^1\text{H}$  protons in water) (105), and the properties of the sample being imaged local to the contrast agent. Among other factors, the relaxivity properties of any given contrast agent is related to its size, structure, physiochemical properties and its concentration and distribution within tissues.

To be appropriate for clinical use, contrast agents must be thermodynamically stable and non-toxic. The clinical application of a given contrast agent depends on several factors including its biodistribution after administration, relaxivity and susceptibility effects, plasma half life, and mechanism(s) of excretion and metabolism. These properties, in turn, are related to the size and structure of the agent, as well as how easily it can influence and interact with nearby  $^1\text{H}$  protons. Ferumoxytol has greater relaxivity properties than GBCAs (109). Many classes of MRI contrast agents with wide clinical applications exist, including blood pool agents, extracellular agents and hepatobiliary-enhancing agents, though many are experimental and not approved for clinical use (105). Commonly, a three-compartment model is used to describe contrast agent localization after injection: intravascular, the extravascular extracellular space (EES) or the extravascular intracellular space (EIS) (Figure 2.4) (110). In this model, the  $^1\text{H}$  protons in whichever compartment the contrast agent resides in will experience effects from that contrast, producing signal changes that can be detected with MRI. In normal brain, contrast agents are *physically prevented* from traversing from the blood into the extravascular space by the TJs of cerebrovascular ECs (see Chapter 1; *Vascular Endothelial Cells*). If BBB breakdown occurs, this barrier no longer precludes contrast entry into the CNS. Thus, pathological BBB disruptions can be detected with contrast-enhanced MRI. Below, I briefly discuss GBCA and iron oxide nanoparticles, two classes of contrast that behave differently in these compartments over time. A number of other MRI contrast agents exist and are used for experimental applications, but are not discussed here.

The first clinically-approved MRI contrast agent was a complex of the rare earth element gadolinium and diethylenetriaminepentaacetate (Gd-DTPA; Magnevist) (111). With seven unpaired electrons, gadolinium is the most potent lanthanide element in the periodic table for  $T_1$  relaxation. Ideally, gadolinium chelate is excreted very quickly from the body via the kidneys and has few allergic or adverse effects --- all of which make it a useful MRI contrast agent. The gadolinium ion ( $Gd^{3+}$ ) is toxic, so GBCA are generally chelated with either linear or macrocyclic structured chelates (84,108). Linear chelates have been shown to be less stable *in vivo*, leading the European Medicines Agency to suspend or limit their clinical use (89). In a more recent discovery, gadolinium has been shown to accumulate in the dentate gyrus and globus pallidus of patients that have received repeated linear GBCA administrations (87,88,112-116), prompting the International Society for Magnetic Resonance in Medicine to revise their recommendations regarding its use in particular patient populations and in research (86). Specifically, the society recommended that healthcare professionals limit GBCA administration to those cases where the contrast provides information that is of absolute necessity and that use of repeated GBCA administration in established treatment protocols be reconsidered (<http://www.fda.gov/Safety/MedWatch/SafetyInformation/SafetyAlertsforHumanMedicalProducts/ucm456012.htm>).

A second class of less commonly used contrast agents is ultrasmall superparamagnetic iron oxide (USPIO) nanoparticles. These agents have also been available in several different formulations over the years (109,117). Compositionally, the agents are built upon a magnetite ( $Fe_3O_4$  or  $\gamma-Fe_2O_3$ ) core that is stabilized with a

polymeric coating in a colloidal suspension (118). The surrounding polymeric coating increases the stability of the core in aqueous mediums and decreases opsonization and endocytosis (109,117,119). The coating identity varies between agents and each coating imparts unique behavior to the particle (109). The coating also provides sites for conjugation of specific molecules that can effectively “vectorize” the nanoparticles to specific targets (109,120). Though iron [Fe(II), Fe(III)] atoms alone are considered ferromagnetic, iron oxide contrast agents are able to act as superparamagnetic contrast agents due to a cooperative alignment of the electron spins of iron electrons within the magnetite crystals, which creates a large magnetic dipole moment that far surpasses the effects of paramagnetic Fe atoms alone. This large magnetic dipole creates inhomogeneities in the local magnetic field experienced by tissue protons, which decreases  $T_1$  and, to a greater extent,  $T_2$  relaxation times (102). In general, iron oxide nanoparticles are classified according to their size and effective hydrodynamic diameter: standard superparamagnetic iron oxide nanoparticles (SPIOs; >50nm), ultrasmall superparamagnetic iron oxide nanoparticles (USPIO; <50nm). The particles also have favorable metabolism properties as long as the recommended dose is not exceeded; as the iron in the core is biocompatible, the iron simply enters the normal iron metabolism pathways for use or degradation (117). In the event of iron overload, normal iron metabolism pathways cannot be used effectively (121).

### **2.3 Use of gadolinium-based contrast agents in the brain**

Most of the currently available clinical MRI agents are gadolinium-based. Over 200 million doses of GBCAs have been administered worldwide since 1988 (84,85,108).

Studies as far back as 1985 suggested that GBCAs held great utility for CNS imaging due to the fact that GBCAs did not appear to be able to cross an intact BBB (or at least resulted in extravasation that was below the limits of detection; see *Impaired Gadolinium Elimination*) (111,122). This meant that, for the many CNS disorders with pathological BBB breakdown, GBCAs would be an excellent candidate to localize dysfunctional vasculature and possibly to guide therapy.

#### *Mechanisms of gadolinium-based enhancement*

Following intravenous administration, GBCAs distribute throughout the peripheral and cerebral vasculature. The pharmacokinetics, biodistribution, elimination rates, and relaxivity properties vary between GBCAs based on the physiochemical properties of the chelate and the particular GBCA used (85). Many of the GBCAs commonly used for CNS imaging are EES agents. In general, these low molecular weight GBCAs quickly equilibrate between intravascular and extracellular/interstitial compartments, in a volume transfer rate constant defined by  $K^{\text{trans}}$  (Figure 2.4) (79,110). Recall that in the CNS, GBCAs are only able to extravasate from the cerebrovasculature and provide parenchymal enhancement if BBB dysfunction is present. There must also be sufficient extracellular space available in which the GBCA can localize. If these conditions are met, extravasation occurs rapidly and leads to  $T_1$ -shortening (decrease in  $T_1$  relaxation time) and enhancement (brightening) on  $T_1$ -weighted MRI (108,114). Further, this extravasation is the result of passive GBCA leak across disrupted endothelial TJs and, as such, is not specific to any biological phenomenon other than the presence of leaky vasculature; therefore, similar patterns of enhancement are observed across biologically diverse neurological and oncologic lesions. Finally, if there is inadequate cerebral blood

flow to the area of interest, GBCA delivery (and thus extravasation) is attenuated or even completely abrogated in cases such as stroke. As such, gadolinium-based enhancement reflects the vascularity of the particular brain area being imaged and also the pathological state of the BBB.

#### *Impaired Gadolinium elimination*

Ideally, elimination of GBCA after administration is rapid --- and complete. The principle excretion pathway for most GBCAs is renal though some agents are excreted through hepatobiliary pathways (85). While renocompromised patients are at particular risk for impaired GBCA elimination, recent reports have demonstrated that gadolinium can accumulate in the brain even in patients with intact BBB and normal renal and hepatobiliary functions. Two elimination-related phenomena have led the medical and research communities to recently question the safety of some GBCAs: NSF and gadolinium retention in the brain.

NSF is a potentially lethal condition characterized by fibrosis of the skin and internal organs. The first report of skin fibrosis in patients with compromised renal function that received repeated or high dosages of GBCAs appeared in 2000 (123). There are no effective treatments for the disease and death is due in part to restricted respiratory movements caused by thoracic fibrosis (124,125). A causal relationship between GBCA administration and the development of NSF was established in 2006 (126,127), though the exact mechanism underlying disease development remains unknown. Before this time, GBCAs were commonly administered at 2-3 times their recommended dose to improve image quality and increase enhancement (100). A 2007 study following hemodialysis patients found that patients with NSF-related skin fibrosis had a 2-year

mortality rate of 48% versus 20% for those without NSF (adjusted HR 2.9, 95% CI: 1.4-5.9). Patients that were exposed to GBCA were nearly 15 times more likely to have skin fibrosis compared to patients with no GBCA exposure (128). NSF is associated with renal dysfunction; affected patients cannot adequately excrete the administered GBCAs (126). Over time, the toxic gadolinium ion is thought to gradually dissociate from its stabilizing chelate and be deposited in various tissues throughout the body (129). Cowper *et al.* have suggested that gadolinium then activates circulating fibrocytes, thereby inducing tissue fibrosis (90-92). The risk for NSF development is markedly increased for the linear GBCA chelates, which dechelate more readily than their macrocyclic counterparts (130). As a result, GBCAs have been reclassified as low, intermediate, or high risk for NSF based on 1) the surrounding chelate structure (linear or macrocyclic) and 2) the gadolinium ion (ionic vs. non ionic) (131). In new guidelines issued (2013), the European Society of Urogenital Radiology used these GBCA risk classifications to suggest appropriate contrast agents for patients based on their glomerular filtration rates (130,132). Thus, patients with kidney dysfunction or severe chronic kidney disease (CKD) (stages 4-5) that are at risk for NSF cannot receive GBCA and require a safe, alternative contrast agent (118).

In 2014, Kanda *et al.* discovered that patients who had received multiple GBCA-enhanced brain MRI scans showed increased signal intensity in specific brain regions (dentate nucleus and globus pallidus) on subsequent *unenanced* T<sub>1</sub>-weighted MR images (133). The presence of sustained enhancement suggested that repeated GBCA administration might be resulting in 1) impaired GBCA elimination (even in patients with healthy kidney function) and/or 2) preferential deposition of GBCA in anatomically

specific regions of brain. The next year, McDonald *et al.* confirmed the presence of dose-dependent gadolinium deposits in post-mortem brain tissues of patients who had received multiple GBCA doses for MRI using inductively-coupled plasma mass spectrometry (87). Patients with brain tumors or multiple sclerosis (MS) lesions require repeated GBCA-enhanced imaging sessions for diagnosis and to assess lesion progression over time (134). Though tempting to attribute such a finding to the pathophysiological BBB function that characterizes these patient populations, 18-42% of the detected gadolinium was found to have crossed an apparently intact BBB (87) and gadolinium deposition has since been demonstrated in healthy adults without intracranial abnormalities (135). Furthermore, both macrocyclic and linear GBCAs have been shown to accumulate in rat brain, though the linear formulations deposit more robustly than the macrocyclic agents (136). Why gadolinium preferentially accumulates in particular brain structures and the clinical significance of these deposits remains unknown. As of 2017, the FDA has stated that there is not yet any evidence that the gadolinium deposits are detrimental or have a clinical effect ([www.fda.gov/Drugs/DrugSafety/ucm559007.htm](http://www.fda.gov/Drugs/DrugSafety/ucm559007.htm)) (131), though others have demonstrated that enhanced delivery of gadolinium may increase the frequency of delayed seizures (137,138). The recommendation from the National Institutes of Health to clinicians is to carefully consider whether the use of GBCA is completely necessary and to consider the use of alternatives when available (131). On December 14<sup>th</sup>, 2017, the United Kingdom's Medicines and Healthcare products Regulatory Agency announced that two of the four linear chelate GBCAs would be pulled from the market in light of the numerous reports of GBCA retention ([35](https://www.gov.uk/drug-safety-</a></p></div><div data-bbox=)

update/gadolinium-containing-contrast-agents-removal-of-omniscan-and-iv-magnevist-restrictions-to-the-use-of-other-linear-agents).

## **2.4 Ferumoxytol as an alternative MRI contrast agent**

Ferumoxytol has several unique physiochemical and pharmacokinetic properties that lend it to temporally disparate CNS imaging applications first in the vasculature and then in the brain parenchyma. Cerebrovascular imaging is possible early after ferumoxytol injection, as the nanoparticle has a long blood-pool phase relative to GBCAs.

Parenchymal and vessel wall imaging is possible after a delay of 2-48h if there is pathological and/or macrophage-based CNS inflammation present. Importantly, ferumoxytol is well positioned to act as a supplemental contrast to GBCAs in many clinical MRI endeavors, or even as a replacement in some cases.

### *Properties of Ferumoxytol*

Though originally developed for MRI contrast, ferumoxytol holds FDA-approval only for iron replacement therapy under the brand name Feraheme (95), as of 2017 (99,119). The nanoparticle has a molecular weight of ~750kD and a hydrodynamic diameter of 30 nm, making it much larger than traditional GBCAs (98). The polyglucose carboxymethylether coating surrounding the superparamagnetic iron core prevents mast cell degranulation after intravenous (IV) administration and increases the blood plasma half-life of ferumoxytol (~14h) (139,140). The larger size and modified carbohydrate coating of ferumoxytol confer a prolonged intravascular residence time (~14-21h) to the nanoparticle relative to traditional GBCA (~60 min depending on kidney function, dose, and particular agent) (119,141) (Figure 2.5). The lack of early extravasation and strong

susceptibility effects of ferumoxytol make it particularly useful for vascular MR imaging as the prolonged vascular signal allows for extended image acquisitions and improved image resolution not possible with GBCA (139,142). Further, repeat imaging can be performed if necessary without the need of additional contrast injection. Ferumoxytol contains less labile iron than any other parenteral iron formulation and is intended for IV administration (98). In 2015, the FDA required a black box warning be placed on ferumoxytol after anaphylactic reactions occurred in 79 patients receiving the drug as an undiluted bolus (143) (<https://www.fda.gov/Drugs/DrugSafety/ucm440138.htm>). Fifty-three of these patients had a history of drug allergies. The European Medicines Agency Pharmacovigilance Risk Assessment Committee came to a similar conclusion in 2014, but held that the benefits of ferumoxytol outweighed the risks ([http://www.ema.europa.eu/ema/index.jsp?curl=pages/news\\_and\\_events/news/2014/07/news\\_detail\\_002136.jsp&mid=WC0b01ac058004d5c1](http://www.ema.europa.eu/ema/index.jsp?curl=pages/news_and_events/news/2014/07/news_detail_002136.jsp&mid=WC0b01ac058004d5c1)). Ferumoxytol is contraindicated in patients with a history of iron overload or known iron/dextran hypersensitivities (119). Ferumoxytol is available in individual vials that contain 17 mL of 510 mg of elemental iron in a sterile, pH-balanced solution. Currently, the FDA recommends that the agent be administered in a diluted fashion as an infusion over 15 min, rather than as an undiluted IV bolus (144).

### *Cerebrovascular Imaging with Ferumoxytol*

The vascularity of a lesion affects the behavior of contrast agents at the site. Two important factors governing exogenous contrast enhancement at a lesion site are 1) vascular integrity and 2) vascular density. The former dictates how easily the contrast agent can successfully extravasate into and around the lesion while the latter is related to

the amount of contrast that is likely to extravasate given that the vessels are pathologically leaky. Both vascular integrity and vascular density are extremely relevant in the context of CNS neoplasms, which are often characterized by higher vascularity that is abnormal, tortuous, and leaky (see Chapter I; *Neurovascular unit pathology in neoplastic disease*) (145). After IV infusion, contrast agents distribute throughout the peripheral and cerebral vasculature. The time during which contrast agents are localized exclusively intravascularly is known as their blood pool phase (Figure 2.6). Low molecular weight GBCA have a very short blood pool phase while larger molecular weight ferumoxytol nanoparticles have a long blood pool phase. As such, ferumoxytol-enhanced MRI scans are useful for visualizing the cerebrovasculature during the blood pool phase of the nanoparticle (146,147) (Figure 2.6b).

Perfusion is a physiological parameter that characterizes the delivery of blood to tissue (148). Perfusion imaging is useful for assessing lesion vascularization in intensely enhancing regions that could represent either active tumor or necrosis (149). Active tumor growth and necrosis can have similar enhancement effects on anatomical MRI, but can be differentiated using contrast-enhanced perfusion-imaging techniques. Two perfusion MRI techniques, dynamic-susceptibility contrast (DSC) perfusion imaging and steady-state (SS) perfusion imaging, are commonly used to assess brain vasculature and supplement anatomical MRI scans (Figure 2.7). Each technique can be used to calculate maps of relative cerebral blood volume (CBV; a metric used to locate actively growing tumor for biopsy targeting and to assess tumor progression, response, grading and prognosis) in a region of interest (149). DSC-MRI is a dynamic MRI technique that relies on monitoring of the “first-pass” of low molecular weight contrast through the

cerebrovasculature. The drawbacks of performing this technique with GBCAs relate to the short blood pool phase and rapid extravasation of these agents: 1) lesions with highly permeable (dysfunctional) cerebrovasculature will underestimate blood volumes as the CBV calculation assumes zero contrast extravasation (150) and 2) the rapid extravasation of GBCAs necessitates a rapid image acquisition in order to visualize GBCA in the blood pool (at least 3 min after infusion for a 0.1 mmol/kg body weight dose) (151), which comes at the expense of image resolution. Ferumoxytol was originally used to solve some of these issues with DSC-MRI. Because ferumoxytol has a prolonged blood pool phase relative to GBCA, it renders more reliable CBV measurements from DSC-MRI (152). Further, DSC-MRI with GBCA may require a contrast “preload” dose and post processing leakage correction that are not required with ferumoxytol (150,153). Ferumoxytol shows similar advantages in MR angiography, where it increases the spatial resolution and visualization of brain microvasculature compared to GBCAs with increased blood resident times (~30 min), such as Gadofosveset (119). However, even with ferumoxytol, low resolution still limits the DSC-MRI technique (149).

SS-MRI is an MRI technique that relies on the use of contrast with a long intravascular residence. The long blood pool phase ensures that the concentration of contrast in the cerebrovasculature is approximately constant and that there is limited vascular leakage throughout the imaging procedure (154). The SS technique was not previously used clinically due to lack of suitable blood pool imaging agent, but Varallyay *et al.* demonstrated in 2013 that long-circulating ferumoxytol enabled such imaging at clinically applicable doses, rendering high resolution, nearly-distortion free CBV maps

(149). This method is advantageous as it allows longer image acquisition times, which results in higher spatial resolution images (Figure 2.7).

### *CNS Inflammatory Imaging with Ferumoxytol*

Exogenous contrast agents are often employed to not only help visualize the lesion, but also to assess its vascularity, its malignancy, or its response to treatment. Both GBCAs and ferumoxytol require BBB dysfunction to enter the brain parenchyma and both improve border delineation of lesions relative to pre-contrast images. Unlike GBCAs, whose enhancement is immediate and relatively transient, with signal changes completely resolved within 60min, ferumoxytol can be used at delayed time points (24h) for macrophage imaging. Outside of the CNS, ferumoxytol extravasates into tissues of the mononuclear phagocyte system (MPS; liver, spleen, lymph nodes, and bone marrow) where it is taken up by resident, tissue-specific, phagocytic macrophages, enabling *in vivo* imaging of macrophages (155). As macrophages are known to accumulate around and inside inflammatory pathologies as part of an innate immune response, inflammation detection using ferumoxytol-enhanced MRI is a clinically relevant imaging endeavor (156,157).

MRI of inflammatory CNS lesions with ferumoxytol is an attractive avenue of study as ferumoxytol is uniquely situated to characterize not only CBV and vascular architecture, but also BBB dysfunction and lesion inflammatory state. Recall that, if a dysfunctional BBB is present, ferumoxytol will extravasate into the brain parenchyma in a delayed fashion as it slowly leaves the blood pool. Peak parenchymal ferumoxytol enhancement is usually seen at lesions ~24h after ferumoxytol administration (96). At 3T, signal changes can remain for days (96). In the brain parenchyma, ferumoxytol can be

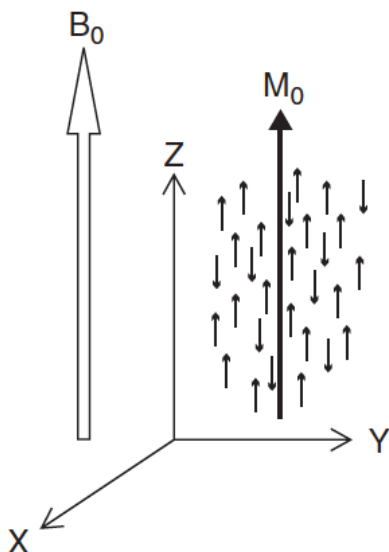
taken up by monocyte-derived macrophages that have also infiltrated due to BBB dysfunction, or by activated brain-resident microglia and phagocytic astrocytes (101). This uptake makes ferumoxytol a candidate for evaluation of macrophage-rich CNS lesions *in vivo* using MRI. Parenchymal ferumoxytol enhancement on MRI thus reflects two phenomena: the presence of vessel leakiness and ferumoxytol uptake into inflammatory phagocytes. Characterizing the behavior of ferumoxytol at cerebral vessels and neuroinflammatory lesion sites may aid in clinical interpretation of ferumoxytol-enhanced MRI in lesion-bearing patients. Research to date has suggested that, for lesion delineation purposes, delayed ferumoxytol imaging is not inferior to MRI with traditional GBCA; a 2011 study comparing the enhancement achieved with the two agents in patients with untreated gliomas found no significant differences in T<sub>1</sub>-weighted estimated enhancement sizes (158). Further, GBCA and ferumoxytol-enhanced MRI have been shown to detect an equal number of enhancing masses in primary brain tumors and metastatic lesions on MRI (159).

Due to the cell-specific uptake of ferumoxytol, the composition of a lesion's immune cell infiltrate will determine the extent to which it will enhance with ferumoxytol. White blood cells, T-cells, B-cells, and dendritic cells can all infiltrate neuroinflammatory lesions depending on the cytokine/chemokine milieu, but only macrophages/microglia and phagocytic astrocytes demonstrate ferumoxytol uptake and intracellular signal enhancement on MRI. Making use of this fact, a 2017 study from Stirrat *et al.* evaluating ferumoxytol enhancement in acute myocarditis determined that the inflammation in this condition was not macrophage-dependent based on a lack of ferumoxytol enhancement in the inflamed and edematous myocardial tissues (160). A

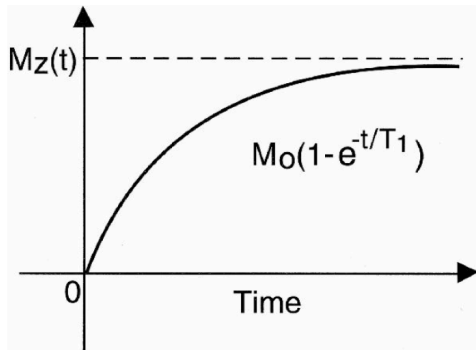
2015 study found that, due to its uptake in tumor associated macrophages (TAMs), ferumoxytol but not GBCA could delineate areas of early necrosis on MRI, even in tumors characterized by an overall lack of blood perfusion (161). Ferumoxytol TAM enhancement may act as a noninvasive diagnostic assay in patients with CNS neoplasms; in peripheral breast cancers the presence of TAMs is strongly correlated with poor outcomes in patients (156,162). Further, macrophage-rich areas of a lesion can be targeted for biopsy with ferumoxytol-enhanced imaging (158,163). Because inflammation is a predictive factor for rupture of cerebral aneurysms, ferumoxytol-enhanced MRI is also a candidate to evaluate aneurysm stability. In a 2012 pilot study, Hasan *et al.* demonstrated that delayed MRI (24h) with ferumoxytol could be used to predict cerebral aneurysm instability; ferumoxytol localization to macrophages in aneurysm walls strongly suggested probability of rupture within 6 months (164).

In summary, ferumoxytol is an attractive alternative contrast agent for patients with renal dysfunction who cannot receive GBCAs. Unlike GBCAs, ferumoxytol nanoparticles do not pose safety concerns for NSF or tissue deposition as they are treated as elemental iron after breakdown. Ferumoxytol also has greater relaxivity properties than GBCAs, which enables greater sensitivity during MRI (109). Ferumoxytol is not merely an alternative to GBCAs, however, as it possesses many unique and attractive imaging properties in its own right, including a prolonged vascular phase and intracellular imaging capabilities. Indeed, dual contrast with GBCAs and ferumoxytol will likely offer the most information for MRI, enabling *in vivo* visualization of CBV, BBB breakdown, cellular inflammation, and lesion development in both animal models and in clinical neurological disease.

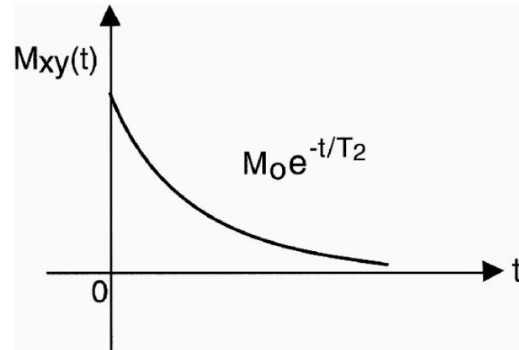
## Figures



**Figure 2.1.** Vector representation of net magnetization produced in the presence of an external magnetic field.  $^1\text{H}$  proton spins are represented as small arrows. In the presence of an external magnetic field ( $B_0$ ), these nuclei behave as bar magnets and will preferentially align themselves with the large  $B_0$ . The result is that the net magnetization ( $M_0$ ) points in the direction of  $B_0$ . Figure reproduced with permission from (103).

**A**

$$M_z(t) = M_0(1 - e^{-t/T_1})$$

**B**

$$M_{xy}(t) = M_0 e^{-t/T_2}$$

**Figure 2.2.** Time course of tissue magnetization is governed by the  $T_1$  and  $T_2$  relaxation constants. After the RF pulse is turned off, tissue protons will return to their lowest energy state and align themselves with the large  $B_0$ . During this process, **A**) longitudinal magnetization along  $M_z$  is recovered and **B**) transverse magnetization along  $M_{xy}$  decays. Both processes occur simultaneously with rate constants of  $1/T_1$  and  $1/T_2$ , respectively. Figure adapted with permission from (102).

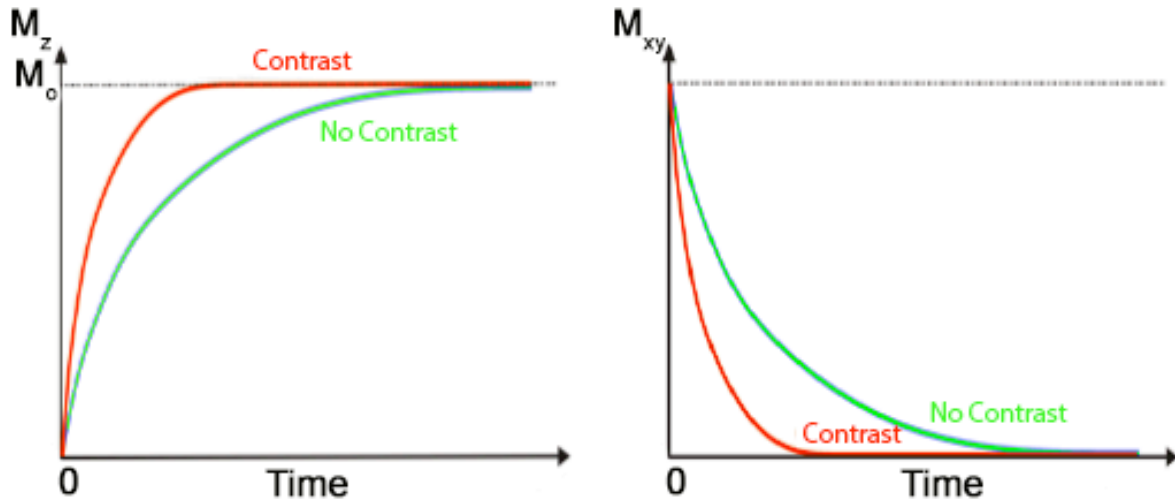


**Figure 2.3.** Magnetic resonance imaging contrast agents shorten  $T_1$  and  $T_2$  relaxation times. The time course of longitudinal magnetization recovery (**A**) and transverse magnetization decay (**B**) is shown in the presence (orange) and absence (green) of a contrast agent.

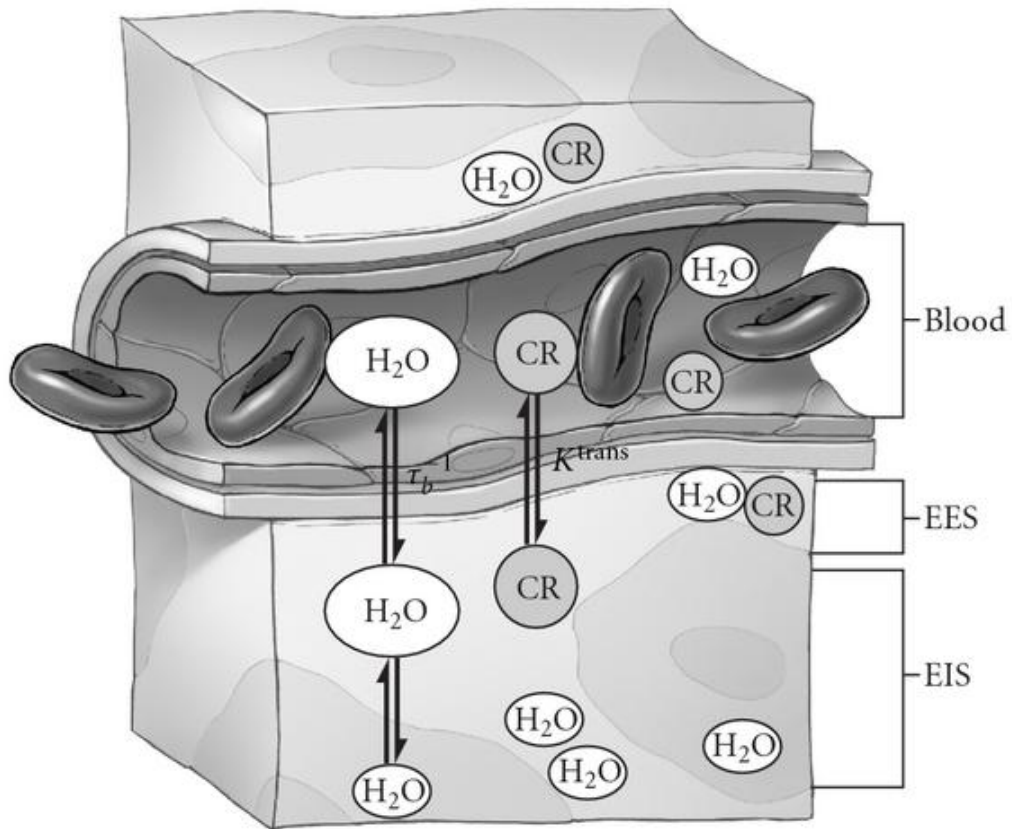


**Figure 2.4.** Gadolinium-based contrast reagent extravasation in a three-compartment tissue model. After intravenous injection, the gadolinium-based contrast reagent (CR) distributes throughout the blood plasma. These agents rapidly equilibrate with the extravascular extracellular space (EES) at a volume transfer constant defined by the metric  $K^{trans}$ , but only if the cerebrovascular blood-brain barrier is disrupted. This CR is not taken up into cells and does not occupy the extravascular intracellular space (EIS). Contemporaneously, water exchange occurs throughout all 3 tissue compartments. Figure reproduced with permission from (110).

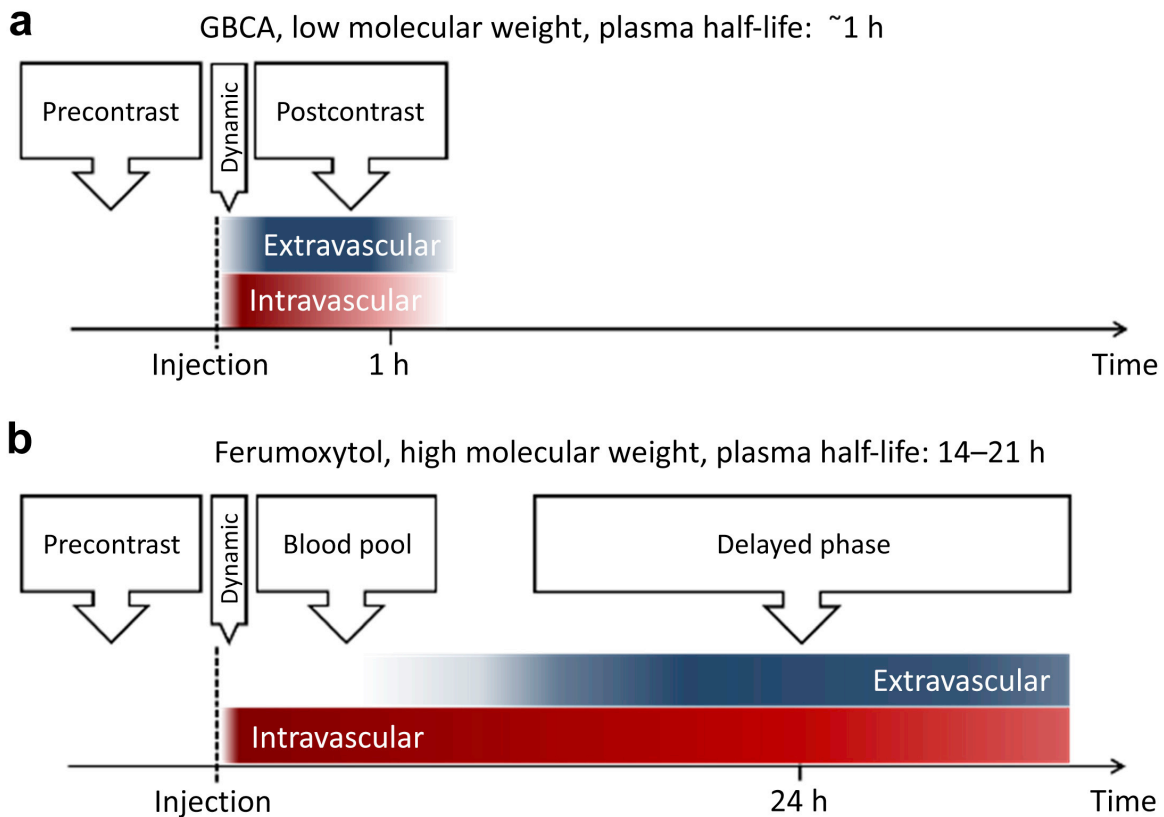


**Figure 2.5.** Vascular localization of gadolinium-based contrast agents and ferumoxytol after injection. **a)** Low molecular weight gadolinium-based contrast agents (GBCAs) have a short plasma half-life of ~1h and quickly extravasate into the extracellular space after injection. Consequently, there is temporal overlap of vascular and parenchymal enhancement on magnetic resonance imaging. **b)** Ferumoxytol has a long plasma half-life of 14-21h and does not extravasate immediately after injection. Consequently, ferumoxytol has a distinct blood pool phase that allows for high resolution imaging of the intravascular space and a delayed tissue uptake phase that allows for tissue imaging ~24h after administration. Figure reproduced from (119).

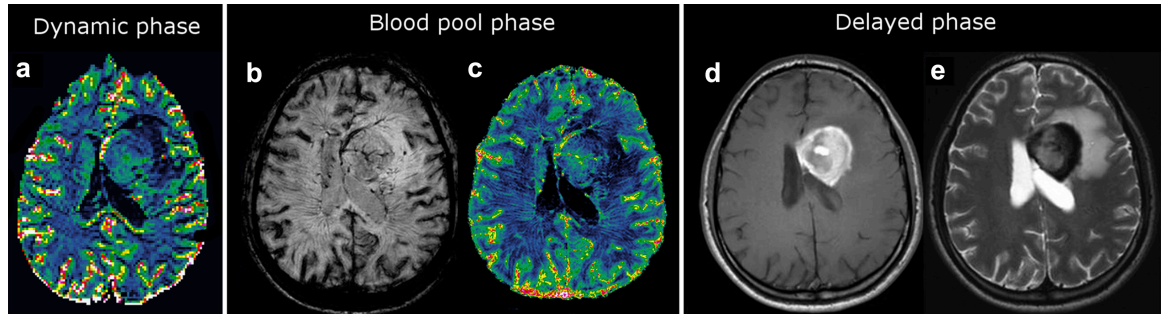


**Figure 2.6.** Imaging phases of ferumoxytol after intravenous administration in a single tumor-bearing patient. **a)** Immediately after injection, ferumoxytol can be used for dynamic first pass perfusion imaging to create relative cerebral blood volume (rCBV) maps that allow assessment of hypo- and hypervascular areas within or around a brain lesion. **b)** With an intravascular half-life of 14-21h, ferumoxytol has a long blood pool phase where it can be used in susceptibility-weighted MRI to assess cerebrovascular architecture, **c)** which can then be compared with the CBV maps. Over ~24h ferumoxytol leaks across abnormal BBB, leaves the blood pool, and enters the parenchyma, allowing delayed **d)**  $T_1$ - and **e)**  $T_2$ -weighted MRI to be performed. Note that fluid surrounding the lesion is visible in **d)** as hypointense signal and in **e)** as hyperintense signal. Figure reproduced from (119).

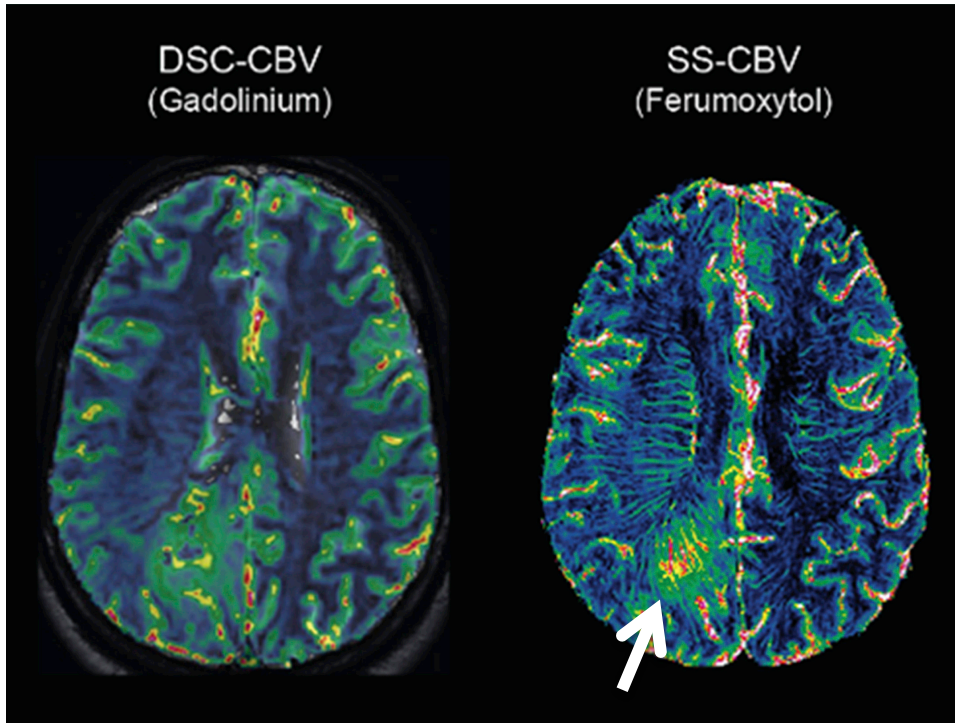


**Figure 2.7.** Spatial resolution comparison of cerebral blood volume maps calculated from gadolinium-enhanced dynamic susceptibility contrast imaging versus ferumoxytol-enhanced steady-state imaging. Relative cerebral blood volume (rCBV) maps calculated using two different imaging techniques with either gadolinium-based contrast agent (Gadolinium) or ferumoxytol in tumor-bearing patient. Left: Low-molecular weight gadolinium contrast necessitates the use of a dynamic, first pass dynamic susceptibility contrast (DSC) imaging technique to calculate CBV maps. The spatial resolution of these maps suffers from the rapid image acquisition technique. Right: Use of the blood pooling agent ferumoxytol allows steady-state imaging to be performed with longer image acquisition, resulting in CBV maps with higher spatial resolution. Note that the area of increased blood volume within the tumor in the right occipital hemisphere is demonstrated more clearly in the right image (white arrow). Figure reproduced from (119).

### **Chapter 3. Ferumoxytol nanoparticle uptake in brain during acute neuroinflammation is cell-specific**

Heather L. McConnell<sup>a</sup>, Daniel L. Schwartz<sup>b</sup>, Brian E. Richardson<sup>c</sup>, Randall L. Woltjer<sup>d</sup>,  
Leslie L. Muldoon<sup>a</sup>, Edward A. Neuwelt<sup>a,e,f</sup>

<sup>a</sup>Department of Neurology, Oregon Health & Science University, Portland, OR, USA

<sup>b</sup>Advanced Imaging Research Center, Oregon Health & Science University, Portland,  
OR, USA

<sup>c</sup>Department of Molecular and Medical Genetics, Oregon Health & Science University,  
Portland, OR, USA

<sup>d</sup>Department of Pathology, Oregon Health & Science University, Portland, OR, USA

<sup>e</sup>Department of Neurosurgery, Oregon Health & Science University, Portland, OR, USA

<sup>f</sup>Department of Veterans Affairs, Portland Veterans Affairs Medical Center, Portland,  
OR, USA

*Published in Nanomedicine, August 2016*

*(DOI: 10.1016/j.nano.2016.03.009)*

### 3.1 Abstract

Ferumoxytol ultrasmall superparamagnetic iron oxide nanoparticles can enhance contrast between neuroinflamed and normal-appearing brain tissue when used as a contrast agent for high-sensitivity MRI. Here we used an anti-dextran antibody (Dx1) that binds the nanoparticle's carboxymethyl-dextran coating to differentiate ferumoxytol from endogenous iron and localize it unequivocally in brain tissue. Intravenous injection of ferumoxytol into immune-competent rats that harbored human tumor xenograft-induced inflammatory brain lesions resulted in heterogeneous and lesion-specific signal enhancement on MRI scans *in vivo*. We used Dx1 immunolocalization and electron microscopy to identify ferumoxytol in affected tissue post-MRI. We found that ferumoxytol nanoparticles were taken up by astrocyte endfeet surrounding cerebral vessels, astrocyte processes, and CD163<sup>+</sup>/CD68<sup>+</sup> macrophages, but not by tumor cells. These results provide a biological basis for the delayed imaging changes seen with ferumoxytol and indicate that ferumoxytol-MRI can be used to assess the inflammatory component of brain lesions in the clinic.

### Keywords

Neuroinflammation, MRI, Iron oxide nanoparticles, macrophages, contrast agents

---

**Abbreviations** CNS (central nervous system), MRI (magnetic resonance imaging), USPIO (ultrasmall superparamagnetic iron oxide), BBB (blood-brain barrier)

### 3.2 Introduction

Neuroinflammation is common in CNS pathologies and causes changes in the cerebrovasculature and brain parenchyma that can be inconsistent and subtle, complicating detection of inflammatory processes with magnetic resonance imaging (MRI). Because neuroinflammation results in tissue changes that occur before loss of function, *in vivo* imaging of inflammation is of significant clinical interest. Such imaging is enabled by ferumoxytol, a viral-sized (17-31 nm) USPIO nanoparticle (100,165). Ferumoxytol is approved by the Federal Drug Administration for treatment of iron deficiency anemia in patients with chronic kidney disease, but can be used off-label as a MRI contrast agent to detect CNS lesions and vascular abnormalities in brain (100,166,167). While conventional gadolinium-based contrast agents allow rapid, transient, non-specific imaging of BBB permeability, they cannot differentiate neuroinflammation due to trauma from that due to tumor, for example (168). The USPIO nanoparticle ferumoxytol is an emerging alternative approach for contrast enhancement in neuroimaging because, during neuroinflammation, it traffics from systemic circulation to reactive lesions and increases the contrast between affected and normal tissues (165). Ongoing phase II clinical trials using ferumoxytol in patients with high-grade gliomas and multiple sclerosis plaques show that ferumoxytol-contrasted MRI may resolve phenomena including vascular changes, altered BBB permeability, long-term tissue changes in tumors, brain parenchyma, and neurological lesions on MRI (clinicaltrials.gov NCT00660543) (100,169,170). Despite these clinical advances, the timing and mechanisms of ferumoxytol trafficking into the brain, uptake into neuroinflammatory lesions, and cell-type specificity are unknown. The lack of information on ferumoxytol localization is due in part to a lack of specific immunohistochemical markers. Perls'

Prussian blue staining is the method typically used to assess the *ex vivo* tissue distribution of ferumoxytol along with electron microscopy methods (171,172). However, Perls' stain is an imperfect method to measure ferumoxytol localization because of its relatively low sensitivity and because it cannot reliably distinguish between the nanoparticle and endogenous (e.g. hemorrhage-derived) iron deposits. Here, we demonstrate that an anti-dextran monoclonal antibody (Dx1) reproducibly and specifically associates with the modified dextran coating of the ferumoxytol nanoparticle, allowing us to localize it in tissues *ex vivo* and differentiate ferumoxytol from endogenous iron.

We hypothesized that the enhanced BBB permeability resulting from acute neuroinflammation would allow targeted delivery of ferumoxytol nanoparticles to inflammatory lesions. To that end, we developed and characterized a model of localized inflammatory lesion using intracerebral injection of immunogenic human tumor cells in immune-competent rats. Our results show that ferumoxytol nanoparticles traffic from system circulation to reactive lesions during neuroinflammation, are taken up in a cell-specific manner, and can be detected over time using non-invasive MRI techniques. We present a novel correlate of neuroinflammation that can improve diagnostic imaging and response characterization across numerous neuropathologies.

### 3.3 Methods

**Cell Culture and Reagents:** H460 non-small cell lung carcinoma cells were purchased from American Type Culture Collection (Manassas VA), used at a passage number below 20, and cultured in RPMI 1640 growth medium (Corning Life Sciences—Mediatech, Manassas VA USA) with 1% Penicillin/Streptomycin, 0.1% Gentamicin (Life Technologies, Eugene OR USA), and 10% FBS in 5% CO<sub>2</sub> at 37°C. U87 glioma cells were purchased from American Type Culture Collection (Manassas VA USA), used at a passage number below 20, and cultured in EMEM growth medium (Corning Life Sciences—Mediatech, Manassas VA USA) with 1% Penicillin/Streptomycin (Life Technologies, Eugene OR USA), 0.1% Gentamicin (Life Technologies, Eugene OR USA), and 10% FBS in 5% CO<sub>2</sub> at 37°C. Ferumoxytol (Feraheme®) was obtained from AMAG Pharmaceuticals Inc., Cambridge, MA USA.

**Neuroinflammation Model:** The care and use of animals was approved by the Institutional Animal Care and Use Committee and was supervised by the OHSU Department of Comparative Medicine. Adult female, immune-competent heterozygous nude rats (rnu/+) (200-300 g) were anesthetized with IP ketamine (60 mg/kg) and diazepam (7.5 mg/kg). To induce neuroinflammation, 10  $\mu$ L of either H460 human non-small cell lung carcinoma cells (10<sup>6</sup> cells/ $\mu$ L, >90% viability) (n=6) or U87 glioma cells (n=3) were injected into the right caudate nucleus (bregma= 0; lateral 0.31 cm; vertical -0.65 cm) of each rat at a rate of 1  $\mu$ L/min. To control for any inflammation due to the inoculation procedure, 10  $\mu$ L of 0.9% NaCl was injected into the contralateral caudate nucleus (bregma= 0; lateral -0.31 cm; vertical -0.65 cm) of each rat using a stereotactic frame.

**Intravenous Ferumoxytol Administration:** Rats were anesthetized with 2% mask isoflurane with oxygen. Ferumoxytol (30 mg/mL) (50 mg/kg body weight) was delivered over 60 seconds using a 24-gauge IV catheter in the lateral tail vein. For the pilot MRI study, ferumoxytol was administered at 0 (n=2), 24 (n=7), or 48 (n=2) hours after the inflammatory insult. Control animals instead received an equivalent volume of 0.9% NaCl IV (n=2).

**Magnetic Resonance Imaging:** MRI was performed 24h after ferumoxytol administration using a horizontal bore 11.75 T (Bruker Scientific Instruments, Billerica MA) under IP dexmedetomidine (0.6 mg/kg) (Zoetis, Lincoln NE) and ketamine (15 mg/kg) (sedation).  $T_1$ -weighted images were acquired with a fast low angle shot gradient-echo sequence (repetition time [TR]/echo time [TE]= 160.0 ms/1.6 ms, flip angle =  $25^\circ$ , 25 slices, inplane field of view (FOV) = 32 x 32 mm, matrix = 256 x 256, number of averages = 4, total acquisition time = 2.75 min).  $T_2$ -weighted images were acquired with a Rapid Acquisition and Refocused Echoes (RARE) spin-echo sequence (TR/TE = 4020.6 ms/11.8 ms, RARE factor = 8, 25 slices, FOV = 32 x 32 mm, matrix = 256 x 256, number of averages = 1, total acquisition time = 2.13 min). Images were processed using AFNI (173). Briefly, images were compiled to NIFTI format, corrected for  $B_1$  inhomogeneity using 3dUnifize, with manual thresholding and clustering performed to isolate the contrast-enhanced region-of-interest (ROI) on the  $T_1$ -weighted image. The ROI was then inverted along the midsagittal axis (3dLRflip) in order to extract image values in the NaCl-inoculated hemisphere (3dmaskave). The ROI was then superimposed

on T<sub>2</sub>-weighted images, and the same value-extraction process was performed. As the animals were fully anesthetized for the entire MRI session, no between-scan coregistration was necessary.

**Immunohistochemistry:** Immediately after MRI, rats were euthanized with a lethal dose of IV euthasol (Virbac, Fort Worth TX). Whole brains were removed for processing, fixed in 4% paraformaldehyde (Tousimis, Bethesda MD) at room temperature for 48 h and processed into paraffin blocks. Paraffin-embedded, 7- $\mu$ m-thick tissue sections were cut from control and experimental rat brain hemispheres and mounted onto charged microscope slides. Immunohistochemical stains were applied to sections after deparaffinization and antigen retrieval (5 minutes at room temperature in 95% formic acid followed by 30 minutes incubation in citrate buffer, pH 6.0, at 80°C). Tissue sections were blocked with 3% nonfat dry milk in phosphate-buffered saline and stained with antibodies to the macrophage markers CD68 (AbCam, Cambridge MA, catalog #AB125212) (1:200) or CD163 (Biorad ABDSerotec Inc., Raleigh NC, catalog #MCA342R) (1:2500), the astrocyte marker glial fibrillary acidic protein (GFAP) (Sigma-Aldrich, St. Louis MO, catalog #G9269) (1:2500), or dextran (Dx1) (Stemcell Technologies, Vancouver Canada, catalog #60026) (1:100). Results were visualized after application of appropriate secondary antibodies using diaminobenzidine or Vector Red (Vector Laboratories, Burlingame, CA) as chromagens using an Olympus Bx50 microscope.

**Immunofluorescent Histochemistry:** Seven- $\mu$ m-thick paraffin-embedded tissue sections of formalin-fixed control and experimental rat brain hemispheres were mounted onto charged microscope slides, deparaffinized, subjected to antigen retrieval as described above, blocked with 10% BSA, and simultaneously incubated with antibodies against D $\alpha$ 1 and either  $\alpha$ -smooth muscle actin (SMA) (AbCam, Cambridge MA, catalog #AB5694) (1:2500) (a vascular smooth muscle cell marker) or CD68 (AbCam, Cambridge MA, catalog # AB125212) (1:200), all diluted in 1% BSA. Antibody labeling was visualized using Alexa-conjugated fluorescent secondary antibodies (1:500, Life Technologies, Grand Island, NY.) Sections were treated with Autofluorescence Eliminator Reagent (Millipore, Billerica, MA) and mounted using Prolong Gold antifade agent with DAPI (Life Technologies). Tissue was imaged using a Zeiss LSM 780 confocal microscope (Carl Zeiss, Oberkochen, Germany) at the OHSU Advanced Light Microscopy core facility. Post-acquisition processing was performed using ImageJ software (NIH, Bethesda MD).

**Human subjects:** Tissue collection analysis was performed at Oregon Health & Science University with informed consent by subjects and in accordance with the requirements of the local Institutional Review Board. For the histological review and immunohistochemical studies, the pathologic diagnoses of glioblastoma were established by a neuropathologist and reviewed (by RLW) to confirm the diagnosis and assess tumor vasculature. Immunohistochemical evaluation was performed on archival tissue from 2 subjects. Immunohistochemical staining was performed as described above.

**Tissue sampling:** For rat tissue, dextran immunostaining was consistently distributed throughout the macrophage-rich core of the lesion and a representative area was depicted in the figures. Human tumor tissue was derived from the MRI T<sub>1</sub>- enhancing portion of a glioblastoma and Dx1 immunostaining was present multifocally throughout the area of the tumor and was present most conspicuously around vessels supplying viable tumor.

**Electron Microscopy:** Tissues from the neuroinflamed and saline-inoculated caudate nuclei of rats (n=2) were collected 24h after ferumoxytol administration and fixed in 1.5% glutaraldehyde, 1.5% paraformaldehyde in 0.1 mol/L sodium cacodylate buffer (pH 7.4). The tissues were then postfixated in buffered osmium tetroxide, stained *en bloc* with 1% uranyl acetate, dehydrated in graded ethanol solutions, and then embedded in epoxy resin. Sections of 60–90 nm thicknesses were placed onto 200 mesh grids, stained with uranyl acetate and lead citrate, then examined with a Techni 12 electron microscope (FEI, Hillsboro OR) at 80 Kv. Digital images were acquired using a 16 megapixel Advanced Microscopy Techniques camera (AMT, Woburn MA). Nanoparticle diameter was measured using the scope measurement tool, which is calibrated against a diffraction grating replica. Post-acquisition processing and additional nanoparticle diameter measurements (figure insets) were performed using ImageJ software.

### 3.4 Results

#### **Pilot characterization of the tumor xenograft neuroinflammation model**

We performed a pilot study investigating magnetic resonance (MR) signal changes at intracerebral lesion sites in order to characterize the time course of inflammatory changes induced by tumor xenograft placement. We acquired  $T_1$ - and  $T_2$ -weighted MRI experiments at 11.75 T 24, 48, and 72h after insult. Ferumoxytol was administered 24h prior to each scanning session. We found that peak susceptibility and peak enhancement occurred 48h post-insult on  $T_2$ -weighted and  $T_1$ -weighted images, respectively (Figure 3.1F). Therefore, the 48h time point was used for all subsequent experiments (Figure 3.2). Ferumoxytol resulted in MR signal changes at all reactive inflammatory lesions.  $T_1$ -weighted sequences produced areas of hypointensity within the core of the lesion (due to  $T_2$  contributions from areas of high contrast agent concentration) and a peripheral hyperintense ring around the lesion (Figure 3.1A).  $T_2$ -weighted experiments showed a marked focal signal loss at the insult site due to high concentrations of ferumoxytol (Figure 3.1D). Color maps depicting the values within each ROI for both  $T_1$ - and  $T_2$ -weighted images are shown in Figures 3.1B and 3.1E, respectively. Saline injection into the contralateral hemisphere did not result in MRI signal changes (Figure 3.1A, white arrowhead). The ratio of MRI values (lesion/saline) averaged over each ROI for 24, 48, and 72h measurements were 1.23, 1.41, and 1.19 for  $T_1$ -weighted images and 0.72, 0.53, and 0.94 for  $T_2$ -weighted, respectively.

### **Ferumoxylol traffics from systemic circulation to reactive lesions**

Because MRI signal enhancement occurred in xenografted but not saline-injected hemispheres (Figure 3.1A), we determined whether these signal changes were due to ferumoxylol extravasation and parenchymal infiltration in the affected hemisphere. Immunohistochemical analyses of the inflamed hemisphere containing the xenograft demonstrated CD68- and CD163-rich lesions with live tumor cells located peripherally (Figure 3.3B and 3.3C). We used a monoclonal anti-Dx1 antibody to detect the ferumoxylol nanoparticle coating and observed strong intracellular staining in areas that colocalized with the CD68<sup>+</sup> and CD163<sup>+</sup> cells at the lesion (Figure 3.3A). The contralateral (saline-injected) hemispheres were lesion-negative and showed no CD163 or Dx1 reactivity after IV ferumoxylol (data not shown). Rats that received IV saline after xenograft placement instead of IV ferumoxylol had similar CD163<sup>+</sup>-rich lesions (Figure 3.3F) but showed no Dx1 reactivity (Figure 3.3E).

In addition to the intracellular Dx1 staining within the lesion, we observed Dx1 staining in cells outside the lesion that were macrophage-negative (Figure 3.3A arrowhead). Astrocytes are known to be capable phagocytes following activation; we analyzed CD163/CD68-negative, Dx1-positive regions for GFAP-reactivity and found robustly staining cells of astrocytic morphology (Figure 3.3D arrowhead).

### **Ferumoxylol uptake at inflammatory lesions is cell type-specific**

We confirmed cell-specific uptake of ferumoxylol using double immunofluorescence labeling. Immunostaining for Dx1 and CD68 confirmed that ferumoxylol was intracellularly localized to CD68<sup>+</sup> cells in the lesions (Figure 3.4A). In these cells we

noted membrane-localization of CD68 and diffuse, cytoplasmic Dx1 localization with distinct nuclear exclusion. Control rats that received saline instead of ferumoxytol showed similar CD68<sup>+</sup> cells at the lesion but did not display Dx1 reactivity (Figure 3.4B). We next identified nearby vasculature as the source of ferumoxytol using multichannel high-resolution confocal microscopy. Within a z-stack of optical sections, dual staining for Dx1 and SMA revealed abundant perivascular ferumoxytol and sparse, residual ferumoxytol within the vascular lumen of precapillary arterioles (Figure 3.4C). The confinement of Dx1 staining around the vasculature suggested that some of the nanoparticles might become trapped within the basal lamina basement membrane of the neurovascular unit and be unable to extravasate, a phenomenon known to occur with iron nanoparticles that are >30 nm in diameter (174). We repeated the dual staining for Dx1 and SMA on biopsy tissue from a human patient with glioblastoma who received IV ferumoxytol prior to MRI and gross tumor resection and observed the same perivascular delimitation of Dx1 staining around cerebral vessels (Figure 3.4D).

To identify the cellular or subcellular perivascular structure in which ferumoxytol accumulates, we performed electron microscopy on tissue from inflamed and control rat brain hemispheres. Twenty-four h after administration, ferumoxytol nanoparticles were found in dilated astroglial endfeet-ensheathing capillaries (Figure 3.5A) and were identified as electron-dense particles ~30 nm in diameter (Figure 3.5A inset). Swollen astrocyte endfeet are an ultrastructural feature that has been noted previously in ischemic rodent brain (175). Astroglial processes in the parenchyma also showed abundant ferumoxytol uptake (Figure 3.5B). Finally, we confirmed intracellular ferumoxytol localization within lysosome-rich CNS macrophages (Figure 3.5C). In agreement with

our immunohistochemical findings that showed more robust Dx1 staining in macrophages than in areas of gliosis (Figure 3.4A, macrophages versus arrowhead), ferumoxytol nanoparticles were more abundant in macrophages and more aggregated in appearance (Figure 3.5C) than in astrocytic endfeet (Figure 3.5A) or processes (Figure 3.5B). The saline-inoculated hemispheres of rats that received IV ferumoxytol were ferumoxytol-negative and did not display swollen astrocytic endfeet (Figure 3.5D).

### **3.5 Discussion**

An important barrier to the use of ferumoxytol in the clinic is that the timing and pattern of delayed parenchymal MRI signal enhancement can be highly variable, which confounds meaningful interpretation of MRI data (166,176). These inconsistencies led us to believe that the localization of the nanoparticles during and after their extravasation may underlie the variable timing and pattern of parenchymal MRI enhancement. In the current study, we evaluated ferumoxytol imaging characteristics and entry into the brain using a human tumor xenograft model of acute neuroinflammation in rat. We found that ferumoxytol USPIO nanoparticles extravasate from the cerebrovasculature and traffic to reactive CNS lesions within 24h of their entry into the systemic circulation, but only if neuroinflammation is present. Our finding that ferumoxytol extravasation into the brain parenchyma only occurred in hemispheres containing inflammatory lesions indicates an inflammation-dependent increase in cerebrovascular permeability and supports the well-characterized role of the cerebrovascular BBB in bridging peripheral and central innate immune responses (157). Our results demonstrated cell-specific uptake of ferumoxytol by astrocyte endfeet surrounding cerebral vessels, astrocyte processes, and CD163<sup>+</sup>/CD68<sup>+</sup>

macrophages in the brain. In addition, we found that our model of neuroinflammation was clinically relevant, as it recapitulated features of ferumoxytol uptake and localization in the vasculature of GBM patients.

The mechanism by which ferumoxytol extravasates from cerebral vasculature remains unclear, but may involve 1) passive diffusion of free, non-cell associated nanoparticles across a disrupted BBB (118,177) or 2) active transport across the BBB within infiltrating monocytes (177,178). Our electron microscopy data is most consistent with a mechanism involving free nanoparticle trafficking, as free nanoparticles were observed in astrocyte endfeet and processes that ensheath brain vascular ECs and, as such, should be the first cells to encounter extravasating nanoparticles (177,179). Consistent with reports showing *in vitro* iron oxide nanoparticle uptake by astrocytes (180-182), we found ferumoxytol within swollen astrocytic endfeet 24h after its administration. Interestingly, ferumoxytol was only present in endfeet that did not juxtapose EC nuclei, suggesting that the nanoparticles do not cross EC nuclei though such permeability has been reported previously for *in vitro* systems (183,184). Extravasation of nanoparticles across disrupted EC TJs is also plausible, but we were unable to resolve such structures in our images.

An alternative mechanism for ferumoxytol extravasation from the cerebrovasculature may involve Trojan horse-like transport across the BBB within infiltrating monocytes (178). This mechanism was not supported by our histological or electron microscopy data, but only insofar as our tissue sections did not capture an extravasation event. Previous studies investigating the ability of USPIO (~20-30 nm particle diameter) and larger SPIO (~60-150 nm particle diameter) nanoparticles to label

leukocytes *in vivo* for MRI cell tracking found that only larger SPIO nanoparticles were appreciably taken up by mononuclear leukocytes (185,186). Differential cellular uptake of USPIO nanoparticles can depend on many variables, including particle coating composition, particle charge, and particle size. In 2012, Thu *et al.* demonstrated that effective *in vitro* labeling of mononuclear leukocytes with ferumoxytol could only occur in the absence of serum and only if the USPIO nanoparticle was first complexed with heparin and protamine (effectively increasing the size of the nanoparticle and strength of the stimulus for cell uptake) (172). The rare systemic uptake of ferumoxytol reported and our histological and electron microscopy data both support a mechanism wherein ferumoxytol traffics into the CNS as a free nanoparticle. Importantly, our data does not rule out the possibility that, once inside the brain, free ferumoxytol is taken up by infiltrating blood monocytes that differentiate into macrophages upon CNS entry. Indeed, the vast numbers of CD163+/CD68+ macrophages observed at the reactive lesion sites suggest such a scenario.

The USPIO nanoparticle ferumoxytol is of particular clinical interest for detecting tissue changes in the brain because, during neuroinflammation, it traffics from systemic circulation to reactive lesions and can be detected by MRI. Differential cellular uptake of this USPIO nanoparticle suggests the potential for improved diagnostic discrimination of inflammatory and vascular etiologies of brain lesions. Importantly, improved imaging of pathologies that directly alter the permeability of the BBB or induce inflammation may be a critical step in improving patient management. Previous studies have demonstrated that MRI with ferumoxytol facilitates visualization of inflammatory cells within and around inflammatory CNS lesions such as stroke (187), vascular malformations (166),

demyelination, and brain tumors (100,169). Immediately after injection, ferumoxytol is visible on  $T_1$ -weighted MRI as signal enhancement in the vasculature. In normal brain, ferumoxytol does not extravasate appreciably from the cerebral vasculature (96). During neuroinflammation, however, organized immunological cascades develop within the NVU and CNS that can increase vascular permeability (188-190). When an inflammatory CNS lesion is present, ferumoxytol is taken up by inflammatory macrophages and demonstrates delayed extravascular enhancement that peaks 24h after its administration.

Our histological identification of ferumoxytol nanoparticles in tissue via Dx1 immunohistochemistry provides new insight into disease pathogenesis in affected tissues. The opposing ring enhancement patterns found on  $T_1$  and  $T_2$ -weighted MRI reflect our immunohistochemistry findings that clearly show ferumoxytol uptake in densely packed macrophages in the core of the lesion and reactive astrocytes around the margin of the lesion but not in viable tumor cells. The non-invasive, *in vivo* identification of immune reactivity to inflammatory CNS insult at sub-millimeter resolution using ferumoxytol-MRI may provide a more expansive view of affected tissue and provide more accurate targets for invasive biopsy in CNS lesions than current standard of care contrast-enhanced MRI. The nonlinearity of  $T_1$ -weighted contrast with respect to ferumoxytol concentration provides further specificity of microenvironmental heterogeneity in and around a lesion. Strong  $T_1$ -weighted signal dropout in regions of intense Dx1 staining within macrophages suggests a  $T_2$  shortening contribution to  $T_1$ -weighted images in regions with very high ferumoxytol concentration. We observed  $T_1$  hyperintensity among areas of diffuse Dx1 staining on the lesion periphery that suggested lower ferumoxytol concentrations, possibly due to nanoparticles localized within the processes or endfeet of

reactive astrocytes. These findings suggest that ferumoxytol-MRI may be able to differentiate immunological microenvironments in the brain.

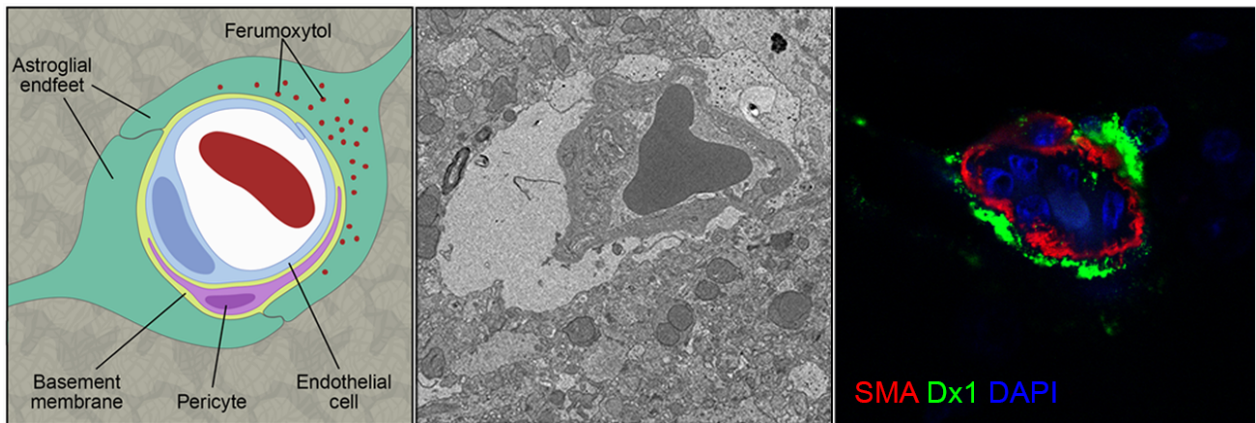
Limitations of our study include a relatively high dose of administered ferumoxytol (compared to human dosages; although, as seen in Figure 3.4D, we were able to detect ferumoxytol in human tissue) and an experimental model that relies on the acute inflammatory effects of a xenograft in rat that may not accurately replicate what occurs over time in human metastatic or primary CNS tumors. Furthermore, we used immune-competent rats in this study, but patients with brain tumors often display a degree of immunologic anergy; our use of a fully immune-competent animal may not adequately recapitulate the state of these patients. Future work may investigate the validity of our findings using hematogenous metastasis or spontaneous GBM models of inflammation.

In conclusion, our study is the first confirmation that ferumoxytol nanoparticles are taken up by astrocyte endfeet surrounding cerebral vessels, astrocyte processes, and CD163<sup>+</sup>/CD68<sup>+</sup> macrophages in a model of a brain inflammatory lesion. We identify a novel and specific marker of the ferumoxytol carboxymethyl-dextran coating, Dx1, which allows ferumoxytol to be unambiguously identified in tissue and differentiated from endogenous iron. We present a clinically relevant animal model of acute neuroinflammation with which to study ferumoxytol nanoparticle extravasation that recapitulates features of ferumoxytol localization in the vasculature of GBM patients. Moreover, we demonstrate that areas of Dx1 reactivity in CNS tissue match well with areas of signal change on MR images. Future investigations should quantify and correlate immune-based USPIO nanoparticle uptake and CNS infiltration with USPIO-induced

MR signal alterations, which we believe will assist interpretation of MR images in the clinical setting, guide CNS biopsy, and provide unique information to facilitate diagnostic specificity.

### **Acknowledgements**

We thank Josh Robertson, Megan Chalupsky, and Thao Pham for technical assistance with this study and Lori Vaskalis for help with figures.



**Graphical Abstract.** An ultrasmall superparamagnetic iron oxide nanoparticle (ferumoxytol) is used off-label as a contrast agent for magnetic resonance imaging of neuroinflammation in an immune-competent rat model. Dx1 (an anti-dextran monoclonal antibody) interacts with the modified carbohydrate coating of ferumoxytol, facilitating localization of the nanoparticles after extravasation from brain vasculature and phagocytosis by astrocytes and macrophages. The model is clinically relevant and recapitulated features of ferumoxytol localization in human glioblastoma multiform biopsy tissues.

## Figures

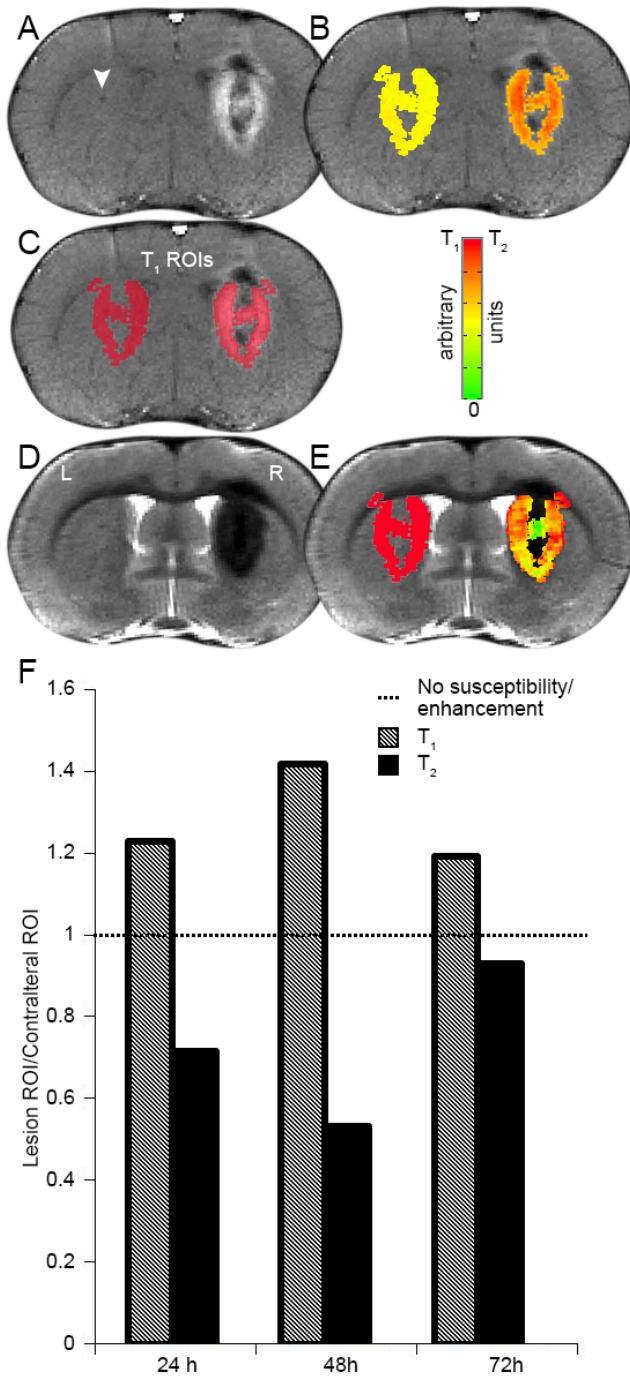


**Figure 3.1. Maximum ferumoxytol MRI susceptibility/enhancement occurs 48 h post inflammatory insult. (A, D) T<sub>1</sub> and T<sub>2</sub>-weighted MR images showing tumor cell and saline inoculation sites (right and left hemispheres, respectively) 48 h post-inoculation**

and 24h post-ferumoxytol. **(B, E)**  $T_1$  and  $T_2$  intensity values displayed as a color map in arbitrary units within the region of interest (ROI). **(C)** ROI masks superimposed on the  $T_1$ -weighted image. **(F)** Voxel values within the lesion and contralateral ROIs were averaged over all voxels and compared graphically as a ratio for both  $T_1$  (shaded)- and  $T_2$  (black)-weighted MR images at each post-inoculation time point.

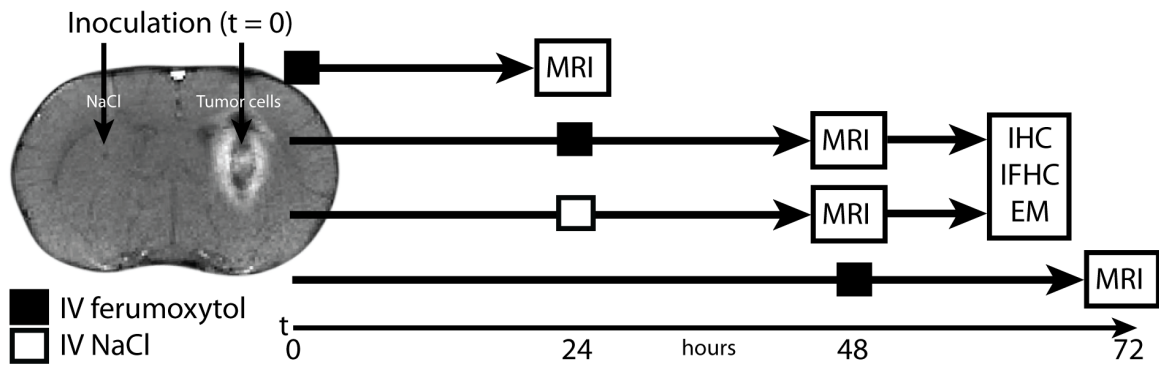


**Figure 3.2. Experimental protocol schematic.** For all experiments after the pilot MRI study, neuroinflammatory insult was administered at time ( $t$ )=0, IV ferumoxytol or saline (control) was administered at  $t=24$ h, and MRI was performed at  $t=48$ h. Immediately after MRI brains were extracted for immunohistochemistry (IHC) analysis, immunofluorescent histochemistry (IFHC) analysis, and electron microscopy (EM) analysis.

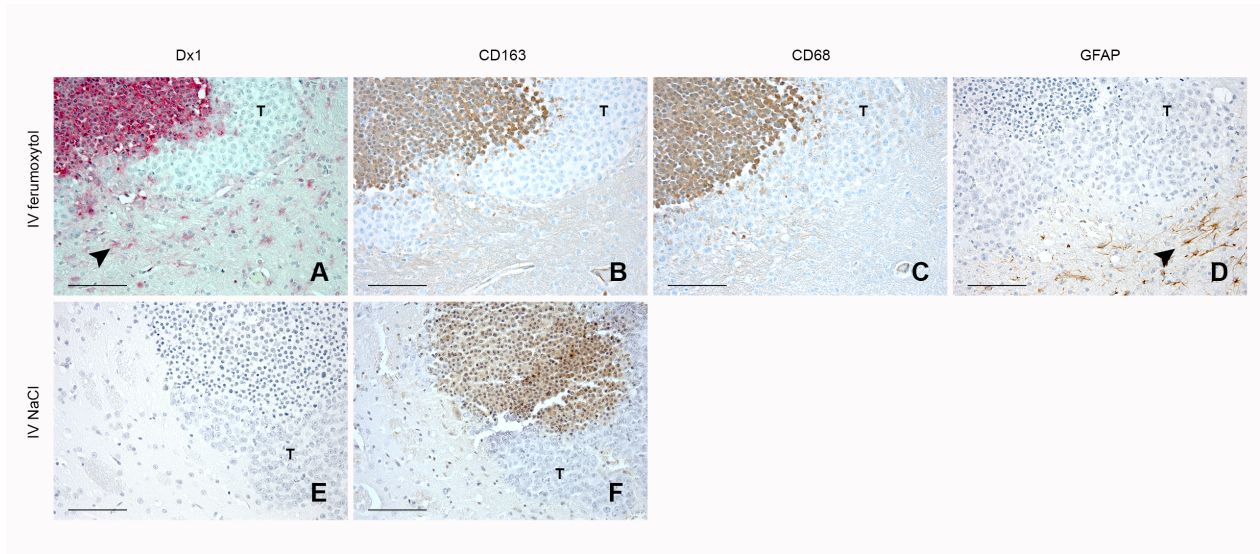


**Figure 3.3. Immunostaining demonstrates that ferumoxytol traffics from the systemic circulation to reactive CNS lesions. (A-D)** Immunostains performed 48 h after H460 cell inoculation into caudate nucleus and 24h after IV ferumoxytol administration. A representative inflammatory lesion was immunostained with **(A)** Dx1 for the ferumoxytol coating (red), **(B)** CD163 for macrophages (brown), **(C)** CD68 for macrophages (brown), and **(D)** GFAP for astrocytes (brown). **(E-F)** Immunostains performed 48h after H460 cell inoculation into caudate nucleus and 24h after IV saline administration. A representative inflammatory lesion was immunostained with **(E)** Dx1 (red), and **(F)** CD163 (brown). All cell nuclei were counterstained with hematoxylin. **T** depicts live tumor cells **(A-F)**. Arrowhead depicts reactive cells located outside of the main lesion **(A-D)**. Scale bars, 100  $\mu\text{m}$ .

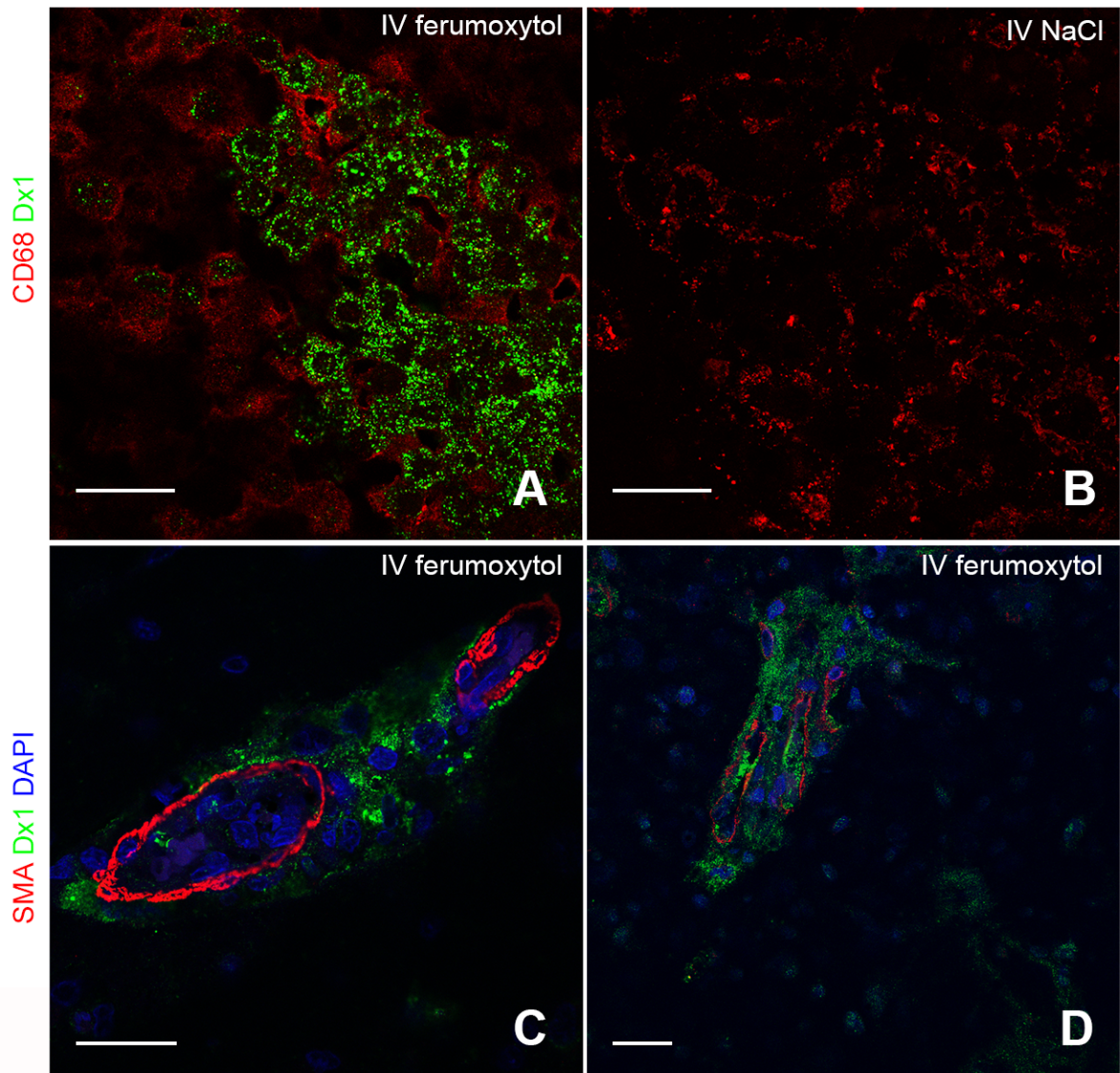


**Figure 3.4. Immunofluorescence analysis reveals ferumoxytol localization within lesional macrophages and perivascular spaces. (A)** Immunofluorescent image of CD68<sup>+</sup> (red) and Dx1<sup>+</sup> (green) macrophages in a representative inflammatory CNS lesion 48h after H460 cell inoculation into caudate nucleus and 24h after IV ferumoxytol administration. **(B)** Immunofluorescent image of CD68<sup>+</sup> and Dx1<sup>-</sup> macrophages in a representative inflammatory CNS lesion 48h after H460 cell inoculation into caudate

nucleus and 24h after IV saline administration. Scale bars, 25  $\mu\text{m}$ . **(C)** Representative immunofluorescent image demonstrating smooth muscle actin (SMA) (red) reactivity in the vascular wall and Dx1 (green) reactivity around a vessel near an inflammatory lesion. Scale bars, 25  $\mu\text{m}$ . **(D)** Representative immunofluorescent image of human glioblastoma biopsy tissue demonstrating smooth muscle actin (SMA) (red) reactivity in the vascular wall and Dx1 (green) reactivity around cerebral vessels.

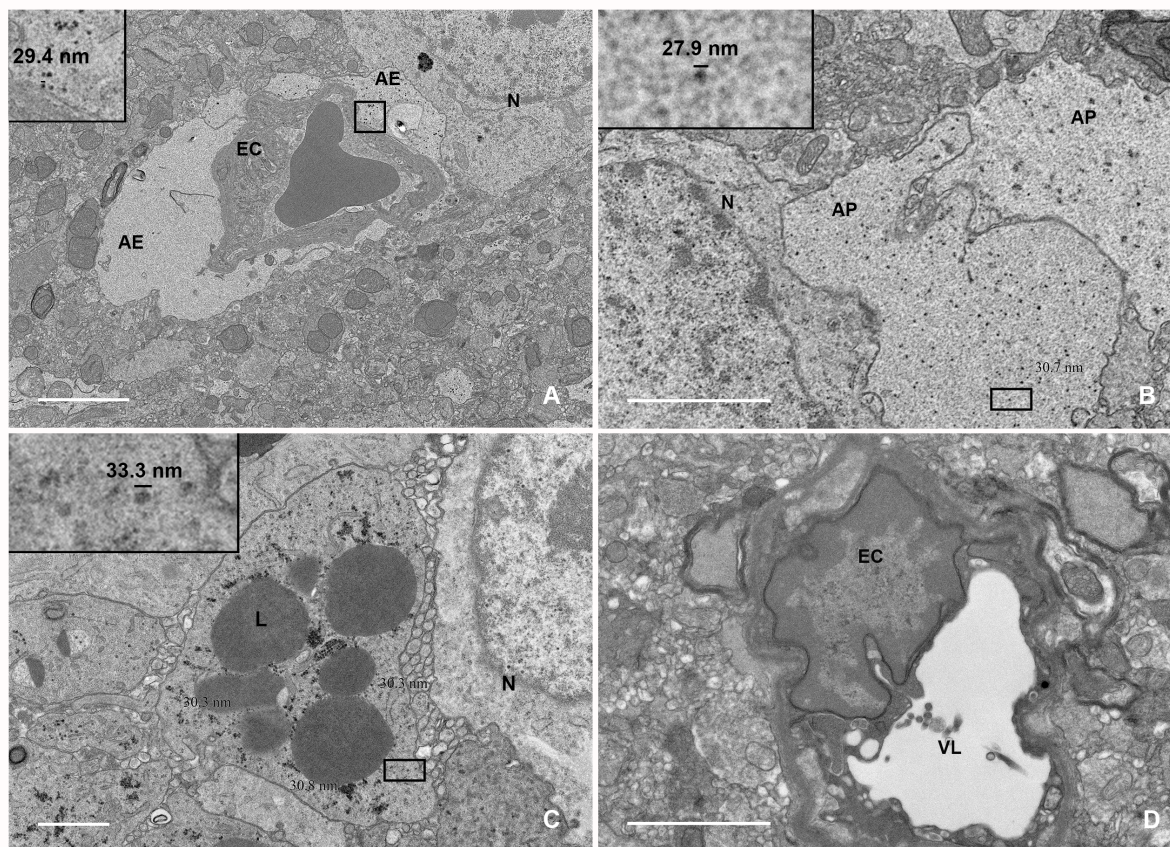


**Figure 3.5. Ultrastructural analyses of CNS tissue show ferumoxytol localization within astrocyte endfeet, astrocyte processes, and phagocytic CNS macrophages. (A-C)** Representative electron micrographs showing tissue from the caudate nucleus of neuroinflamed rats 24h after IV ferumoxytol. **(A)** Capillary cross-section showing a single luminal red blood cell and dispersed electron-dense ferumoxytol nanoparticles (inset) within the astrocyte endfoot not abutting the endothelial cell nucleus. The astrocyte endfoot abutting the vascular endothelial cell nucleus is swollen and void of ferumoxytol (magnification  $\times 2900$ ). Scale bar, 2  $\mu\text{m}$ . **(B)** Two astrocyte processes showing dispersed, electron-dense ferumoxytol nanoparticles (inset) (magnification

×6800). Scale bar, 1 μm. **(C)** Activated CNS macrophage with lysosome-rich cytoplasm and abundant intracellular ferumoxytol nanoparticle accumulation (inset) (magnification ×6800). Scale bar 1 μm. **(D)** Electron micrographs showing tissue from the contralateral (saline-inoculated) caudate nucleus of neuroinflamed rats 24h after IV ferumoxytol. Representative cerebral vessel cross-section showing no astrocyte endfoot swelling and no ferumoxytol uptake (magnification ×6800). Scale bar, 1 μm. N, neuron; EC, endothelial cell; AE, astrocyte endfoot; AP, astrocyte process; L, lysosome; VL, vessel lumen.

#### **Chapter 4. Future directions for ferumoxytol research**

The majority of the work presented in this dissertation aimed to characterize the behavior of ferumoxytol USPIO nanoparticles in the brain. To this end, I optimized a detection protocol for the nanoparticle and demonstrated that the mAb Dx1 could localize ferumoxytol in tissues unequivocally and allow it to be distinguished from endogenous iron. I also developed a novel model of neuroinflammatory lesion using immune competent rats and inflammatory human tumor cell xenografts. This model produced a localized lesion and robust inflammatory response that induced BBB dysfunction and allow contrast extravasation. Specifically, my results demonstrated that ferumoxytol was taken up differentially by particular innate immune cell subsets: avidly by CNS macrophages/microglia within the lesion, less avidly by reactive astrocytes at the lesion periphery and around cerebral vessels. My results demonstrated tumor cells did not take up ferumoxytol. Further, this work suggests that ferumoxytol exerts variable contributions to  $T_1$ -weighted MRI as a function of concentration within inflammatory cells. These distinct patterns of enhancements may be critical to resolving differences in signal within and around CNS lesions in patients receiving ferumoxytol-enhanced MRI. Broadly, my findings suggest that ferumoxytol is of great utility for non-invasive imaging of neuroinflammatory lesions that are characterized by robust macrophage/microglial infiltrate, and less useful for tumor cell imaging. This cell specific uptake may prove critical for determining whether particular inflammatory pathologies are macrophage based, which may help guide therapy at the clinical level. Ferumoxytol MRI will likely be extremely useful in pathologies where macrophages play a key role. Realistically, ferumoxytol likely holds the greatest clinical utility for imaging of pathologies in

reticuloendothelial system organs such as liver and spleen, as the nanoparticle naturally accumulates in these organs for clearance.

#### **4.1 Pseudoprogression is an immune-related response occurring after glioma therapy**

Among future directions for ferumoxytol research, the phenomenon of pseudoprogression ranks among the most clinically significant challenges to pursue. After resection and chemoradiation therapy (CRT), patients with high-grade glioma (glioblastoma; GBM) and other brain tumors are monitored over time with MRI to detect tumor response, progression, or recurrence (191). Currently, GBCA-enhanced MRI is the gold standard for assessing treatment response in these patients during follow-up imaging.

Pseudoprogression refers to MRI changes (typically, increased volume of T<sub>1</sub> enhancement) that *mimic* those that occur with recurring or progressing disease but will *resolve spontaneously* over time. Pseudoprogression occurs in 10-30% of patients, and is usually seen within 3 months of their CRT, although it has been reported up to a year after treatment (192) (Figure 4.1). Because pseudoprogression is a transient phenomenon that occurs in resolving tumors that are responding positively to treatment, it requires no intervention other than neurological symptom management). It is advantageous to continue the cancer treatment and allow the pseudoresponse to resolve naturally as 1) its occurrence is a reflection of higher treatment efficacy and 2) numerous studies have shown patients that develop pseudoprogression experience statistically significant improvements in overall survival (193-195). Premature termination of an effective therapy in these instances would therefore be prognostically disadvantageous. In contrast, true tumor progression would require a change in treatment or initiation of second-line

therapies. Thus, the inability to distinguish between pseudoprogression and true tumor growth on MRI is a clinically significant diagnostic dilemma, as each requires a treatment that is contraindicated for its counterpart (193,196,197).

The pathophysiology underlying pseudoprogression remains unknown. Multiple studies suggest that a spectrum of pathologies contribute to the imaging phenomenon, including treatment-related BBB changes and acute/subacute/late radiation effects (196,198). An immunological basis for pseudoprogression has been suggested after histopathology demonstrated CD-68<sup>+</sup> macrophage-rich inflammatory infiltrates and gliosis in patient tissues (199). This hypothesis is in line with the sequence of imaging changes that define pseudoprogression: namely, the initial increase in contrast enhancement on post-contrast T<sub>1</sub>-weighted images that mimics true progression would actually be due to an inflammatory immune response involving 1) increased BBB permeability, 2) leukocyte activation and recruitment and 3) local cytokine-mediated immune stimulation (200). The eventual loss of contrast enhancement (spontaneous resolution) would be due to the anti-tumor effects of this immune cascade that results in resolution of both the leaky vasculature and the innate immune reaction.

Both true progression and pseudoprogression result in increased BBB permeability that leads to an apparent increase in contrast enhancement. In pseudoprogression, the permeability increase is thought to be due to radiation injury to radio-sensitive cerebrovascular ECs as well as cytokine-mediated changes in NVU function (201), while in true progression it is presumed to be due to the abnormally leaky neovasculature induced by growing tumors (such vasculature lacks structural components of normal NVU; see Chapter 1, Figure 1.4B) (74). Research in the Neuwelt lab has used

DSC-MRI with ferumoxytol to exploit these mechanistic differences and shown that high rCBV correlates with active neovascularization (actively growing tumor), while low rCBV is associated with areas of necrosis and inflammation (194). More recently, the improved SS-MRI technique has shown the vascular changes that occur with pseudoprogession at high resolution (149).

*Future Directions:* In addition to its use early after administration to evaluate brain tumor vasculature and rCBV, it would be interesting to evaluate ferumoxytol as a potential biomarker of immune cell infiltration and activation at delayed (24h) timepoints. The work presented in this dissertation suggests that ferumoxytol would be an excellent candidate for this endeavor. The volume and intensity of ferumoxytol T<sub>1</sub> enhancement would theoretically be greater in pseudoprogession versus true tumor progession. Further, as the current hypothesis for the spontaneous enhancement resolution that occurs with pseudoprogession centers around immune-based resolution of tumor cells, it would be interesting to determine if the macrophages present were polarized to an anti-tumor phenotype and whether this polarization may have been directed by ferumoxytol (202). Experimentally, these tasks are not straightforward, as animal models of pseudoprogession are lacking, due in large part to the unresolved pathophysiology of the condition. In lieu of a pseudoprogession model, an alternative approach would be to use a radiation necrosis (RN) model. Clinically, RN is a manifestation of radiation-induced injury to non-neoplastic brain tissue. Like pseudoprogession, RN is difficult to distinguish from recurrent tumor on MR imaging and can occur months to years after radiotherapy. However, RN would be relatively easy to induce, as it is not defined by the spontaneous resolution that characterizes

pseudoprogression, and involves only focal delivery of high dose radiation. Insofar as pseudoprogression is characterized by a general immune response post-CRT, a RN model inducing a similar response in tumor-bearing animals may be able to recapitulate at least this aspect of the phenomenon. We are currently collaborating with the Barajas lab on an alternative model of pseudoprogression that makes use of the drug amphotericin B to stimulate macrophage infiltration into brain.

Early perfusion imaging with ferumoxytol in differentiating pseudoprogression from true progression also has potential for future research. Future studies should validate the use of rCBV as an imaging biomarker not only in GBM patients undergoing CRT, but also in those receiving immunotherapy and those with other brain tumors, particularly brain metastases. Indeed, immunotherapy may induce pseudoprogression as our lab has witnessed with the use of rituximab in CNS lymphoma. Specifically, future studies should examine the diagnostic utility of rCBV for tumor hot spot targeting prior to biopsy and stereotactic radiation surgery. rCBV may also hold potential for detecting and monitoring non-enhancing tumor. For these research endeavors, appropriate rCBV cutoff values must be defined. Currently, the ideal cutoff values for determining “high” versus “low” rCBV vary substantially in the literature (152,203-205). Though reported variation may be related to the use of different MRI sequence protocols or equipment, it is a clinically relevant problem as it may lead to patient misclassification and delivery of inappropriate treatment. A large clinical trial to validate appropriate rCBV cutoff values for differentiating pseudoprogression from true progression would be worthwhile. Ultimately, a combination of perfusion imaging MRI and delayed anatomical ferumoxytol MRI approaches will provide more accurate estimation of blood volume and

inflammation status, thereby increasing diagnostic differentiation. CNS tumor vascularity can also be assessed by the MRI-derived parameter,  $K^{trans}$ , which reflects both vascular surface area and permeability (79). Future studies should investigate whether  $K^{trans}$  can predict ferumoxytol extravasation. Studies of how rCBV,  $K^{trans}$ , and delayed ferumoxytol enhancement correlate in inflammatory versus non-inflammatory lesion and in different tumor types would significantly advance our understanding of these conditions. These studies should also stratify patients to account for the effects of individual therapies on cerebrovascular permeability, such as anti-angiogenics (206,207) and corticosteroids (208,209). With the growing clinical incidence of pseudoprogression, which is expected to increase further in the era of targeted immunotherapeutics, understanding its mechanistic underpinnings and successfully differentiating it from true progression will be clinically significant research endeavors with substantial diagnostic impact.

#### **4.2 Ferumoxytol uptake is cell-specific**

Defining cell uptake patterns of ferumoxytol is critical to understanding its behavior at inflammatory lesions and within/around the cerebrovasculature. My results indicate that ferumoxytol is taken up by reactive astrocytes and inflammatory CNS macrophages during neuroinflammation. Besides particle size, uptake is also determined by nanoparticle surface coating properties such as charge (210,211). Among iron oxide nanoparticles, ferumoxytol is not alone in its tendency to be taken up by tissue-resident macrophages; indeed, its larger SPIO predecessors [e.g. ferumoxides (Feridex®), AMI-227 (Combidex®), ferucarbotran (Resovist®)] were taken up by macrophages even more avidly (155,212,213). Ferumoxytol uptake by astrocytes had been suggested to occur in

numerous reports (158,214,215) but until the work of this dissertation was never demonstrated experimentally. This uptake is perhaps not surprising, as reactive astrocytes have been shown to demonstrate phagocytic properties (180,216) and because macrophages behave as professional phagocytes within the body (217).

*Ex vivo*, localization of ferumoxytol has only been possible using the nonspecific iron stain Perls Prussian Blue. However, Perls stain is an imperfect method to measure ferumoxytol localization because of its relatively low sensitivity, which renders it incapable of detecting low concentrations of the ferumoxytol iron oxide core. Further, Perls cannot reliably distinguish between the iron oxide nanoparticle and endogenous (e.g. hemorrhage-derived) iron deposits, a clinically relevant failing in the context of CNS lesions. My results demonstrate that an anti-dextran mAb (Dx1) reproducibly and specifically associates with the modified dextran coating of ferumoxytol, allowing the nanoparticle to be localized in tissues apart from endogenous iron (Figure 4.2). The use of the Dx1 marker is an important advancement for ferumoxytol research, as it is the first definitive means of *ex vivo* localization that does not necessitate the use of an electron microscope.

*Future Directions:* The most striking difference between astrocyte and macrophage uptake of ferumoxytol in the brain is the quantity of intracellular ferumoxytol present. As my results suggest that ferumoxytol exerts differential T<sub>1</sub> signal enhancement based on its location in macrophages versus areas of reactive gliosis, it would be interesting, scientifically, to determine whether the fate and behavior of ferumoxytol within astrocytes is similar to macrophages. Within macrophages, ferumoxytol is taken up into lysosomes, where the modified carbohydrate coating is

enzymatically cleaved and undergoes renal or fecal excretion. This degradation of the ferumoxytol coating is a potential limitation of the Dx1 marker, as the mAb will no longer show immunoreactivity with ferumoxytol once the coating is eliminated. On the other hand, the loss of reactivity over time is therefore suggestive of ferumoxytol degradation, which may facilitate study of ferumoxytol degradation kinetics. After the coating is cleaved, the iron core is taken up into cellular iron stores, similar to elemental iron (119). Experimentally, differences in astrocyte/macrophage ferumoxytol handling could be determined using the mAb Dx1 marker of ferumoxytol along with the Perls Prussian blue stain. The dual use of these agents would be informative as each localizes a separate component of ferumoxytol – the coating and the core, respectively. Therefore, the time course over which these components dissociate could be compared in macrophages and in astrocytes. Importantly, the ability of Dx1 to localize ferumoxytol in tissues will facilitate numerous future research endeavors that aim to characterize the behavior of ferumoxytol in specific peripheral and CNS pathologies.

#### **4.3. Ferumoxytol highlights cerebrospinal fluid movement through cortical glymphatic space**

Ferumoxytol may have utility in imaging and quantifying the recently described CNS fluid circulation and waste clearance pathway known as the glymphatic system. In this system, arterial pulsation (218) or dispersion (219) drives para-arterial cerebrospinal fluid (CSF) flow into the brain parenchyma. In the interstitial space of the brain parenchyma, convective bulk flow drives the exchange of solutes (e.g. proteins, metabolic waste products and excess extracellular fluids) between CSF and brain interstitial fluid (ISF).

Afterwards, there is aquaporin-4 mediated paravenous clearance of the brain metabolites into CSF or into dural sinus lymphatic vessels that connect to deep cervical lymph nodes (17,220). As impaired glymphatic clearance is implicated in numerous neurological conditions including brain trauma (221) and Alzheimer's disease (17), contrast enhanced MRI of brain extravascular space and assessment glymphatic function is clinically significant.

GBCAs have been used to assess CSF flow and glymphatic function using MRI in rodent models (218,222) and in patients (223,224) and have been administered intrathecally into subarachnoid space (218,222) and cisterna magna (224,225). Using Combidex iron oxide nanoparticles, an earlier iteration of ferumoxytol, the Neuwelt lab showed trafficking to the deep and superficial cervical lymph nodes after parenchymal or CSF infusion (226). Pilot data from our lab suggests that, following intracisternal injection, ferumoxytol provides increased susceptibility along penetrating arterioles in cortex within 10 min (See Chapter 1, Figure 1.4B). In this experiment, signal changes were detected in deep cervical lymph nodes within 20 min. Based on this trafficking pattern, ferumoxytol may also hold promise as an imaging tracer for glymphatic MRI.

*Future Directions:* Ferumoxytol has potential as a glymphatic tracer to determine the impact of CNS lesions on drainage and flow. Experimentally, this could be achieved by administering intrathecal ferumoxytol to rats with and without brain tumors, stroke, or neuroinflammatory lesions and performing MRI at various time points thereafter. Parallel experiments in immune competent rats and immunosuppressed rats could evaluate the impact of the innate and adaptive immune systems on glymphatic function. After each imaging sessions, brains and deep cervical lymph nodes could be collected and assessed

for ferumoxytol localization along glymphatic pathways, and this localization could be compared to patterns of ferumoxytol enhancement on MRI. The image resolution of the 12T magnet should be sufficient to allow detection of cerebrovessels and lymphatic vessels participating in glymphatic drainage. Studies might also make use of fluorescent FITC- (227) or rhodamine-conjugated ferumoxytol (228). The behavior of these fluorescent ferumoxytol conjugates could be compared with fluorescently conjugated dextran tracers of known molecular weights. In particular, a small molecular weight dextran (which should extravasate easily) and a large molecular weight dextran (which should not extravasate) could be used as controls. Confocal fluorescent microscopy could be used to quantify the amount of tracer(s) present in brain structures of interest and to “map” tracer movement over time. If these experiments confirm that ferumoxytol can provide useful enhancement of glymphatic drainage routes, these experiments could be translated to patients to allow assessment of glymphatic function in the setting of a brain tumor.

#### **4.4. Intracellular localization may alter the $T_1$ signal of ferumoxytol**

Delayed ferumoxytol enhancement on  $T_1$ -weighted MRI can provide hypo- or hyperintense signal enhancement at a lesion site. The biology underlying the distinct MR characteristics of ferumoxytol on  $T_1$ -weighted images has not yet been defined. Though ferumoxytol resulted in MR signal changes at all reactive inflammatory lesions in my experiments, the ferumoxytol present within macrophages appeared to differentially influence  $T_1$  signal enhancement patterns on MRI (Figure 4.3). Specifically, the ferumoxytol that was taken up by lesion-associated macrophages resulted in strong  $T_2$  contributions in these areas and these contributions were strong enough to be present on

$T_1$ -weighted MRI sequences as hypointense signal (i.e. signal drop-out). One potential hypothesis for differential ferumoxytol enhancement at macrophages is that phagocytosis alters the MRI signal and causes  $T_2$  dephasing before  $T_1$  signal can be captured (228). However, reactive astrocytes around inflammatory lesions also phagocytose ferumoxytol and uptake at these peripheral areas of reactive gliosis did not result in hypointense signal enhancement on  $T_1$ -weighted MRI sequences; indeed, these areas instead showed hyperintense signal enhancement. Thus, the ‘cellular internalization’ hypothesis is inconsistent with our findings. Another possibility is that the variability in concentration of ferumoxytol within cells causes the differential  $T_1$ -weighted contrast. This hypothesis is supported in part by my data, as my EM results indicated that the concentration of ferumoxytol within astrocytes was substantially lower than it was within lesional macrophages. Specifically, my EM data showed that the large amounts of ferumoxytol that had accumulated within lesional macrophages had effectively aggregated and had begun to form large, electron-dense entities that were easily identifiable. As the relaxation rates of MRI contrast agents are known to change as a function of concentration (as well as with temperature and field strength) (229), it is reasonable to assume that these high concentrations and presence of ferumoxytol aggregates are contributing to the increased  $T_2$  contribution in these cells. Put simply, increased  $T_2$  contributions can be explained by assuming that the protons contributing to the MR signal experience stronger dipole interactions with ferumoxytol aggregates than with individual, more disperse nanoparticles.

Ferumoxytol and other USPIO nanoparticles have been used to demonstrate numerous neuroinflammatory lesions including stroke, experimental autoimmune

encephalitis, brain tumors, and MS *in vivo* (230). However, inflammatory lesions often have characteristics and areas of variable signal enhancement that can confound clinical interpretation, including hemorrhage, edema, and cysts. Importantly, these distinct patterns of signal enhancement may aid clinical MRI interpretation and guide therapy.

*Future Directions:* Future work may investigate how ferumoxytol concentration and localization affect  $T_1$  and  $T_2$  contributions at heterogeneous CNS lesion sites, particularly before and after CRT as a means to assess local treatment response. Specifically, as CNS lesions can have areas of hemorrhage, edema, cysts and inflammatory cell infiltrate, it would be clinically and diagnostically relevant to determine how ferumoxytol affects enhancement within these different regions. This could be determined most easily with a retrospective chart review. Theoretically, how each lesion is influenced by ferumoxytol should depend on blood perfusion to the area. In other words, intravenously administered ferumoxytol should be able to reach the lesion in sufficient quantities in order to provide a discernable pattern of MRI enhancement there. Pockets of hemorrhage and cysts may not be perfused but could instead simply be their own contained volumes of blood and fluid, respectively. Ferumoxytol may still provide distinct patterns of enhancement in these regions as these areas can often appear with surrounding areas of inflammation. Edema may influence aspects of ferumoxytol behavior other than enhancement, such as the rate at which it is able to diffuse away from a lesion over time. Because there is variation in macrophagic, cystic, edematous, and hemorrhagic distributions between glial tumors, lymphomas and inflammation, ferumoxytol-enhanced MRI may improve differentiation these lesions (231).

#### **4.5 Ferumoxytol immunoconjugation may enable tumor cell labeling**

Despite the promise it holds for macrophage imaging in the CNS, the behavior of ferumoxytol at inflammatory lesions at delayed (>24h) time points was not well characterized prior to the work of Chapter 2 in this dissertation. However, as not all CNS lesions are inflammatory in nature, there are obvious limitations to its use for clinical imaging. Ferumoxytol is not taken up by tumor cells (101,232) and does not provide enhancement in solid tumors (161). To overcome this challenge, ferumoxytol nanoparticles can be physiochemically modified to target specific populations of cells via conjugation of tumor-specific antibodies to the modified carbohydrate coating of ferumoxytol. Indeed, ferumoxytol uptake into cells such as tumor cells may provide more clinically useful enhancement in non-inflammatory lesions and provide new opportunities for oncological MRI.

In collaboration with the Wilbur lab at University of Washington, we have created two novel immunoconjugations of ferumoxytol nanoparticles with tumor-specific antibodies targeting either CD20 (rituximab) or HER2 (trastuzumab). Such MRI contrast bioconjugates can be used in *in vitro* and *in vivo* models for numerous cancer molecular imaging endeavors and, as a result of their conjugate-directed specificity, may have potential uses that extend beyond that of ferumoxytol alone. Specifically, these constructs impart tumor selectivity to ferumoxytol, allowing us to direct the USPIO contrast agent to CD20 and HER2 receptor-expressing cells (B-cell lymphoma and breast cancer cells, respectively). In the context of cancer, conjugation of tumor-specific antibodies is more commonly performed on cytotoxic drugs that are then able to deliver a chemotherapeutic payload upon receptor recognition and cell uptake. Although ferumoxytol is not toxic, the principles governing delivery and internalization of these immunoconjugates are similar

and related to several factors including the density of CD20 and HER2 cell surface antigens, and the affinity of the conjugated rituximab and trastuzumab for these antigens. The magnitude of contrast enhancement provided will likely depend on the localization of the immunoconjugates after antigen recognition (i.e. cell surface-bound or internalized) and, of course, the amount of ferumoxytol successfully delivered to the cell. We have attempted to characterize the behavior of the immunoconjugates in *in vitro* models using the CD20-expressing tumor cell lines MC116 and Z138 and the HER2-expressing cell lines SKBR3 and HCC1954.

Initially I investigated the effect of each immunoconjugate on the cell viability of SKBR3 cells *in vitro* using a well-characterized WST-1 assay (233). We incubated these cell lines with their reciprocal immunoconjugate, the non-reciprocal immunoconjugate, or unconjugated ferumoxytol for 24h and compared the viability of these cells with those incubated in plain media (Figure 4.4). In the cell viability assay, 72h treatment with 30  $\mu\text{g}/\text{mL}$  trastuzumab-ferumoxytol immunoconjugate or rituximab-ferumoxytol immunoconjugate had minimal toxicity in SKBR3 and HCC1954 human breast cancer cell lines that both express HER2.

I next assessed immunoconjugate uptake *in vitro* using the same cell lines, controls, and incubation times as above. For the immunostains, I used antibodies recognizing the ferumoxytol coating (Dx1) or human IgG (to recognize the human CD20 or HER2 antibody portions of the conjugate). Co-localization of these immunostains would allow me to visualize where the ferumoxytol immunoconjugate was located, confirm cellular uptake, and perhaps visualize the time course over which the nanoparticle and the antibody conjugate dissociated. While cells robustly took up the

reciprocal immunoconjugate, the plain ferumoxytol condition and the non-reciprocal immunoconjugate condition also showed cellular uptake, contrary to expectations. This finding suggested that the nanoparticles might not be cell-specific despite conjugation to antibodies targeting cell-specific receptors. However, this result was not conclusive, particularly as several reports have shown that cancer cells do not take up ferumoxytol *in vitro* as determined by the relatively insensitive Perls stain (118,172,234,235).

To further investigate whether the cancer cells were internalizing the immunoconjugates in a target-specific manner, I performed an ultrastructural analysis using EM with the same experimental conditions described above. This analysis revealed that in cells incubated with their reciprocal immunoconjugate, nanoparticle uptake was robust and also localized to lysosomes. These cells had many more lysosomes present intracellularly, and many contained internalized immunoconjugate. Cells incubated with the non-reciprocal immunoconjugate or unconjugated ferumoxytol showed low levels of nanoparticle localization within the lysosomes of cells but drastically less so than in the positive controls. Interestingly, the cells incubated with the unconjugated ferumoxytol and the non-reciprocal immunoconjugate both displayed nanoparticle interactions at the membrane, outside of the cell, despite multiple wash steps between incubation, fixation and final processing. It is unclear whether these nanoparticles were unable to enter the cell or had recently been extruded at the time of fixation. However, their distribution and location suggest that they may be “sticky” and/or “sticking” to the plasma membrane of these cells. As this does not typically occur with unconjugated ferumoxytol *in vitro*, it may be related to our (liberal, though necessary) use of poly-L-lysine on the mounting coverslips prior to plating the cells. If ferumoxytol and the immunoconjugate were truly

sticking to the plasma membrane, they may both be taken up by non-specific pinocytosis, explaining the relatively small amounts of each we found intracellularly.

I next tested the hypothesis that conjugation of ferumoxytol to tumor-specific mAbs would allow specific visualization of brain tumors at clinically relevant doses in an *in vivo* pilot study. Delayed ferumoxytol imaging in the rat model requires high doses (25-50 mg/kg) compared to the clinical dose of 4-7 mg/kg ferumoxytol. Figure 4.6 shows our initial results testing the trastuzumab-ferumoxytol immunoconjugate in HCC1954 human breast carcinoma intracerebral xenografts. At the lower dose of ferumoxytol in this experiment, there was minimal signal change in the tumor and no enhancement in brain around tumor. In contrast, both animals receiving the trastuzumab-ferumoxytol immunoconjugate showed signal dropout in the tumor. Unfortunately, both conjugate animals had a cystic tumor, as demonstrated by bright enhancement on the T<sub>2</sub>\*-weighted pre-scans, while the animal receiving ferumoxytol alone had a smaller solid tumor, so it is not clear that the imaging changes were due to the contrast agent rather than difference in the tumor.

*Future Directions:* The next steps for these experiments should attempt to troubleshoot what appears to be non-specific uptake. For example, to investigate whether poly-lysine is causing the nanoparticles to preferentially stick at plasma membranes, different cell culture coating substrates such as collagen type IV, poly-l-ornithine, or fibronectin should be tested (236). Further, it may be that a 24h incubation period is unnecessarily long and that cells *in vitro* will non-specifically take up whatever small particulate matter is in culture with them over this a long a time period. Though the 24h timepoint has proved optimal for our *in vivo* ferumoxytol studies, it may be unnecessarily

long for *in vitro* experiments. Running the experiment again with shorter incubation times may solve this problem in both the EM experiments and the immunofluorescent histochemistry experiments. Finally, given the finding that the immunoconjugate localizes to lysosomes, it may be interesting to restrict our analysis to these subcellular structures and quantify the amount of reciprocal immunoconjugate present in cells versus non-reciprocal and unconjugated ferumoxytol to confirm that there is significantly more specific uptake than non-specific. This quantification could be performed on the EM micrographs using grid-based image quantification (237) and EM software that allows a threshold to be set for a particular level of electron density consistent with that of the nanoparticles.

Ultimately, the most exciting next step for ferumoxytol research in the Neuwelt lab will be to assess how these immunoconjugates behave *in vivo* in animal CNS tumor models. If the preliminary *in vitro* experiments confirm tumor-specific binding and uptake of the bioconjugate that is detectable using confocal and electron microscopy, the conjugates should be further tested *in vivo* to determine whether they can provide sufficiently detectable contrast enhancement at tumor sites that is independent of macrophage infiltration and cystic enhancement. The ability to provide contrast at tumor cells may have clinically and diagnostically useful implications for the identification of previously unidentifiable micrometastases in the brain (238). Further, this finding would open the door for other, novel antibody-ferumoxytol combinations that could perhaps target ferumoxytol contrast to not only cancer cells generally, but to specific subsets of cancer cells.

## Summary

Ferumoxytol is an USPIO nanoparticle that has demonstrated utility for MRI of inflammation in the CNS and in the periphery. In rat brains, ferumoxytol showed robust enhancement on T<sub>1</sub>- and T<sub>2</sub>-weighted MRI within a xenografted inflammatory lesion. The enhancement patterns at lesion sites varied and this variation appeared to correspond to the concentration of ferumoxytol; when ferumoxytol was intracellular and present in high concentration aggregates, it caused T<sub>2</sub> shortening that was present even on T<sub>1</sub>-weighted images. When ferumoxytol was present in smaller concentrations or extracellularly, it caused hyperintense signal changes on T<sub>1</sub>-weighted images. Ferumoxytol was only present within inflammatory macrophages/microglia and reactive astroglia and never within tumor cells. In light of these results, we conjugated ferumoxytol to tumor cell specific antibodies, trastuzumab and rituximab, to try and vectorize ferumoxytol to tumor cells. We hypothesized that these immunoconjugates would provide superior discrimination of tumors and small metastases on MRI relative to unconjugated ferumoxytol. Preliminary results suggest that these immunoconjugates are non-toxic and are successfully taken up by tumor cells *in vitro*. This work is a step forward in tumor diagnostic assessment and neuroinflammation assessment via MRI. Due to its extended blood pool phase and unique inflammatory cell uptake, ferumoxytol is a promising supplemental contrast agent to GBCA for imaging CNS pathologies and monitoring tissue changes related to disease or chemoradiation therapies.

## Figures

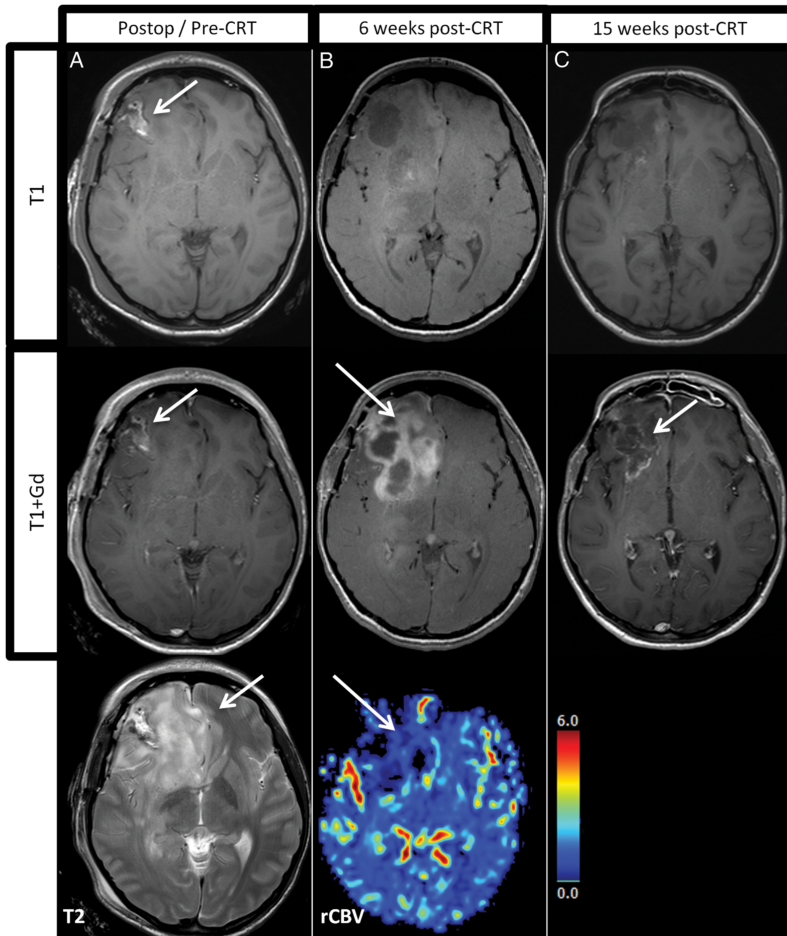


**Figure 4.1. Imaging characteristics of pseudoprogression.** Magnetic resonance images (MRI) demonstrating the phenomenon of pseudoprogression in a 23-year-old female glioblastoma patient. Column A shows scans taken prior to maximum safe resection of the right frontal lobe tumor. Column B shows scans taken 6 weeks after the patient completed her chemoradiotherapy (CRT) course. Note the large increase in gadolinium-enhanced  $T_1$  signal here, which suggests the tumor might be recurring. The relative cerebral volume (rCBV) map in the bottom row shows that blood volume at the resected tumor site is low compared to normal brain; a lack of robust blood supply suggests the

phenomenon of pseudoprogression rather than tumor recurrence. Column C shows follow-up MRI taken 15 weeks after completion of CRT and demonstrates that the previous area of enhancement was transient and resolved without any changes in treatment, consistent with pseudoprogression. Used with permission from (170).

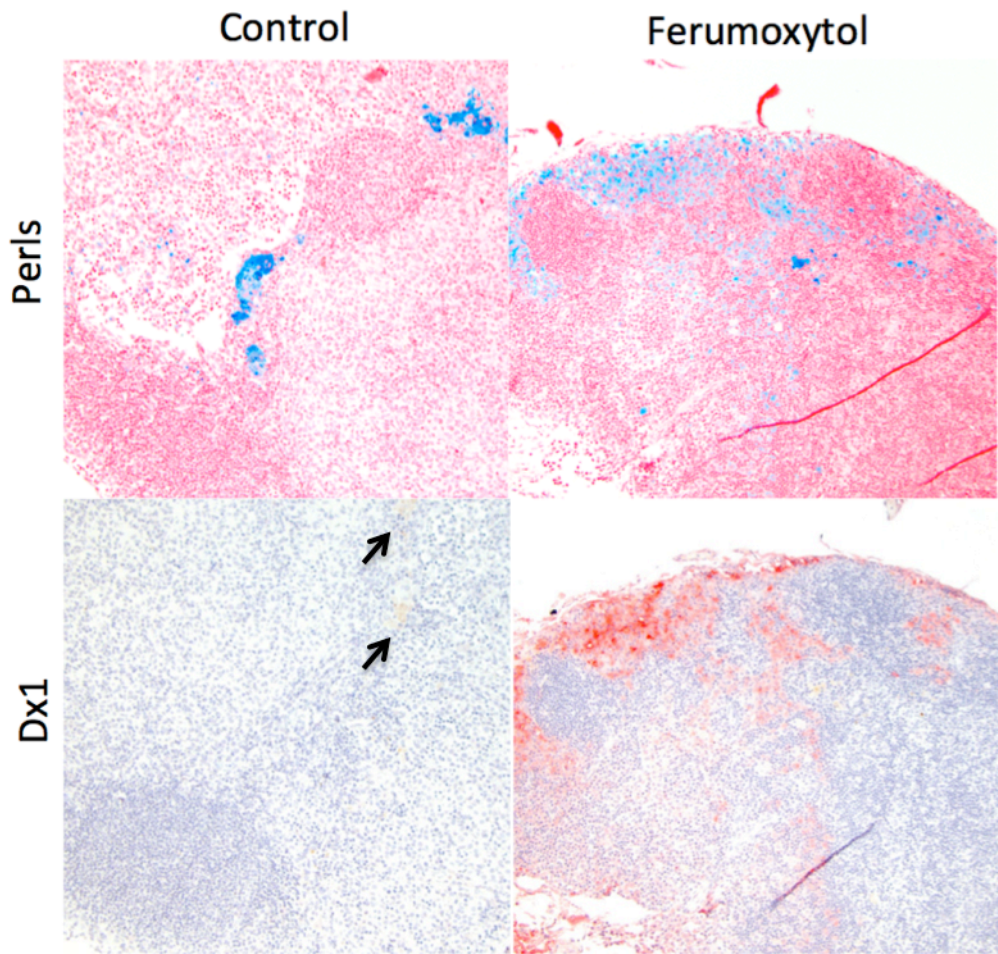


**Figure 4.2. Ferumoxytol trafficking to cervical lymph nodes.** Rat cervical lymph nodes were extracted 24h after intracerebroventricular ferumoxytol administration (right) or IV saline administration (left). Sections were stained with Perls Prussian Blue iron histochemical stain (top) or the anti-dextran monoclonal antibody Dx1 (bottom) at 1:100 with Vector Red development. Both conditions were counterstained with hematoxylin. The Dx1 reactivity demonstrated a sinusoidal distribution, suggesting macrophagic uptake. Detection sensitivity could be controlled by antibody titer with minimal background patterns. The Dx1 antibody reacted only with ferumoxytol iron nanoparticles (red), allowing us to distinguish them from endogenous iron [brown in the Dx1 panels (arrows), blue in the Perls-stained panels]. Unpublished data.

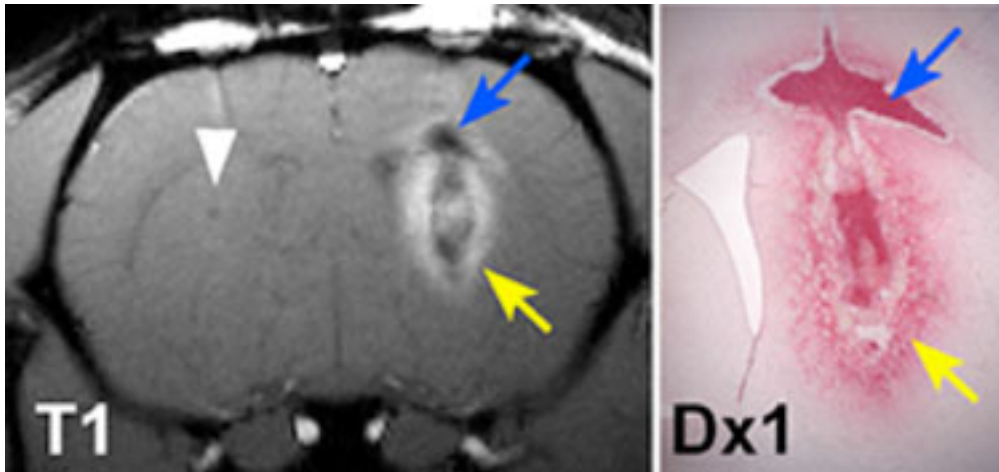


**Figure 4.3. Intracellular localization may alter the  $T_1$  signal of ferumoxytol.**

Intracerebral inoculation of human tumor cells in the right caudate nucleus of immune-competent rat brain elicits a robust inflammatory response that can be detected with  $T_1$  and  $T_2$ -weighted magnetic resonance imaging (MRI) following systemic administration of ferumoxytol. Saline injection in the contralateral hemisphere induces minimal trauma and elicits minimal signal change (arrowhead).  $T_1$ -weighted MRI (left) shows areas of hyperintensity (yellow arrow) and hypointensity (blue arrow) that correspond with areas of intracellular (blue arrow) and extracellular (yellow arrow) ferumoxytol localization, respectively, on Dx1 immunohistochemistry. Adapted from (101).

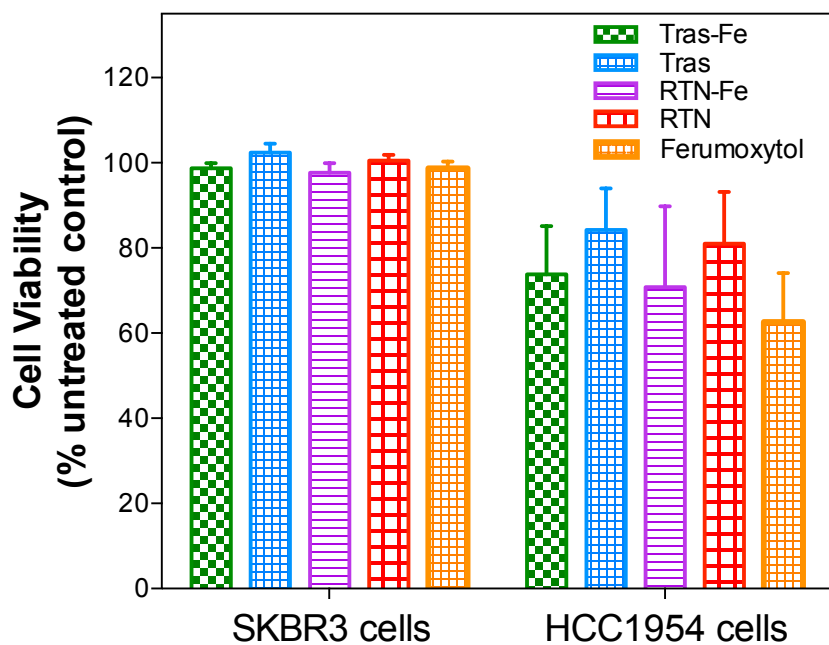


**Figure 4.4. WST-1 assay of cell survival.** Relative to media-treated controls, trastuzumab-ferumoxytol immunoconjugate (Tras-Fe), trastuzumab (Tras), rituximab-ferumoxytol immunoconjugate (RTN-Fe), rituximab (RTN), and unconjugated ferumoxytol (30  $\mu\text{g}/\text{mL}$  for all) resulted in minimal toxicity in SKBR3 and HCC1954 human breast cancer cell lines that both express HER2. Data shown are mean  $\pm$  SD values for one experiment (one culture for each cell line) performed in quadruplicate. Unpublished data.

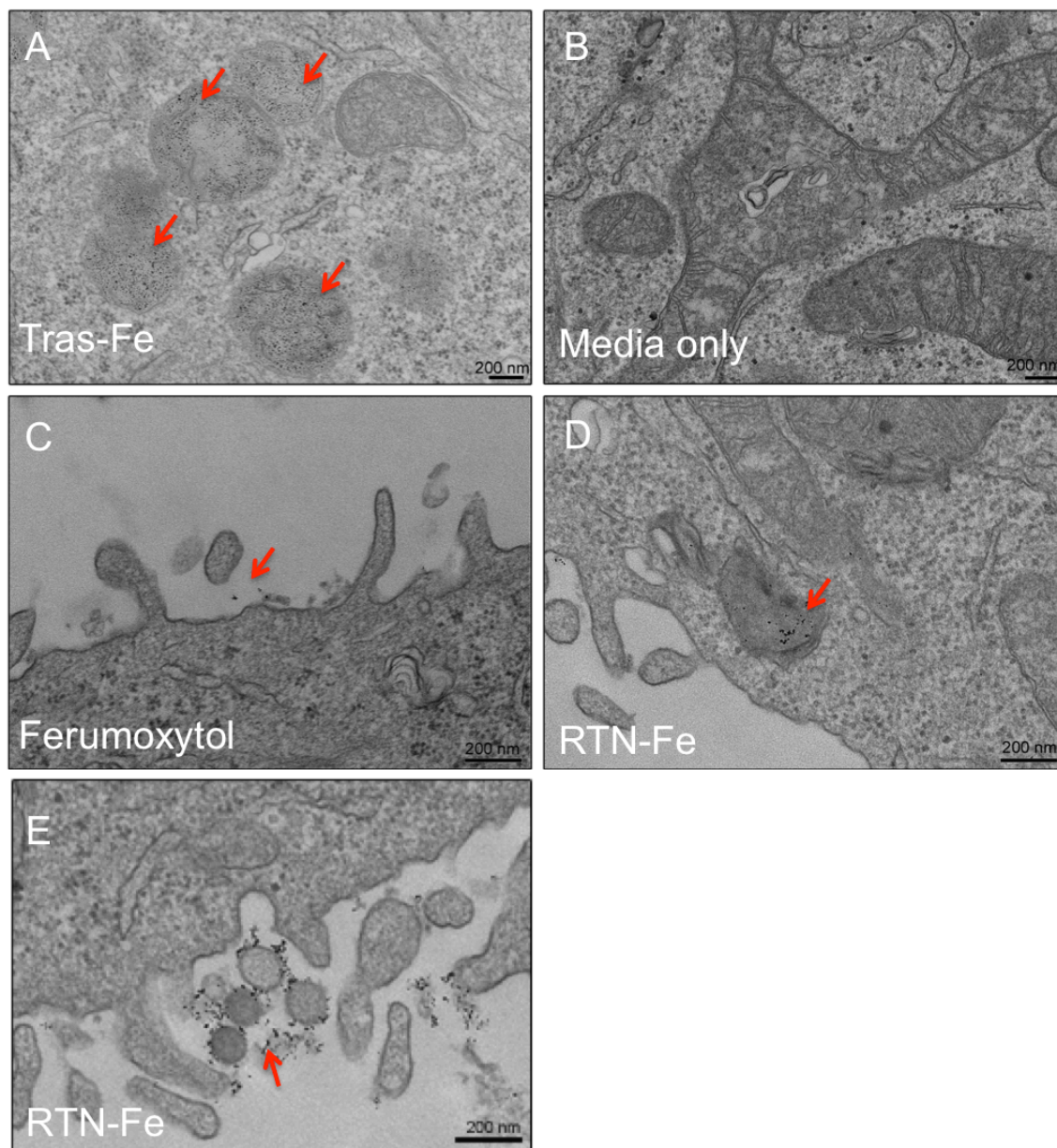


**Figure 4.5. Electron micrographs of SKBR3 human breast cancer cells treated with ferumoxytol immunoconjugate *in vitro*.** (A-E) Representative electron micrographs showing SKBR3 human breast cancer 24h after treatment with 100 µg/mL (A) trastuzumab-ferumoxytol immunoconjugate (Tras-Fe) (magnification x18500), plain media (B) (magnification x18500), unconjugated ferumoxytol (C) (magnification x30000), or (D and E) rituximab-ferumoxytol (RTN-Fe), a non-reciprocal

immunoconjugate as SKBR3 cells do not express the CD20 receptor that the rituximab monoclonal antibody targets (magnification x30000 and x13000, respectively).

Unpublished data.

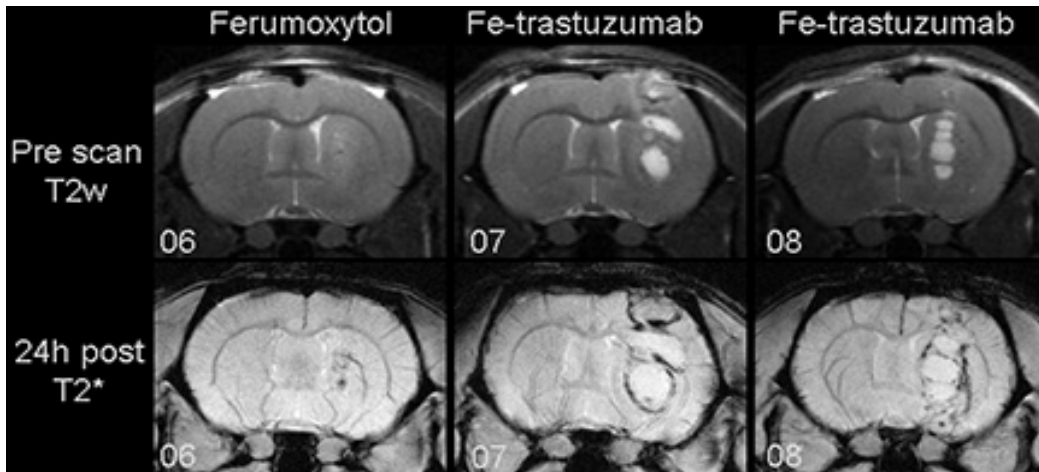


**Figure 4.6. Trastuzumab-ferumoxytol immunoconjugate *in vivo* magnetic resonance imaging pilot study.** Ten days after intracerebral implantation of HCC1954 human breast carcinoma cells, athymic rats received baseline magnetic resonance imaging (MRI) (top row) and then received either ferumoxytol alone (rat 06, 7 mg/kg ferumoxytol IV) or trastuzumab-ferumoxytol immunoconjugate (rats 07 and 08, 7mg/kg IV). Brains were imaged 24h after ferumoxytol or immunoconjugate administration, and T2\*-weighted (T2w) images are shown. Unpublished data.

## References

1. Iadecola, C. (2004) Neurovascular regulation in the normal brain and in Alzheimer's disease. *Nat Rev Neurosci* **5**, 347-360
2. Stamatovic, S. M., Keep, R. F., and Andjelkovic, A. V. (2008) Brain endothelial cell-cell junctions: how to "open" the blood brain barrier. *Curr Neuropharmacol* **6**, 179-192
3. Butt, A. M., Jones, H.C., Abbott, N.J. . (1990) Electrical resistance across the blood-brain barrier in anaesthetized rats: a developmental study.
4. Betz, A. L., Firth, J. A., and Goldstein, G. W. (1980) Polarity of the blood-brain barrier: distribution of enzymes between the luminal and antiluminal membranes of brain capillary endothelial cells. *Brain Res* **192**, 17-28
5. Sweeney, M. D., Ayyadurai, S., and Zlokovic, B. V. (2016) Pericytes of the neurovascular unit: key functions and signaling pathways. *Nat Neurosci* **19**, 771-783
6. Attwell, D., Mishra, A., Hall, C. N., O'Farrell, F. M., and Dalkara, T. (2016) What is a pericyte? *J Cereb Blood Flow Metab* **36**, 451-455
7. Hartmann, D. A., Underly, R. G., Grant, R. I., Watson, A. N., Lindner, V., and Shih, A. Y. (2015) Pericyte structure and distribution in the cerebral cortex revealed by high-resolution imaging of transgenic mice. *Neurophotonics* **2**, 041402
8. Winkler, E. A., Bell, R. D., and Zlokovic, B. V. (2011) Central nervous system pericytes in health and disease. *Nat Neurosci* **14**, 1398-1405
9. Armulik, A., Abramsson, A., and Betsholtz, C. (2005) Endothelial/pericyte interactions. *Circ Res* **97**, 512-523
10. Armulik, A., Genove, G., Mae, M., Nisancioglu, M. H., Wallgard, E., Niaudet, C., He, L., Norlin, J., Lindblom, P., Strittmatter, K., Johansson, B. R., and Betsholtz, C. (2010) Pericytes regulate the blood-brain barrier. *Nature* **468**, 557-561
11. Sakuma, R., Kawahara, M., Nakano-Doi, A., Takahashi, A., Tanaka, Y., Narita, A., Kuwahara-Otani, S., Hayakawa, T., Yagi, H., Matsuyama, T., and Nakagomi, T. (2016) Brain pericytes serve as microglia-generating multipotent vascular stem cells following ischemic stroke. *J Neuroinflammation* **13**, 57
12. Nakagomi, T., Kubo, S., Nakano-Doi, A., Sakuma, R., Lu, S., Narita, A., Kawahara, M., Taguchi, A., and Matsuyama, T. (2015) Brain vascular pericytes following ischemia have multipotential stem cell activity to differentiate into neural and vascular lineage cells. *Stem Cells* **33**, 1962-1974
13. Agulhon, C., Petravic, J., McMullen, A. B., Sweger, E. J., Minton, S. K., Taves, S. R., Casper, K. B., Fiocco, T. A., and McCarthy, K. D. (2008) What is the role of astrocyte calcium in neurophysiology? *Neuron* **59**, 932-946
14. Nagy, J. I., and Rash, J. E. (2003) Astrocyte and oligodendrocyte connexins of the glial syncytium in relation to astrocyte anatomical domains and spatial buffering. *Cell Commun Adhes* **10**, 401-406
15. Sosunov, A. A., Wu, X., Tsankova, N. M., Guilfoyle, E., McKhann, G. M., 2nd, and Goldman, J. E. (2014) Phenotypic heterogeneity and plasticity of isocortical and hippocampal astrocytes in the human brain. *J Neurosci* **34**, 2285-2298

16. Filosa, J. A., Morrison, H. W., Iddings, J. A., Du, W., and Kim, K. J. (2016) Beyond neurovascular coupling, role of astrocytes in the regulation of vascular tone. *Neuroscience* **323**, 96-109
17. Iliff, J. J., Wang, M., Liao, Y., Plogg, B. A., Peng, W., Gundersen, G. A., Benveniste, H., Vates, G. E., Deane, R., Goldman, S. A., Nagelhus, E. A., and Nedergaard, M. (2012) A paravascular pathway facilitates CSF flow through the brain parenchyma and the clearance of interstitial solutes, including amyloid beta. *Sci Transl Med* **4**, 147ra111
18. Alvarez, J. I., Katayama, T., and Prat, A. (2013) Glial influence on the blood brain barrier. *Glia* **61**, 1939-1958
19. Gordon, G. R., Howarth, C., and MacVicar, B. A. (2011) Bidirectional control of arteriole diameter by astrocytes. *Exp Physiol* **96**, 393-399
20. De Bock, M., Decrock, E., Wang, N., Bol, M., Vinken, M., Bultynck, G., and Leybaert, L. (2014) The dual face of connexin-based astroglial Ca(2+) communication: a key player in brain physiology and a prime target in pathology. *Biochim Biophys Acta* **1843**, 2211-2232
21. Tanigami, H., Okamoto, T., Yasue, Y., and Shimaoka, M. (2012) Astroglial integrins in the development and regulation of neurovascular units. *Pain Res Treat* **2012**, 964652
22. Niwa, K., Araki, E., Morham, S. G., Ross, M. E., and Iadecola, C. (2000) Cyclooxygenase-2 contributes to functional hyperemia in whisker-barrel cortex. *J Neurosci* **20**, 763-770
23. Gotoh, J., Kuang, T. Y., Nakao, Y., Cohen, D. M., Melzer, P., Itoh, Y., Pak, H., Pettigrew, K., and Sokoloff, L. (2001) Regional differences in mechanisms of cerebral circulatory response to neuronal activation. *Am J Physiol Heart Circ Physiol* **280**, H821-829
24. Yaksh, T. L., Wang, J. Y., and Go, V. L. (1987) Cortical vasodilatation produced by vasoactive intestinal polypeptide (VIP) and by physiological stimuli in the cat. *J Cereb Blood Flow Metab* **7**, 315-326
25. Scremin, O. U., Rovere, A. A., Raynald, A. C., and Giardini, A. (1973) Cholinergic control of blood flow in the cerebral cortex of the rat. *Stroke* **4**, 233-239
26. De Michele, M., Touzani, O., Foster, A. C., Fieschi, C., Sette, G., and McCulloch, J. (2005) Corticotropin-releasing factor: effect on cerebral blood flow in physiologic and ischaemic conditions. *Exp Brain Res* **165**, 375-382
27. Abounader, R., Villemure, J. G., and Hamel, E. (1995) Characterization of neuropeptide Y (NPY) receptors in human cerebral arteries with selective agonists and the new Y1 antagonist BIBP 3226. *Br J Pharmacol* **116**, 2245-2250
28. Cauli, B., Tong, X. K., Rancillac, A., Serluca, N., Lambolez, B., Rossier, J., and Hamel, E. (2004) Cortical GABA interneurons in neurovascular coupling: relays for subcortical vasoactive pathways. *J Neurosci* **24**, 8940-8949
29. Ruhrberg, C., and Bautsch, V. L. (2013) Neurovascular development and links to disease. *Cell Mol Life Sci* **70**, 1675-1684
30. Adkins, C. E., Mittapalli, R. K., Manda, V. K., Nounou, M. I., Mohammad, A. S., Terrell, T. B., Bohn, K. A., Yasemin, C., Grothe, T. R., Lockman, J. A., and Lockman, P. R. (2013) P-glycoprotein mediated efflux limits substrate and drug

- uptake in a preclinical brain metastases of breast cancer model. *Front Pharmacol* **4**, 136
31. Lacoste, B., Comin, C. H., Ben-Zvi, A., Kaeser, P. S., Xu, X., Costa Lda, F., and Gu, C. (2014) Sensory-related neural activity regulates the structure of vascular networks in the cerebral cortex. *Neuron* **83**, 1117-1130
  32. Joutel, A., Haddad, I., Ratelade, J., and Nelson, M. T. (2016) Perturbations of the cerebrovascular matrisome: A convergent mechanism in small vessel disease of the brain? *J Cereb Blood Flow Metab* **36**, 143-157
  33. da Fonseca, A. C., Matias, D., Garcia, C., Amaral, R., Geraldo, L. H., Freitas, C., and Lima, F. R. (2014) The impact of microglial activation on blood-brain barrier in brain diseases. *Front Cell Neurosci* **8**, 362
  34. Alliot, F., Godin, I., and Pessac, B. (1999) Microglia derive from progenitors, originating from the yolk sac, and which proliferate in the brain. *Brain Res Dev Brain Res* **117**, 145-152
  35. Dudvarski Stankovic, N., Teodorczyk, M., Ploen, R., Zipp, F., and Schmidt, M. H. (2016) Microglia-blood vessel interactions: a double-edged sword in brain pathologies. *Acta Neuropathol* **131**, 347-363
  36. Cherry, J. D., Olschowka, J. A., and O'Banion, M. K. (2014) Neuroinflammation and M2 microglia: the good, the bad, and the inflamed. *J Neuroinflammation* **11**, 98
  37. Goldmann, T., Wieghofer, P., Jordao, M. J., Prutek, F., Hagemeyer, N., Frenzel, K., Amann, L., Staszewski, O., Kierdorf, K., Krueger, M., Locatelli, G., Hochgerner, H., Zeiser, R., Epelman, S., Geissmann, F., Priller, J., Rossi, F. M., Bechmann, I., Kerschensteiner, M., Linnarsson, S., Jung, S., and Prinz, M. (2016) Origin, fate and dynamics of macrophages at central nervous system interfaces. *Nat Immunol* **17**, 797-805
  38. Hickey, W. F., and Kimura, H. (1988) Perivascular microglial cells of the CNS are bone marrow-derived and present antigen in vivo. *Science* **239**, 290-292
  39. Jolivel, V., Bicker, F., Biname, F., Ploen, R., Keller, S., Gollan, R., Jurek, B., Birkenstock, J., Poisa-Beiro, L., Bruttger, J., Opitz, V., Thal, S. C., Waisman, A., Bauerle, T., Schafer, M. K., Zipp, F., and Schmidt, M. H. (2015) Perivascular microglia promote blood vessel disintegration in the ischemic penumbra. *Acta Neuropathol* **129**, 279-295
  40. Davalos, D., Ryu, J. K., Merlini, M., Baeten, K. M., Le Moan, N., Petersen, M. A., Deerinck, T. J., Smirnoff, D. S., Bedard, C., Hakoziaki, H., Gonias Murray, S., Ling, J. B., Lassmann, H., Degen, J. L., Ellisman, M. H., and Akassoglou, K. (2012) Fibrinogen-induced perivascular microglial clustering is required for the development of axonal damage in neuroinflammation. *Nat Commun* **3**, 1227
  41. Bayerl, S. H., Niesner, R., Cseresnyes, Z., Radbruch, H., Pohlen, J., Brandenburg, S., Czabanka, M. A., and Vajkoczy, P. (2016) Time lapse in vivo microscopy reveals distinct dynamics of microglia-tumor environment interactions-a new role for the tumor perivascular space as highway for trafficking microglia. *Glia* **64**, 1210-1226
  42. Attwell, D., Buchan, A. M., Charpak, S., Lauritzen, M., Macvicar, B. A., and Newman, E. A. (2010) Glial and neuronal control of brain blood flow. *Nature* **468**, 232-243

43. Volterra, A., Liaudet, N., and Savtchouk, I. (2014) Astrocyte Ca(2)(+) signalling: an unexpected complexity. *Nat Rev Neurosci* **15**, 327-335
44. Gordon, G. R., Choi, H. B., Rungta, R. L., Ellis-Davies, G. C., and MacVicar, B. A. (2008) Brain metabolism dictates the polarity of astrocyte control over arterioles. *Nature* **456**, 745-749
45. Takano, T., Tian, G. F., Peng, W., Lou, N., Libionka, W., Han, X., and Nedergaard, M. (2006) Astrocyte-mediated control of cerebral blood flow. *Nat Neurosci* **9**, 260-267
46. Filosa, J. A., Bonev, A. D., Straub, S. V., Meredith, A. L., Wilkerson, M. K., Aldrich, R. W., and Nelson, M. T. (2006) Local potassium signaling couples neuronal activity to vasodilation in the brain. *Nat Neurosci* **9**, 1397-1403
47. Zonta, M., Angulo, M. C., Gobbo, S., Rosengarten, B., Hossmann, K. A., Pozzan, T., and Carmignoto, G. (2003) Neuron-to-astrocyte signaling is central to the dynamic control of brain microcirculation. *Nat Neurosci* **6**, 43-50
48. Iadecola, C., and Nedergaard, M. (2007) Glial regulation of the cerebral microvasculature. *Nat Neurosci* **10**, 1369-1376
49. Zlokovic, B. V. (2008) The blood-brain barrier in health and chronic neurodegenerative disorders. *Neuron* **57**, 178-201
50. Chasseigneaux, S., and Allinquant, B. (2012) Functions of Abeta, sAPPalpha and sAPPbeta : similarities and differences. *J Neurochem* **120 Suppl 1**, 99-108
51. Rosenberg, R. N., Lambracht-Washington, D., Yu, G., and Xia, W. (2016) Genomics of Alzheimer Disease: A Review. *JAMA Neurol* **73**, 867-874
52. Tarasoff-Conway, J. M., Carare, R. O., Osorio, R. S., Glodzik, L., Butler, T., Fieremans, E., Axel, L., Rusinek, H., Nicholson, C., Zlokovic, B. V., Frangione, B., Blennow, K., Menard, J., Zetterberg, H., Wisniewski, T., and de Leon, M. J. (2015) Clearance systems in the brain-implications for Alzheimer disease. *Nat Rev Neurol* **11**, 457-470
53. Krstic, D., Madhusudan, A., Doehner, J., Vogel, P., Notter, T., Imhof, C., Manalastas, A., Hilfiker, M., Pfister, S., Schwerdel, C., Riether, C., Meyer, U., and Knuesel, I. (2012) Systemic immune challenges trigger and drive Alzheimer-like neuropathology in mice. *J Neuroinflammation* **9**, 151
54. Kanekiyo, T., Cirrito, J. R., Liu, C. C., Shinohara, M., Li, J., Schuler, D. R., Shinohara, M., Holtzman, D. M., and Bu, G. (2013) Neuronal clearance of amyloid-beta by endocytic receptor LRP1. *J Neurosci* **33**, 19276-19283
55. Grathwohl, S. A., Kalin, R. E., Bolmont, T., Prokop, S., Winkelmann, G., Kaeser, S. A., Odenthal, J., Radde, R., Eldh, T., Gandy, S., Aguzzi, A., Staufenbiel, M., Mathews, P. M., Wolburg, H., Heppner, F. L., and Jucker, M. (2009) Formation and maintenance of Alzheimer's disease beta-amyloid plaques in the absence of microglia. *Nat Neurosci* **12**, 1361-1363
56. Yoon, S. S., and Jo, S. A. (2012) Mechanisms of Amyloid-beta Peptide Clearance: Potential Therapeutic Targets for Alzheimer's Disease. *Biomol Ther (Seoul)* **20**, 245-255
57. Chung, H., Brazil, M. I., Soe, T. T., and Maxfield, F. R. (1999) Uptake, degradation, and release of fibrillar and soluble forms of Alzheimer's amyloid beta-peptide by microglial cells. *J Biol Chem* **274**, 32301-32308

58. Wyss-Coray, T., Loike, J. D., Brionne, T. C., Lu, E., Anankov, R., Yan, F., Silverstein, S. C., and Husemann, J. (2003) Adult mouse astrocytes degrade amyloid-beta in vitro and in situ. *Nat Med* **9**, 453-457
59. Zhao, J., O'Connor, T., and Vassar, R. (2011) The contribution of activated astrocytes to Aβ production: implications for Alzheimer's disease pathogenesis. *J Neuroinflammation* **8**, 150
60. Avila-Munoz, E., and Arias, C. (2014) When astrocytes become harmful: functional and inflammatory responses that contribute to Alzheimer's disease. *Ageing Res Rev* **18**, 29-40
61. Olabarria, M., Noristani, H. N., Verkhratsky, A., and Rodriguez, J. J. (2010) Concomitant astroglial atrophy and astrogliosis in a triple transgenic animal model of Alzheimer's disease. *Glia* **58**, 831-838
62. Charles, N., and Holland, E. C. (2010) The perivascular niche microenvironment in brain tumor progression. *Cell Cycle* **9**, 3012-3021
63. Hambarzumyan, D., Becher, O. J., Rosenblum, M. K., Pandolfi, P. P., Manova-Todorova, K., and Holland, E. C. (2008) PI3K pathway regulates survival of cancer stem cells residing in the perivascular niche following radiation in medulloblastoma in vivo. *Genes Dev* **22**, 436-448
64. Shaifer, C. A., Huang, J., and Lin, P. C. (2010) Glioblastoma cells incorporate into tumor vasculature and contribute to vascular radioresistance. *Int J Cancer* **127**, 2063-2075
65. Sharma, A., and Shiras, A. (2016) Cancer stem cell-vascular endothelial cell interactions in glioblastoma. *Biochem Biophys Res Commun* **473**, 688-692
66. Pietras, A., Katz, A. M., Ekstrom, E. J., Wee, B., Halliday, J. J., Pitter, K. L., Werbeck, J. L., Amankulor, N. M., Huse, J. T., and Holland, E. C. (2014) Osteopontin-CD44 signaling in the glioma perivascular niche enhances cancer stem cell phenotypes and promotes aggressive tumor growth. *Cell Stem Cell* **14**, 357-369
67. Motegi, H., Kamoshima, Y., Terasaka, S., Kobayashi, H., and Houkin, K. (2014) Type 1 collagen as a potential niche component for CD133-positive glioblastoma cells. *Neuropathology* **34**, 378-385
68. Infanger, D. W., Cho, Y., Lopez, B. S., Mohanan, S., Liu, S. C., Gursel, D., Boockvar, J. A., and Fischbach, C. (2013) Glioblastoma stem cells are regulated by interleukin-8 signaling in a tumoral perivascular niche. *Cancer Res* **73**, 7079-7089
69. Cuddapah, V. A., Robel, S., Watkins, S., and Sontheimer, H. (2014) A neurocentric perspective on glioma invasion. *Nat Rev Neurosci* **15**, 455-465
70. Caspani, E. M., Crossley, P. H., Redondo-Garcia, C., and Martinez, S. (2014) Glioblastoma: a pathogenic crosstalk between tumor cells and pericytes. *PLoS One* **9**, e101402
71. Mignogna, C., Signorelli, F., Vismara, M. F., Zeppa, P., Camastra, C., Barni, T., Donato, G., and Di Vito, A. (2016) A reappraisal of macrophage polarization in glioblastoma: Histopathological and immunohistochemical findings and review of the literature. *Pathol Res Pract* **212**, 491-499
72. Chen, W., Wang, D., Du, X., He, Y., Chen, S., Shao, Q., Ma, C., Huang, B., Chen, A., Zhao, P., Qu, X., and Li, X. (2015) Glioma cells escaped from

- cytotoxicity of temozolomide and vincristine by communicating with human astrocytes. *Med Oncol* **32**, 43
73. Burgett, M. E., Lathia, J. D., Roth, P., Nowacki, A. S., Galileo, D. S., Pugacheva, E., Huang, P., VasANJI, A., Li, M., Byzova, T., Mikkelsen, T., Bao, S., Rich, J. N., Weller, M., and Gladson, C. L. (2016) Direct contact with perivascular tumor cells enhances integrin  $\alpha$ v $\beta$ 3 signaling and migration of endothelial cells. *Oncotarget*
  74. Farnsworth, R. H., Lackmann, M., Achen, M. G., and Stacker, S. A. (2014) Vascular remodeling in cancer. *Oncogene* **33**, 3496-3505
  75. Henshall, T. L., Keller, A., He, L., Johansson, B. R., Wallgard, E., Raschperger, E., Mae, M. A., Jin, S., Betsholtz, C., and Lendahl, U. (2015) Notch3 is necessary for blood vessel integrity in the central nervous system. *Arterioscler Thromb Vasc Biol* **35**, 409-420
  76. Mao, J. M., Liu, J., Guo, G., Mao, X. G., and Li, C. X. (2015) Glioblastoma vasculogenic mimicry: signaling pathways progression and potential anti-angiogenesis targets. *Biomark Res* **3**, 8
  77. Jain, R. K., di Tomaso, E., Duda, D. G., Loeffler, J. S., Sorensen, A. G., and Batchelor, T. T. (2007) Angiogenesis in brain tumours. *Nat Rev Neurosci* **8**, 610-622
  78. Lockman, P. R., Mittapalli, R. K., Taskar, K. S., Rudraraju, V., Gril, B., Bohn, K. A., Adkins, C. E., Roberts, A., Thorsheim, H. R., Gaasch, J. A., Huang, S., Palmieri, D., Steeg, P. S., and Smith, Q. R. (2010) Heterogeneous blood-tumor barrier permeability determines drug efficacy in experimental brain metastases of breast cancer. *Clin Cancer Res* **16**, 5664-5678
  79. Pishko, G. L., Muldoon, L. L., Pagel, M. A., Schwartz, D. L., and Neuwelt, E. A. (2015) Vascular endothelial growth factor blockade alters magnetic resonance imaging biomarkers of vascular function and decreases barrier permeability in a rat model of lung cancer brain metastasis. *Fluids Barriers CNS* **12**, 5
  80. Abbott, N. J., Ronnback, L., and Hansson, E. (2006) Astrocyte-endothelial interactions at the blood-brain barrier. *Nat Rev Neurosci* **7**, 41-53
  81. Weiss, N., Miller, F., Cazaubon, S., and Couraud, P. O. (2009) The blood-brain barrier in brain homeostasis and neurological diseases. *Biochim Biophys Acta* **1788**, 842-857
  82. Iliff, J. J., Goldman, S. A., and Nedergaard, M. (2015) Implications of the discovery of brain lymphatic pathways. *Lancet Neurol* **14**, 977-979
  83. Hamel, E. (2006) Perivascular nerves and the regulation of cerebrovascular tone. *J Appl Physiol (1985)* **100**, 1059-1064
  84. Lohrke, J., Frenzel, T., Endrikat, J., Alves, F. C., Grist, T. M., Law, M., Lee, J. M., Leiner, T., Li, K. C., Nikolaou, K., Prince, M. R., Schild, H. H., Weinreb, J. C., Yoshikawa, K., and Pietsch, H. (2016) 25 Years of Contrast-Enhanced MRI: Developments, Current Challenges and Future Perspectives. *Adv Ther* **33**, 1-28
  85. Aime, S., and Caravan, P. (2009) Biodistribution of gadolinium-based contrast agents, including gadolinium deposition. *J Magn Reson Imaging* **30**, 1259-1267
  86. Gulani, V., Calamante, F., Shellock, F. G., Kanal, E., Reeder, S. B., and International Society for Magnetic Resonance in, M. (2017) Gadolinium

- deposition in the brain: summary of evidence and recommendations. *Lancet Neurol* **16**, 564-570
87. McDonald, R. J., McDonald, J. S., Kallmes, D. F., Jentoft, M. E., Murray, D. L., Thielen, K. R., Williamson, E. E., and Eckel, L. J. (2015) Intracranial Gadolinium Deposition after Contrast-enhanced MR Imaging. *Radiology* **275**, 772-782
  88. McDonald, R. J., McDonald, J. S., Kallmes, D. F., Jentoft, M. E., Paolini, M. A., Murray, D. L., Williamson, E. E., and Eckel, L. J. (2017) Gadolinium Deposition in Human Brain Tissues after Contrast-enhanced MR Imaging in Adult Patients without Intracranial Abnormalities. *Radiology*, 161595
  89. Runge, V. M. (2017) Critical Questions Regarding Gadolinium Deposition in the Brain and Body After Injections of the Gadolinium-Based Contrast Agents, Safety, and Clinical Recommendations in Consideration of the EMA's Pharmacovigilance and Risk Assessment Committee Recommendation for Suspension of the Marketing Authorizations for 4 Linear Agents. *Invest Radiol* **52**, 317-323
  90. Cowper, S. E. (2007) Nephrogenic systemic fibrosis: a review and exploration of the role of gadolinium. *Adv Dermatol* **23**, 131-154
  91. Cowper, S. E. (2008) Gadolinium - is it to blame? *J Cutan Pathol* **35**, 520-522
  92. Cowper, S. E., Kuo, P. H., and Bucala, R. (2007) Nephrogenic systemic fibrosis and gadolinium exposure: association and lessons for idiopathic fibrosing disorders. *Arthritis Rheum* **56**, 3173-3175
  93. Finn, J. P., Nguyen, K. L., and Hu, P. (2017) Ferumoxytol vs. Gadolinium agents for contrast-enhanced MRI: Thoughts on evolving indications, risks, and benefits. *J Magn Reson Imaging* **46**, 919-923
  94. Gale, E. M., Atanasova, I. P., Blasi, F., Ay, I., and Caravan, P. (2015) A Manganese Alternative to Gadolinium for MRI Contrast. *J Am Chem Soc* **137**, 15548-15557
  95. Prince, M. R., Zhang, H. L., Chabra, S. G., Jacobs, P., and Wang, Y. (2003) A pilot investigation of new superparamagnetic iron oxide (ferumoxytol) as a contrast agent for cardiovascular MRI. *J Xray Sci Technol* **11**, 231-240
  96. Neuwelt, E. A., Varallyay, C. G., Manninger, S., Solymosi, D., Haluska, M., Hunt, M. A., Nesbit, G., Stevens, A., Jerosch-Herold, M., Jacobs, P. M., and Hoffman, J. M. (2007) The potential of ferumoxytol nanoparticle magnetic resonance imaging, perfusion, and angiography in central nervous system malignancy: a pilot study. *Neurosurgery* **60**, 601-611; discussion 611-602
  97. Neuwelt, E. A., Várallyay, C. G., Manninger, S., Solymosi, D., Haluska, M., Hunt, M. A., Nesbit, G., Stevens, A., Jerosch-Herold, M., Jacobs, P. M., and Hoffman, J. M. (2007) Potential of ferumoxytol nanoparticle MR imaging, perfusion, and angiography in CNS malignancy: A Pilot Study. *Neurosurgery* **60**, 601-611
  98. Balakrishnan, V. S., Rao, M., Kausz, A. T., Brenner, L., Pereira, B. J., Frigo, T. B., and Lewis, J. M. (2009) Physicochemical properties of ferumoxytol, a new intravenous iron preparation. *Eur J Clin Invest* **39**, 489-496
  99. Lu, M., Cohen, M. H., Rieves, D., and Pazdur, R. (2010) FDA report: Ferumoxytol for intravenous iron therapy in adult patients with chronic kidney disease. *Am J Hematol* **85**, 315-319

100. Bashir, M. R., Bhatti, L., Marin, D., and Nelson, R. C. (2015) Emerging applications for ferumoxytol as a contrast agent in MRI. *J Magn Reson Imaging* **41**, 884-898
101. McConnell, H. L., Schwartz, D. L., Richardson, B. E., Woltjer, R. L., Muldoon, L. L., and Neuwelt, E. A. (2016) Ferumoxytol nanoparticle uptake in brain during acute neuroinflammation is cell-specific. *Nanomedicine* **12**, 1535-1542
102. Hashemi, R. H., Bradley, W. G., and Lisanti, C. J. (2012) MRI : the Basics.
103. Newton, H. B. (2016) *Handbook of neuro-oncology neuroimaging*, 2nd ed., Elsevier
104. Radue, E. W., Weigel, M., Wiest, R., and Urbach, H. (2016) Introduction to Magnetic Resonance Imaging for Neurologists. *Continuum (Minneapolis)* **22**, 1379-1398
105. Burtea, C., Laurent, S., Vander Elst, L., and Muller, R. N. (2008) Contrast agents: magnetic resonance. *Handb Exp Pharmacol*, 135-165
106. Chavhan, G. B., Babyn, P. S., Thomas, B., Shroff, M. M., and Haacke, E. M. (2009) Principles, techniques, and applications of T2\*-based MR imaging and its special applications. *Radiographics* **29**, 1433-1449
107. Wood, J. C., Enriquez, C., Ghugre, N., Tyzka, J. M., Carson, S., Nelson, M. D., and Coates, T. D. (2005) MRI R2 and R2\* mapping accurately estimates hepatic iron concentration in transfusion-dependent thalassemia and sickle cell disease patients. *Blood* **106**, 1460-1465
108. Garcia, J., Liu, S. Z., and Louie, A. Y. (2017) Biological effects of MRI contrast agents: gadolinium retention, potential mechanisms and a role for phosphorus. *Philos Trans A Math Phys Eng Sci* **375**
109. Corot, C., Robert, P., Idee, J. M., and Port, M. (2006) Recent advances in iron oxide nanocrystal technology for medical imaging. *Adv Drug Deliv Rev* **58**, 1471-1504
110. Anderson, V. C., Lenar, D. P., Quinn, J. F., and Rooney, W. D. (2011) The Blood-Brain Barrier and Microvascular Water Exchange in Alzheimer's Disease. *Cardiovascular Psychiatry and Neurology* **2011**, 9
111. Runge, V. M., Schoerner, W., Niendorf, H. P., Laniado, M., Koehler, D., Claussen, C., Felix, R., and James, A. E., Jr. (1985) Initial clinical evaluation of gadolinium DTPA for contrast-enhanced magnetic resonance imaging. *Magn Reson Imaging* **3**, 27-35
112. Kanda, T., Ishii, K., Kawaguchi, H., Kitajima, K., and Takenaka, D. (2014) High signal intensity in the dentate nucleus and globus pallidus on unenhanced T1-weighted MR images: relationship with increasing cumulative dose of a gadolinium-based contrast material. *Radiology* **270**, 834-841
113. Errante, Y., Cirimele, V., Mallio, C. A., Di Lazzaro, V., Zobel, B. B., and Quattrocchi, C. C. (2014) Progressive increase of T1 signal intensity of the dentate nucleus on unenhanced magnetic resonance images is associated with cumulative doses of intravenously administered gadodiamide in patients with normal renal function, suggesting dechelation. *Invest Radiol* **49**, 685-690
114. Radbruch, A., and Quattrocchi, C. C. (2017) Interpreting signal-intensity ratios without visible T1 hyperintensities in clinical gadolinium retention studies. *Pediatr Radiol*

115. Radbruch, A., Weberling, L. D., Kieslich, P. J., Eidel, O., Burth, S., Kickingereeder, P., Heiland, S., Wick, W., Schlemmer, H. P., and Bendszus, M. (2015) Gadolinium retention in the dentate nucleus and globus pallidus is dependent on the class of contrast agent. *Radiology* **275**, 783-791
116. Ramalho, J., Castillo, M., AlObaidy, M., Nunes, R. H., Ramalho, M., Dale, B. M., and Semelka, R. C. (2015) High Signal Intensity in Globus Pallidus and Dentate Nucleus on Unenhanced T1-weighted MR Images: Evaluation of Two Linear Gadolinium-based Contrast Agents. *Radiology* **276**, 836-844
117. Bulte, J. W., and Kraitchman, D. L. (2004) Iron oxide MR contrast agents for molecular and cellular imaging. *NMR Biomed* **17**, 484-499
118. Neuwelt, E. A., Hamilton, B. E., Varallyay, C. G., Rooney, W. R., Edelman, R. D., Jacobs, P. M., and Watnick, S. G. (2009) Ultras-small superparamagnetic iron oxides (USPIOs): a future alternative magnetic resonance (MR) contrast agent for patients at risk for nephrogenic systemic fibrosis (NSF)? *Kidney Int* **75**, 465-474
119. Toth, G. B., Varallyay, C. G., Horvath, A., Bashir, M. R., Choyke, P. L., Daldrup-Link, H. E., Dosa, E., Finn, J. P., Gahramanov, S., Harisinghani, M., Macdougall, I., Neuwelt, A., Vasana-wala, S. S., Ambady, P., Barajas, R., Cetas, J. S., Ciporen, J., DeLoughery, T. J., Doolittle, N. D., Fu, R., Grinstead, J., Guimaraes, A. R., Hamilton, B. E., Li, X., McConnell, H. L., Muldoon, L. L., Nesbit, G., Netto, J. P., Petterson, D., Rooney, W. D., Schwartz, D., Szidonya, L., and Neuwelt, E. A. (2017) Current and potential imaging applications of ferumoxytol for magnetic resonance imaging. *Kidney Int* **92**, 47-66
120. Cengelli, F., Maysinger, D., Tschudi-Monnet, F., Montet, X., Corot, C., Petri-Fink, A., Hofmann, H., and Juillerat-Jeanneret, L. (2006) Interaction of functionalized superparamagnetic iron oxide nanoparticles with brain structures. *J Pharmacol Exp Ther* **318**, 108-116
121. Geisser, P., and Burckhardt, S. (2011) The pharmacokinetics and pharmacodynamics of iron preparations. *Pharmaceutics* **3**, 12-33
122. Runge, V. M., Clanton, J. A., Price, A. C., Herzer, W. A., Allen, J. H., Partain, C. L., and James, A. E., Jr. (1985) Dyke Award. Evaluation of contrast-enhanced MR imaging in a brain-abscess model. *AJNR Am J Neuroradiol* **6**, 139-147
123. Cowper, S. E., Robin, H. S., Steinberg, S. M., Su, L. D., Gupta, S., and LeBoit, P. E. (2000) Scleromyxoedema-like cutaneous diseases in renal-dialysis patients. *Lancet* **356**, 1000-1001
124. Gist, R. S., Miller, D. W., and Warren, T. (2010) A difficult airway in a patient with nephrogenic sclerosing fibrosis. *Anesth Analg* **110**, 555-557
125. Kucher, C., Steere, J., Elenitsas, R., Siegel, D. L., and Xu, X. (2006) Nephrogenic fibrosing dermatopathy/nephrogenic systemic fibrosis with diaphragmatic involvement in a patient with respiratory failure. *J Am Acad Dermatol* **54**, S31-34
126. Marckmann, P., Skov, L., Rossen, K., Dupont, A., Damholt, M. B., Heaf, J. G., and Thomsen, H. S. (2006) Nephrogenic systemic fibrosis: suspected causative role of gadodiamide used for contrast-enhanced magnetic resonance imaging. *J Am Soc Nephrol* **17**, 2359-2362
127. Grobner, T. (2006) Gadolinium--a specific trigger for the development of nephrogenic fibrosing dermatopathy and nephrogenic systemic fibrosis? *Nephrol Dial Transplant* **21**, 1104-1108

128. Todd, D. J., Kagan, A., Chibnik, L. B., and Kay, J. (2007) Cutaneous changes of nephrogenic systemic fibrosis: predictor of early mortality and association with gadolinium exposure. *Arthritis Rheum* **56**, 3433-3441
129. Gibson, S. E., Farver, C. F., and Prayson, R. A. (2006) Multiorgan involvement in nephrogenic fibrosing dermatopathy: an autopsy case and review of the literature. *Arch Pathol Lab Med* **130**, 209-212
130. Ranga, A., Agarwal, Y., and Garg, K. J. (2017) Gadolinium based contrast agents in current practice: Risks of accumulation and toxicity in patients with normal renal function. *Indian J Radiol Imaging* **27**, 141-147
131. Malayeri, A. A., Brooks, K. M., Bryant, L. H., Evers, R., Kumar, P., Reich, D. S., and Bluemke, D. A. (2016) National Institutes of Health Perspective on Reports of Gadolinium Deposition in the Brain. *J Am Coll Radiol* **13**, 237-241
132. Thomsen, H. S., Morcos, S. K., Almen, T., Bellin, M. F., Bertolotto, M., Bongartz, G., Clement, O., Leander, P., Heinz-Peer, G., Reimer, P., Stacul, F., van der Molen, A., Webb, J. A., and Committee, E. C. M. S. (2013) Nephrogenic systemic fibrosis and gadolinium-based contrast media: updated ESUR Contrast Medium Safety Committee guidelines. *Eur Radiol* **23**, 307-318
133. Kanda, T., Osawa, M., Oba, H., Toyoda, K., Kotoku, J., Haruyama, T., Takeshita, K., and Furui, S. (2015) High Signal Intensity in Dentate Nucleus on Unenhanced T1-weighted MR Images: Association with Linear versus Macrocyclic Gadolinium Chelate Administration. *Radiology* **275**, 803-809
134. Olchowoy, C., Cebulski, K., Lasecki, M., Chaber, R., Olchowoy, A., Kalwak, K., and Zaleska-Dorobisz, U. (2017) The presence of the gadolinium-based contrast agent depositions in the brain and symptoms of gadolinium neurotoxicity - A systematic review. *PLoS One* **12**, e0171704
135. McDonald, R. J., McDonald, J. S., Kallmes, D. F., Jentoft, M. E., Paolini, M. A., Murray, D. L., Williamson, E. E., and Eckel, L. J. (2017) Gadolinium Deposition in Human Brain Tissues after Contrast-enhanced MR Imaging in Adult Patients without Intracranial Abnormalities. *Radiology* **285**, 546-554
136. McDonald, R. J., McDonald, J. S., Dai, D., Schroeder, D., Jentoft, M. E., Murray, D. L., Kadirvel, R., Eckel, L. J., and Kallmes, D. F. (2017) Comparison of Gadolinium Concentrations within Multiple Rat Organs after Intravenous Administration of Linear versus Macrocyclic Gadolinium Chelates. *Radiology* **285**, 536-545
137. Muldoon, L. L., and Neuwelt, E. A. (2015) Dose-Dependent Neurotoxicity (Seizures) Due to Deposition of Gadolinium-based Contrast Agents in the Central Nervous System. *Radiology* **277**, 925-926
138. Roman-Goldstein, S. M., Barnett, P. A., McCormick, C. I., Ball, M. J., Ramsey, F., and Neuwelt, E. A. (1991) Effects of gadopentetate dimeglumine administration after osmotic blood-brain barrier disruption: toxicity and MR imaging findings. *AJNR Am J Neuroradiol* **12**, 885-890
139. Hope, M. D., Hope, T. A., Zhu, C., Faraji, F., Haraldsson, H., Ordovas, K. G., and Saloner, D. (2015) Vascular Imaging With Ferumoxytol as a Contrast Agent. *AJR Am J Roentgenol* **205**, W366-373
140. Weinstein, J. S., Varallyay, C. G., Dosa, E., Gahramanov, S., Hamilton, B., Rooney, W. D., Muldoon, L. L., and Neuwelt, E. A. (2010) Superparamagnetic

- iron oxide nanoparticles: diagnostic magnetic resonance imaging and potential therapeutic applications in neurooncology and central nervous system inflammatory pathologies, a review. *J Cereb Blood Flow Metab* **30**, 15-35
141. Brasch, R. C. (1992) New directions in the development of MR imaging contrast media. *Radiology* **183**, 1-11
  142. Varallyay, C. G., Muldoon, L. L., Gahramanov, S., Wu, Y. J., Goodman, J. A., Li, X., Pike, M. M., and Neuwelt, E. A. (2009) Dynamic MRI using iron oxide nanoparticles to assess early vascular effects of antiangiogenic versus corticosteroid treatment in a glioma model. *J Cereb Blood Flow Metab* **29**, 853-860
  143. Varallyay, C. G., Toth, G. B., Fu, R., Netto, J. P., Firkins, J., Ambady, P., and Neuwelt, E. A. (2017) What Does the Boxed Warning Tell Us? Safe Practice of Using Ferumoxytol as an MRI Contrast Agent. *AJNR Am J Neuroradiol* **38**, 1297-1302
  144. Vasanawala, S. S., Nguyen, K. L., Hope, M. D., Bridges, M. D., Hope, T. A., Reeder, S. B., and Bashir, M. R. (2016) Safety and technique of ferumoxytol administration for MRI. *Magn Reson Med* **75**, 2107-2111
  145. Law, M., Yang, S., Babb, J. S., Knopp, E. A., Golfinos, J. G., Zagzag, D., and Johnson, G. (2004) Comparison of cerebral blood volume and vascular permeability from dynamic susceptibility contrast-enhanced perfusion MR imaging with glioma grade. *AJNR Am J Neuroradiol* **25**, 746-755
  146. Muehe, A. M., Feng, D., von Eyben, R., Luna-Fineman, S., Link, M. P., Muthig, T., Huddleston, A. E., Neuwelt, E. A., and Daldrup-Link, H. E. (2016) Safety Report of Ferumoxytol for Magnetic Resonance Imaging in Children and Young Adults. *Invest Radiol* **51**, 221-227
  147. Law, M., Yang, S., Wang, H., Babb, J. S., Johnson, G., Cha, S., Knopp, E. A., and Zagzag, D. (2003) Glioma grading: sensitivity, specificity, and predictive values of perfusion MR imaging and proton MR spectroscopic imaging compared with conventional MR imaging. *AJNR Am J Neuroradiol* **24**, 1989-1998
  148. Essig, M., Shiroishi, M. S., Nguyen, T. B., Saake, M., Provenzale, J. M., Enterline, D., Anzalone, N., Dorfler, A., Rovira, A., Wintermark, M., and Law, M. (2013) Perfusion MRI: the five most frequently asked technical questions. *AJR Am J Roentgenol* **200**, 24-34
  149. Varallyay, C. G., Nesbit, E., Fu, R., Gahramanov, S., Moloney, B., Earl, E., Muldoon, L. L., Li, X., Rooney, W. D., and Neuwelt, E. A. (2013) High-resolution steady-state cerebral blood volume maps in patients with central nervous system neoplasms using ferumoxytol, a superparamagnetic iron oxide nanoparticle. *J Cereb Blood Flow Metab* **33**, 780-786
  150. Gahramanov, S., Muldoon, L. L., Li, X., and Neuwelt, E. A. (2011) Improved perfusion MR imaging assessment of intracerebral tumor blood volume and antiangiogenic therapy efficacy in a rat model with ferumoxytol. *Radiology* **261**, 796-804
  151. Essig, M., Anzalone, N., Combs, S. E., Dorfler, A., Lee, S. K., Picozzi, P., Rovira, A., Weller, M., and Law, M. (2012) MR imaging of neoplastic central nervous system lesions: review and recommendations for current practice. *AJNR Am J Neuroradiol* **33**, 803-817

152. Gahramanov, S., Raslan, A. M., Muldoon, L. L., Hamilton, B. E., Rooney, W. D., Varallyay, C. G., Njus, J. M., Haluska, M., and Neuwelt, E. A. (2011) Potential for differentiation of pseudoprogression from true tumor progression with dynamic susceptibility-weighted contrast-enhanced magnetic resonance imaging using ferumoxytol vs. gadoteridol: a pilot study. *Int J Radiat Oncol Biol Phys* **79**, 514-523
153. Boxerman, J. L., Schmainda, K. M., and Weisskoff, R. M. (2006) Relative cerebral blood volume maps corrected for contrast agent extravasation significantly correlate with glioma tumor grade, whereas uncorrected maps do not. *AJNR Am J Neuroradiol* **27**, 859-867
154. Bremer, C., Mustafa, M., Bogdanov, A., Jr., Ntziachristos, V., Petrovsky, A., and Weissleder, R. (2003) Steady-state blood volume measurements in experimental tumors with different angiogenic burdens a study in mice. *Radiology* **226**, 214-220
155. Weissleder, R., Nahrendorf, M., and Pittet, M. J. (2014) Imaging macrophages with nanoparticles. *Nat Mater* **13**, 125-138
156. de Visser, K. E., Eichten, A., and Coussens, L. M. (2006) Paradoxical roles of the immune system during cancer development. *Nat Rev Cancer* **6**, 24-37
157. Engelhardt, B. (2008) Immune cell entry into the central nervous system: involvement of adhesion molecules and chemokines. *J Neurol Sci* **274**, 23-26
158. Hamilton, B. E., Nesbit, G. M., Dosa, E., Gahramanov, S., Rooney, B., Nesbit, E. G., Raines, J., and Neuwelt, E. A. (2011) Comparative analysis of ferumoxytol and gadoteridol enhancement using T1- and T2-weighted MRI in neuroimaging. *AJR Am J Roentgenol* **197**, 981-988
159. Hamilton, B. E., Ambady, P., Nesbit, G., and Neuwelt, E. A. (2016) Ferumoxytol enhanced MRI detection of intracranial metastatic disease in *American Society of Neuroradiology 54th Annual Meeting*, Washington, D.C.
160. Stirrat, C. G., Alam, S. R., MacGillivray, T. J., Gray, C. D., Dweck, M. R., Dibb, K., Spath, N., Payne, J. R., Prasad, S. K., Gardner, R. S., Mirsadraee, S., Henriksen, P. A., Semple, S. I., and Newby, D. E. (2017) Ferumoxytol-enhanced magnetic resonance imaging in acute myocarditis. *Heart*
161. Aghighi, M., Golovko, D., Ansari, C., Marina, N. M., Pisani, L., Kurlander, L., Klenk, C., Bhaumik, S., Wendland, M., and Daldrup-Link, H. E. (2015) Imaging Tumor Necrosis with Ferumoxytol. *PLoS One* **10**, e0142665
162. DeNardo, D. G., and Coussens, L. M. (2007) Inflammation and breast cancer. Balancing immune response: crosstalk between adaptive and innate immune cells during breast cancer progression. *Breast Cancer Res* **9**, 212
163. Farrell, B. T., Hamilton, B. E., Dosa, E., Rimely, E., Nasser, M., Gahramanov, S., Lacy, C. A., Frenkel, E. P., Doolittle, N. D., Jacobs, P. M., and Neuwelt, E. A. (2013) Using iron oxide nanoparticles to diagnose CNS inflammatory diseases and PCNSL. *Neurology* **81**, 256-263
164. Hasan, D., Chalouhi, N., Jabbour, P., Dumont, A. S., Kung, D. K., Magnotta, V. A., Young, W. L., Hashimoto, T., Winn, H. R., and Heistad, D. (2012) Early change in ferumoxytol-enhanced magnetic resonance imaging signal suggests unstable human cerebral aneurysm: a pilot study. *Stroke* **43**, 3258-3265

165. Weinstein, J., Varallyay, C. G., Dosa, E., Gharmanov, S., Hamilton, B., Rooney, W. D., Muldoon, L. L., and Neuwelt, E. A. (2010) Superparamagnetic iron oxide nanoparticles: Diagnostic magnetic resonance imaging and potential therapeutic applications in neurooncology and CNS inflammatory pathologies, a review. *J Cereb Blood Flow Metab* **30**, 15-35
166. Dósa, E., Guillaume, D. J., Haluska, M., Lacy, C. A., Hamilton, B., Njus, J. M., Rooney, W. D., Kraemer, D. F., Muldoon, L. L., and Neuwelt, E. A. (2011) Magnetic resonance imaging of intracranial tumors: intra-patient comparison of gadoteridol and ferumoxytol. *Neuro Oncol* **13**, 251-260
167. Bulte, J. W., and Kraitchman, D. L. (2004) Monitoring cell therapy using iron oxide MR contrast agents. *Curr Pharm Biotechnol* **5**, 567-584
168. Enochs, W. S., Ackerman, R. H., Kaufman, J. A., and Candia, M. (1998) Gadolinium-enhanced MR angiography of the carotid arteries. *J Neuroimaging* **8**, 185-190
169. Farrell, B. T., Hamilton, B. E., Dosa, E., Rimely, E., Nasser, M., Gahramanov, S., Lacy, C. A., Frenkel, E., Doolittle, N. D., Jacobs, P. M., and Neuwelt, E. A. (2013) Using iron oxide nanoparticles to diagnose CNS inflammatory diseases and PCNSL. *Neurology* **81**, 256-263
170. Nasser, M., Gahramanov, S., Netto, J. P., Fu, R., Muldoon, L. L., Varallyay, C., Hamilton, B. E., and Neuwelt, E. A. (2014) Evaluation of pseudoprogression in patients with glioblastoma multiforme using dynamic magnetic resonance imaging with ferumoxytol calls RANO criteria into question. *Neuro Oncol* **16**, 1146-1154
171. Khurana, A., Nejadnik, H., Chapelin, F., Lenkov, O., Gawande, R., Lee, S., Gupta, S. N., Aflakian, N., Derugin, N., Messing, S., Lin, G., Lue, T. F., Pisani, L., and Daldrop-Link, H. E. (2013) Ferumoxytol: a new, clinically applicable label for stem-cell tracking in arthritic joints with MRI. *Nanomedicine (Lond)* **8**, 1969-1983
172. Thu, M. S., Bryant, L. H., Coppola, T., Jordan, E. K., Budde, M. D., Lewis, B. K., Chaudhry, A., Ren, J., Varma, N. R., Arbab, A. S., and Frank, J. A. (2012) Self-assembling nanocomplexes by combining ferumoxytol, heparin and protamine for cell tracking by magnetic resonance imaging. *Nat Med* **26**, 463-467
173. Cox, R. W. (1996) AFNI: software for analysis and visualization of functional magnetic resonance neuroimages. *Comput Biomed Res* **29**, 162-173
174. Muldoon, L. L., Pagel, M. A., Kroll, R. A., Roman-Goldstein, S., Jones, R. S., and Neuwelt, E. A. (1999) A physiological barrier distal to the anatomic blood-brain barrier in a model of transvascular delivery. *AJNR Am J Neuroradiol* **20**, 217-222
175. Lukaszevicz, A. C., Sampaio, N., Guegan, C., Benchoua, A., Couriaud, C., Chevalier, E., Sola, B., Lacombe, P., and Onteniente, B. (2002) High sensitivity of protoplasmic cortical astroglia to focal ischemia. *J Cereb Blood Flow Metab* **22**, 289-298
176. Muldoon, L. L., Manninger, S., Pinkston, K. E., and Neuwelt, E. A. (2005) Imaging, distribution, and toxicity of superparamagnetic iron oxide magnetic resonance nanoparticles in the rat brain and intracerebral tumor. *Neurosurgery* **57**, 785-796

177. Petters, C., Irrsack, E., Koch, M., and Dringen, R. (2014) Uptake and metabolism of iron oxide nanoparticles in brain cells. *Neurochem Res* **39**, 1648-1660
178. Brochet, B., Deloire, M. S., Touil, T., Anne, O., Caille, J. M., Dousset, V., and Petry, K. G. (2006) Early macrophage MRI of inflammatory lesions predicts lesion severity and disease development in relapsing EAE. *Neuroimage* **32**, 266-274
179. Virgintino, D., Monaghan, P., Robertson, D., Errede, M., Bertossi, M., Ambrosi, G., and Roncali, L. (1997) An immunohistochemical and morphometric study on astrocytes and microvasculature in the human cerebral cortex. *Histochem J* **29**, 655-660
180. Hohnholt, M. C., Geppert, M., Luther, E. M., Petters, C., Bulcke, F., and Dringen, R. (2013) Handling of iron oxide and silver nanoparticles by astrocytes. *Neurochem Res* **38**, 227-239
181. Geppert, M., Hohnholt, M. C., Thiel, K., Nurnberger, S., Grunwald, I., Rezwani, K., and Dringen, R. (2011) Uptake of dimercaptosuccinate-coated magnetic iron oxide nanoparticles by cultured brain astrocytes. *Nanotechnology* **22**, 145101
182. Jenkins, S. I., Pickard, M. R., Furness, D. N., Yiu, H. H., and Chari, D. M. (2013) Differences in magnetic particle uptake by CNS neuroglial subclasses: implications for neural tissue engineering. *Nanomedicine (Lond)* **8**, 951-968
183. Hoff, D., Sheikh, L., Bhattacharya, S., Nayar, S., and Webster, T. J. (2013) Comparison study of ferrofluid and powder iron oxide nanoparticle permeability across the blood-brain barrier. *Int J Nanomedicine* **8**, 703-710
184. Thomsen, L. B., Linemann, T., Pondman, K. M., Lichota, J., Kim, K. S., Pieters, R. J., Visser, G. M., and Moos, T. (2013) Uptake and transport of superparamagnetic iron oxide nanoparticles through human brain capillary endothelial cells. *ACS Chem Neurosci* **4**, 1352-1360
185. Wu, Y. J., Muldoon, L. L., Varallyay, C., Markwardt, S., Jones, R. E., and Neuwelt, E. A. (2007) In vivo leukocyte labeling and characterization with intravenous ferumoxides/protamine sulfate for cellular magnetic resonance imaging. *Am J Physiol – Cell Physiol* **293**, C1698-1708
186. Oude Engberink, R. D., van der Pol, S. M., Dopp, E. A., de Vries, H. E., and Blezer, E. L. (2007) Comparison of SPIO and USPIO for in vitro labeling of human monocytes: MR detection and cell function. *Radiology* **243**, 467-474
187. Wiart, M., Davoust, N., Pialat, J. B., Desestret, V., Moucharrafi, S., Cho, T. H., Mutin, M., Langlois, J. B., Beuf, O., Honnorat, J., Nighoghossian, N., and Berthezene, Y. (2007) MRI monitoring of neuroinflammation in mouse focal ischemia. *Stroke* **38**, 131-137
188. Bochner, B. S., Luscinskas, F. W., Gimbrone, M. A., Jr., Newman, W., Sterbinsky, S. A., Derse-Anthony, C. P., Klunk, D., and Schleimer, R. P. (1991) Adhesion of human basophils, eosinophils, and neutrophils to interleukin 1-activated human vascular endothelial cells: contributions of endothelial cell adhesion molecules. *J Exp Med* **173**, 1553-1557
189. del Zoppo, G. J. (2009) Inflammation and the neurovascular unit in the setting of focal cerebral ischemia. *Neuroscience* **158**, 972-982
190. Holman, D. W., Klein, R. S., and Ransohoff, R. M. (2011) The blood-brain barrier, chemokines and multiple sclerosis. *Biochim Biophys Acta* **1812**, 220-230

191. Khan, M. N., Sharma, A. M., Pitz, M., Loewen, S. K., Quon, H., Poulin, A., and Essig, M. (2016) High-grade glioma management and response assessment-recent advances and current challenges. *Curr Oncol* **23**, e383-391
192. Walker, A. J., Ruzevick, J., Malayeri, A. A., Rigamonti, D., Lim, M., Redmond, K. J., and Kleinberg, L. (2014) Postradiation imaging changes in the CNS: how can we differentiate between treatment effect and disease progression? *Future Oncol* **10**, 1277-1297
193. Brandes, A. A., Tosoni, A., Spagnolli, F., Frezza, G., Leonardi, M., Calbucci, F., and Franceschi, E. (2008) Disease progression or pseudoprogression after concomitant radiochemotherapy treatment: pitfalls in neurooncology. *Neuro Oncol* **10**, 361-367
194. Gahramanov, S., Varallyay, C., Tyson, R. M., Lacy, C., Fu, R., Netto, J. P., Nasser, M., White, T., Woltjer, R. L., Gultekin, S. H., and Neuwelt, E. A. (2014) Diagnosis of pseudoprogression using MRI perfusion in patients with glioblastoma multiforme may predict improved survival. *CNS Oncol* **3**, 389-400
195. Radbruch, A., Fladt, J., Kickingereder, P., Wiestler, B., Nowosielski, M., Baumer, P., Schlemmer, H. P., Wick, A., Heiland, S., Wick, W., and Bendszus, M. (2015) Pseudoprogression in patients with glioblastoma: clinical relevance despite low incidence. *Neuro Oncol* **17**, 151-159
196. Brandsma, D., Stalpers, L., Taal, W., Sminia, P., and van den Bent, M. J. (2008) Clinical features, mechanisms, and management of pseudoprogression in malignant gliomas. *Lancet Oncol* **9**, 453-461
197. Wen, P. Y., Macdonald, D. R., Reardon, D. A., Cloughesy, T. F., Sorensen, A. G., Galanis, E., Degroot, J., Wick, W., Gilbert, M. R., Lassman, A. B., Tsien, C., Mikkelsen, T., Wong, E. T., Chamberlain, M. C., Stupp, R., Lamborn, K. R., Vogelbaum, M. A., van den Bent, M. J., and Chang, S. M. (2010) Updated response assessment criteria for high-grade gliomas: response assessment in neuro-oncology working group. *J Clin Oncol* **28**, 1963-1972
198. Tofilon, P. J., and Fike, J. R. (2000) The radioresponse of the central nervous system: a dynamic process. *Radiat Res* **153**, 357-370
199. Stuplich, M., Hadizadeh, D. R., Kuchelmeister, K., Scorzin, J., Filss, C., Langen, K. J., Schafer, N., Mack, F., Schuller, H., Simon, M., Glas, M., Pietsch, T., Urbach, H., and Herrlinger, U. (2012) Late and prolonged pseudoprogression in glioblastoma after treatment with lomustine and temozolomide. *J Clin Oncol* **30**, e180-183
200. Ellingson, B. M., Chung, C., Pope, W. B., Boxerman, J. L., and Kaufmann, T. J. (2017) Pseudoprogression, radionecrosis, inflammation or true tumor progression? challenges associated with glioblastoma response assessment in an evolving therapeutic landscape. *J Neurooncol* **134**, 495-504
201. Kudo, S., Suzuki, Y., Noda, S. E., Mizui, T., Shirai, K., Okamoto, M., Kaminuma, T., Yoshida, Y., Shirao, T., and Nakano, T. (2014) Comparison of the radiosensitivities of neurons and glial cells derived from the same rat brain. *Exp Ther Med* **8**, 754-758
202. Zanganeh, S., Hutter, G., Spitler, R., Lenkov, O., Mahmoudi, M., Shaw, A., Pajarinen, J. S., Nejadnik, H., Goodman, S., Moseley, M., Coussens, L. M., and Daldrop-Link, H. E. (2016) Iron oxide nanoparticles inhibit tumour growth by

- inducing pro-inflammatory macrophage polarization in tumour tissues. *Nat Nanotechnol* **11**, 986-994
203. Hu, L. S., Baxter, L. C., Smith, K. A., Feuerstein, B. G., Karis, J. P., Eschbacher, J. M., Coons, S. W., Nakaji, P., Yeh, R. F., Debbins, J., and Heiserman, J. E. (2009) Relative cerebral blood volume values to differentiate high-grade glioma recurrence from posttreatment radiation effect: direct correlation between image-guided tissue histopathology and localized dynamic susceptibility-weighted contrast-enhanced perfusion MR imaging measurements. *AJNR Am J Neuroradiol* **30**, 552-558
  204. Kong, D. S., Kim, S. T., Kim, E. H., Lim, D. H., Kim, W. S., Suh, Y. L., Lee, J. I., Park, K., Kim, J. H., and Nam, D. H. (2011) Diagnostic dilemma of pseudoprogression in the treatment of newly diagnosed glioblastomas: the role of assessing relative cerebral blood flow volume and oxygen-6-methylguanine-DNA methyltransferase promoter methylation status. *AJNR Am J Neuroradiol* **32**, 382-387
  205. Verma, N., Cowperthwaite, M. C., Burnett, M. G., and Markey, M. K. (2013) Differentiating tumor recurrence from treatment necrosis: a review of neuro-oncologic imaging strategies. *Neuro Oncol* **15**, 515-534
  206. Stegmayr, C., Oliveira, D., Niemietz, N., Willuweit, A., Lohmann, P., Galdiks, N., Shah, N. J., Ermert, J., and Langen, K. J. (2017) Influence of Bevacizumab on Blood-Brain Barrier Permeability and O-(2-(18)F-Fluoroethyl)-l-Tyrosine Uptake in Rat Gliomas. *J Nucl Med* **58**, 700-705
  207. Thompson, E. M., Frenkel, E. P., and Neuwelt, E. A. (2011) The paradoxical effect of bevacizumab in the therapy of malignant gliomas. *Neurology* **76**, 87-93
  208. Stonestreet, B. S., Petersson, K. H., Sadowska, G. B., Pettigrew, K. D., and Patlak, C. S. (1999) Antenatal steroids decrease blood-brain barrier permeability in the ovine fetus. *Am J Physiol* **276**, R283-289
  209. Wolkowitz, O. M., Papadopoulos, N. M., Costello, R., Breier, A., Doran, A. R., Pickar, D., and Rubinow, D. (1990) Prednisone effects on blood-brain barrier permeability and CNS IgG synthesis in healthy humans. *Psychoneuroendocrinology* **15**, 155-158
  210. Daldrup-Link, H. E., Rudelius, M., Oostendorp, R. A., Settles, M., Piontek, G., Metz, S., Rosenbrock, H., Keller, U., Heinzmann, U., Rummeny, E. J., Schlegel, J., and Link, T. M. (2003) Targeting of hematopoietic progenitor cells with MR contrast agents. *Radiology* **228**, 760-767
  211. Matuszewski, L., Persigehl, T., Wall, A., Schwindt, W., Tombach, B., Fobker, M., Poremba, C., Ebert, W., Heindel, W., and Bremer, C. (2005) Cell tagging with clinically approved iron oxides: feasibility and effect of lipofection, particle size, and surface coating on labeling efficiency. *Radiology* **235**, 155-161
  212. Chao, Y., Makale, M., Karmali, P. P., Sharikov, Y., Tsigelny, I., Merkulov, S., Kesari, S., Wrasidlo, W., Ruoslahti, E., and Simberg, D. (2012) Recognition of dextran-superparamagnetic iron oxide nanoparticle conjugates (Feridex) via macrophage scavenger receptor charged domains. *Bioconjug Chem* **23**, 1003-1009
  213. Raynal, I., Prigent, P., Peyramaure, S., Najid, A., Rebuffi, C., and Corot, C. (2004) Macrophage endocytosis of superparamagnetic iron oxide nanoparticles:

- mechanisms and comparison of ferumoxides and ferumoxtran-10. *Invest Radiol* **39**, 56-63
214. Dósa, E., Tuladhar, S., Muldoon, L. L., Hamilton, B. E., Rooney, W. D., and Neuwelt, E. A. (2011) MRI using ferumoxytol improves the visualization of central nervous system vascular malformations. *Stroke* **42**, 1581-1588
  215. Laurent, S., Forge, D., Port, M., Roch, A., Robic, C., Vander Elst, L., and Muller, R. N. (2008) Magnetic iron oxide nanoparticles: synthesis, stabilization, vectorization, physicochemical characterizations, and biological applications. *Chem Rev* **108**, 2064-2110
  216. Nielsen, H. M., Mulder, S. D., Belien, J. A., Musters, R. J., Eikelenboom, P., and Veerhuis, R. (2010) Astrocytic A beta 1-42 uptake is determined by A beta-aggregation state and the presence of amyloid-associated proteins. *Glia* **58**, 1235-1246
  217. Rabinovitch, M. (1995) Professional and non-professional phagocytes: an introduction. *Trends Cell Biol* **5**, 85-87
  218. Iliff, J. J., Wang, M., Zeppenfeld, D. M., Venkataraman, A., Plog, B. A., Liao, Y., Deane, R., and Nedergaard, M. (2013) Cerebral arterial pulsation drives paravascular CSF-interstitial fluid exchange in the murine brain. *J Neurosci* **33**, 18190-18199
  219. Asgari, M., de Zelicourt, D., and Kurtcuoglu, V. (2016) Glymphatic solute transport does not require bulk flow. *Sci Rep* **6**, 38635
  220. Clapham, R., O'Sullivan, E., Weller, R. O., and Carare, R. O. (2010) Cervical lymph nodes are found in direct relationship with the internal carotid artery: significance for the lymphatic drainage of the brain. *Clin Anat* **23**, 43-47
  221. Plog, B. A., Dashnaw, M. L., Hitomi, E., Peng, W., Liao, Y., Lou, N., Deane, R., and Nedergaard, M. (2015) Biomarkers of traumatic injury are transported from brain to blood via the glymphatic system. *J Neurosci* **35**, 518-526
  222. Yang, L., Kress, B. T., Weber, H. J., Thiyagarajan, M., Wang, B., Deane, R., Benveniste, H., Iliff, J. J., and Nedergaard, M. (2013) Evaluating glymphatic pathway function utilizing clinically relevant intrathecal infusion of CSF tracer. *J Transl Med* **11**, 107
  223. Eide, P. K., and Ringstad, G. (2015) MRI with intrathecal MRI gadolinium contrast medium administration: a possible method to assess glymphatic function in human brain. *Acta Radiol Open* **4**, 2058460115609635
  224. Ringstad, G., Vatnehol, S. A. S., and Eide, P. K. (2017) Glymphatic MRI in idiopathic normal pressure hydrocephalus. *Brain* **140**, 2691-2705
  225. Hladky, S. B., and Barrand, M. A. (2014) Mechanisms of fluid movement into, through and out of the brain: evaluation of the evidence. *Fluids Barriers CNS* **11**, 26
  226. Muldoon, L. L., Varallyay, P., Kraemer, D. F., Kiwic, G., Pinkston, K., Walker-Rosenfeld, S. L., and Neuwelt, E. A. (2004) Trafficking of superparamagnetic iron oxide particles (Combidex) from brain to lymph nodes in the rat. *Neuropathol Appl Neurobiol* **30**, 70-79
  227. Khurana, A., Chapelin, F., Beck, G., Lenkov, O. D., Donig, J., Nejadnik, H., Messing, S., Derugin, N., Chan, R. C., Gaur, A., Sennino, B., McDonald, D. M., Kempen, P. J., Tikhomirov, G. A., Rao, J., and Daldrup-Link, H. E. (2013) Iron

- administration before stem cell harvest enables MR imaging tracking after transplantation. *Radiology* **269**, 186-197
228. Nejadnik, H., Lenkov, O., Gassert, F., Fretwell, D., Lam, I., and Daldrup-Link, H. E. (2016) Macrophage phagocytosis alters the MRI signal of ferumoxytol-labeled mesenchymal stromal cells in cartilage defects. *Sci Rep* **6**, 25897
  229. Rohrer, M., Bauer, H., Mintorovitch, J., Requardt, M., and Weinmann, H. J. (2005) Comparison of magnetic properties of MRI contrast media solutions at different magnetic field strengths. *Invest Radiol* **40**, 715-724
  230. Stoll, G., and Bendszus, M. (2009) Imaging of inflammation in the peripheral and central nervous system by magnetic resonance imaging. *Neuroscience* **158**, 1151-1160
  231. Sielska, M., Przanowski, P., Wylot, B., Gabrusiewicz, K., Maleszewska, M., Kijewska, M., Zawadzka, M., Kucharska, J., Vinnakota, K., Kettenmann, H., Kotulska, K., Grajkowska, W., and Kaminska, B. (2013) Distinct roles of CSF family cytokines in macrophage infiltration and activation in glioma progression and injury response. *J Pathol* **230**, 310-321
  232. Daldrup-Link, H. E., Golovko, D., Ruffell, B., Denardo, D. G., Castaneda, R., Ansari, C., Rao, J., Tikhomirov, G. A., Wendland, M. F., Corot, C., and Coussens, L. M. (2011) MRI of tumor-associated macrophages with clinically applicable iron oxide nanoparticles. *Clin Cancer Res* **17**, 5695-5704
  233. Ambady, P., Wu, Y. J., Walker, J. M., Kersch, C., Pagel, M. A., Woltjer, R. L., Fu, R., Muldoon, L. L., and Neuwelt, E. A. (2017) Enhancing the cytotoxicity of chemoradiation with radiation-guided delivery of anti-MGMT morpholino oligonucleotides in non-methylated solid tumors. *Cancer Gene Ther* **24**, 348-357
  234. Auerbach, M. (2008) Ferumoxytol as a new, safer, easier-to-administer intravenous iron: yes or no? *Am J Kidney Dis* **52**, 826-829
  235. Provenzano, R., Schiller, B., Rao, M., Coyne, D., Brenner, L., and Pereira, B. J. (2009) Ferumoxytol as an intravenous iron replacement therapy in hemodialysis patients. *Clin J Am Soc Nephrol* **4**, 386-393
  236. Liberio, M. S., Sadowski, M. C., Soekmadji, C., Davis, R. A., and Nelson, C. C. (2014) Differential effects of tissue culture coating substrates on prostate cancer cell adherence, morphology and behavior. *PLoS One* **9**, e112122
  237. Ninomiya, Y., Zhao, W., and Saga, Y. (2016) GBIQ: a non-arbitrary, non-biased method for quantification of fluorescent images. *Sci Rep* **6**, 26454
  238. Nayak, L., Lee, E. Q., and Wen, P. Y. (2012) Epidemiology of brain metastases. *Curr Oncol Rep* **14**, 48-54